Prostate Segmentation for Medical Interventions

by

Seyedeh Sara Mahdavi

B.A.Sc., Sharif University of Technology, 2004
M.A.Sc., University of Tehran, 2007

A THESIS SUBMITTED IN PARTIAL FULFILLMENT OF
THE REQUIREMENTS FOR THE DEGREE OF

DOCTOR OF PHILOSOPHY

in

The Faculty of Graduate Studies

(Electrical and Computer Engineering)

THE UNIVERSITY OF BRITISH COLUMBIA

(Vancouver)

November 2012

Abstract

Prostate cancer is the most prevalent type of cancer among men. Accurate delineation and appropriate visualization of the prostatic region can greatly affect treatment of prostate cancer and has the potential to reduce some of the treatment side-effects. The main goal of this research is to develop a prostate segmentation tool which is suitable to replace manual delineation. Manual segmentation, the current standard in procedures such as low dose rate prostate brachytherapy, is tedious, time consuming and observer dependent. We propose a 3D semi-automatic segmentation tool to overcome these limitations. To show the clinical value of this method we perform extensive dosimetric evaluation on in-vivo ultrasound images. This tool is currently being clinically used as part of the prostate brachytherapy treatment procedure at the BC Cancer Agency.

Ultrasound is the common modality for imaging the prostate. Although safe and simple to use, it can not always allow the prostate to be reliably delineated. Vibro-elastography is a relatively new imaging method which is used to characterize mechanical properties of tissue. We investigate the suitability of vibro-elastography for visualizing the prostate. We compare in-vivo B-mode ultrasound and vibro-elastograpy images with the gold standard MRI in terms of contrast, edge visibility and the shape and size of the gland as seen in these images. Based on our results we develop a 3D automatic prostate segmentation tool in which, in addition to B-mode, information from vibro-elastography images is used in an iterative model-based segmentation approach.

We conclude this work by studying the visibility of cancer itself in vibro-elastography images. Areas suspected for cancer are manually marked on the images and the results are compared to the marked cancer in registered pathology slices. Our preliminary results show that vibro-elastography has the potential to be used for detecting prostate cancer; however, we suggest a combined use of various modalities or image types to improve cancer detection.

Preface

This thesis is primarily based on four manuscripts, resulting from the collaboration between multiple researchers. All publications have been modified to make the thesis coherent. Ethical approval for conducting this research has been provided by the Clinical Research Ethics Board, certificate numbers: H08-02696, H06-70146.

A version of Chapter 2 has been published in:

- S. Sara Mahdavi, Nick Chng, Ingrid Spadinger, William J. Morris, and Septimiu E. Salcudean. Semi-automatic segmentation for prostate interventions, *Medical Image Analysis*, 15(2011)226-237

The contribution of the author was developing, implementing, and evaluating the method. Dr. Chng developed a user interface in order to simplify the use of the original algorithm for evaluation and to prepare the method as a tool to be used at the Vancouver Cancer Center. Dr. Spadinger helped develop the idea of using nine sectors in evaluation. Dr. Morris and Prof. Salcudean helped with their valuable suggestions in improving the methodology. All co-authors contributed to the editing of the manuscript.

A version of Chapter 3 is in press for publication in:

- S.S. Mahdavi, I. Spadinger, N. Chng, S.E. Salcudean, W.J. Morris. Semiautomatic segmentation for prostate brachytherapy: Dosimetric Evaluation, *Brachytherapy*, 2011

The contribution of the author was developing and implementing the dosimetric evaluation methods. The co-authors helped with their suggestions in the evaluation and Dr. Spadinger created the treatment plans used in the evaluation process. All co-authors contributed to the editing of the manuscript.

A version of Chapter 4 has been published in:

Table of Contents

List of Tables

List of Figures

List of Abbreviations

2D/3D	2-/3-Dimensional
ASM	Active Shape Model
BCCA	British Columbia Cancer Agency
B-mode	Brightness Mode
CC	Cross Correlation
CF	Coherence Function
CNR	Contast to Noise Ratio
CT	Computed Tomography
CTV	Clinical Target Volume
DRE	Digital Rectal Examination
DSC	Dice Similarity Coefficient
ICP	Iterative Closest Point
IMMPDA	Interacting Multiple Model Probabilistic Data Association
LDR	Low Dose Rate
MRI	Magnetic Resonance Imaging
OR	Operating Room
PSA	Prostate Specific Antigen
PTV	Planning Target Volume
RF	Radio Frequency
RO	Radiation Oncologist
ROI	Region Of Interest
TDPE	Time Domain cross-correlation with Prior Estimates
TES	Tapered Ellipsoid Segmentation
TF	Transfer Function
TRUS	Trans-Rectal Ultrasound
US	Ultrasound
VCC	Vancouver Cancer Center
VE	Vibro-elastography

Acknowledgements

Chapter 1

Introduction

The prostate is an exocrine gland of the male reproductive system. It weighs approximately 20gr in young adults and has the approximate shape and size of a walnut [38]. The normal prostate of an adult has average dimensions of 33mm in length (superior-inferior), 24mm in thickness (anterior-posterior) and 41mm in width (left-right). This may vary in different geographical locations or due to malignancies such as tumors or benign prostatic hyperplasia. The prostate is enveloped by a thin but firm fibrous capsule. Two neurovascular bundles lie posterolateral to the gland which are collections of vessels and neural structures and are responsible for proper erectile function. Hence, it is desirable to preserve them during surgery. The superior region of the prostate, or the base, encircles the bladder neck, while the inferior region of the gland, or the apex, is bounded by the muscles of the pelvic floor. Posterior to the prostate lies the rectum. The prostate is transversally at its largest in the superior mid-gland region and tapers down toward the apex. Originating from the bladder and passing through the gland lies the urethra. At the midportion of the urethra a raised ridge called the verumontanum exists and at this location the two ejaculatory ducts join the urethra. At the distal end of the ejaculatory ducts, at the posterior base of the prostate, lie the seminal vesicles and vas deferens which provide a majority of the ejaculate volume.

Based on McNeal's definition [68] the prostate is divided into three zones: the central zone, the peripheral zone and the transitional zone. The central zone, which composes 25% of the gland, is a cone shaped region that surrounds the ejaculatory ducts. The peripheral zone forms a majority of the gland and lies in the posteriolateral region. The transitional zone surrounds the prostatic urethra proximal to the verumontanum and forms only 5-10% of the gland in healthy tissue. This region grows with age and is responsible for benign prostatic hyperplasia (BPH). Finally, the fibromuscular stroma, which is composed of only fibrous and muscle tissue and lacks glandular components, lies in the mid-anterior region of the gland and accounts for approximately 5% of the gland volume. Figure 1.1 illustrates the prostate, its periphery and the zones.
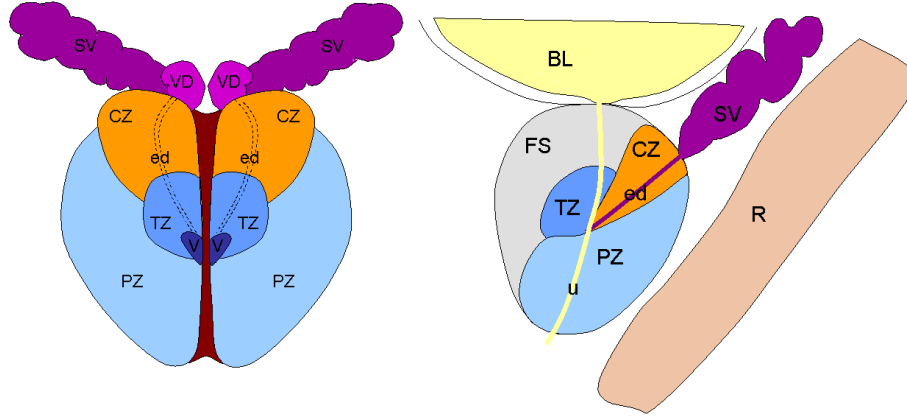
Figure 1.1: An illustration of the prostate and its periphery, in the coronal (left) and sagittal (right) views, displaying the bladder (BL), rectum (R), seminal vesicles (SV) and vas deferens (VD). The three zones are also shown. The central zone (CZ) surrounds the ejaculatory ducts (ed), the transitional zone (TZ) surrounds the prostatic urethra (u) proximal to the verumontanum (V) and the peripheral zone (PZ) forms a majority of the gland. The fibromascular stroma (FS) lies in the mid-anterior part of the prostate and lacks glandular components.

Out of various prostate disorders, prostatitis (inflammation of the gland), benign prostatic hyperplasia (or BPH - enlargement of the transitional zone leading to difficulty in urination) and prostate cancer can be named. Prostate cancer is the most prevalent type of cancer among men and is projected to affect 26,500 men in Canada [12] and 241,740 in the U.S. [74] in 2012. It is the most numerous cancer diagnosed in European men (382,000 cases in 2008, as reported by Ferlay et al.) [28]. Prostate cancer is multifocal in nature. According to McNeal et al. [64] 68% of prostate cancer cases occur in the peripheral zone, 8% in the central zone and 24% in the transitional zone. The small vessels and nerves which enter the prostate from the neurovascular bundles also create a potential pathway for the spread of prostate cancer to outside the prosatatic capsule.

Based on the malignancy of the cancer, the patient's condition (e.g. age, other diseases, etc), and patient preference, various cancer treatment methods exists which may be performed alone, or in combination. Some of these methods include:

- Watchful waiting: Closely monitoring the patient's condition without

giving treatment until symptoms change. It is used in cases where prostate cancer has a slow growth.

- Prostatectomy: Removal of the prostate, either by laparoscopic or open surgery. The surgical margin within which the prostate is removed depends on the stage of the disease.

- External beam radiation therapy (EBRT): Utilizing external radiation focused on the prostate to kill cancer cells. It is recommended for patients with a significant risk of extraprostatic cancer [69].

- Low dose rate brachytherapy: Generally used for early stage, intra-capsular prostate cancer and has rapidly gained acceptance due to its highly successful clinical results [10, 36, 66, 71, 124]. In this treatment, small radioactive seeds (Iodine-125 or Palladium-103) are inserted through the perineum and permanently implanted into the prostate and periprostatic tissue.

- High dose rate (HDR) brachytherapy: Temporary catheters are placed inside the prostate which allow treatment with a high dose rate radioactive source, usually iridium-192, for 5-15 minutes, delivering the radiation treatment over a number of fractions, typically over a few days.

- Hormone therapy: Lowering testosterone levels to stop the growth of cancer cells.

- Chemotherapy: Given as pills or by injection, it is usually used when cancer is in its advanced stage.

- High-intensity focused ultrasound (HIFU): The use of ultrasound to destroy cancer cells.

Currently, common early detection methods are screening the prostate specific antigen (PSA) levels and digital rectal examination (DRE). PSA is a protein produced by normal prostate cells. A rise in levels of PSA (measured in ng/mL) is associated with prostate cancer, benign prostatic hyperplasia or acute bacterial prostatitis. DRE is a physical examination in which the prostate is palpated through the rectum for bumps or abnormalities. Both methods are not accurate and further tests are required. Further confirmation of cancer can be obtained by biopsy (performed either transrectal, transurethral or transperineal). However, false negative rates are relatively high in prostate biopsy.
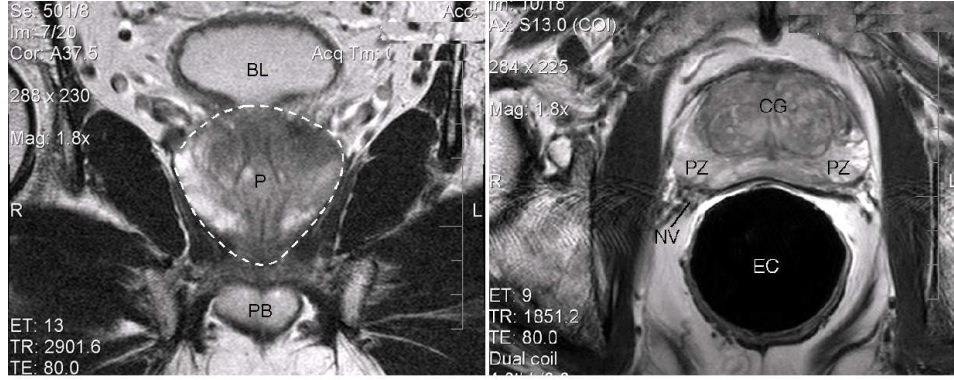
Figure 1.2: MRI images of the prostate in the coronal (left) and transverse (right) views displaying the outline of the prostate (P- dashed line), the bladder (BL) and the penile bulb (PB). In the transverse image an endorectal coil (EC) is placed inside the rectum for higher image quality, better showing the central zone (CZ), peripheral zone (PZ) and neurovascular bundles (NV).

Commonly used modalities for imaging the prostate include transrectal ultrasound (TRUS), computed tomography (CT), and magnetic resonance imaging (MRI). Figure 1.2 shows the coronal and transverse view of the prostate in MRI and Fig. 1.3 displays transverse ultrasound B-mode images of the prostate at two levels: the base and the mid-gland.

1.1 Motivation

Effective localized treatment of prostate cancer, regardless of the treatment method used, requires accurate visualization of the gland and its surrounding region.

Reliably detecting the prostate boundary can aid proper removal of the prostate in prostatectomy. In prostate radiation therapy the prostate boundary is required both prior to treatment, during planning and delivery and, in the case of low dose rate brachytherapy, after treatment for dosimetric assessment. Accurate delineation of the prostate during treatment planning and delivery has the potential to reduce some of the possible side-effects of the current treatment methods. These complications include urinary incontinence, impotence, and damage to the rectum and urethra [107].

Ultrasound is the most commonly used modality for imaging the prostate. This is due to its availability, safety and ease of use. However, ultrasound

4
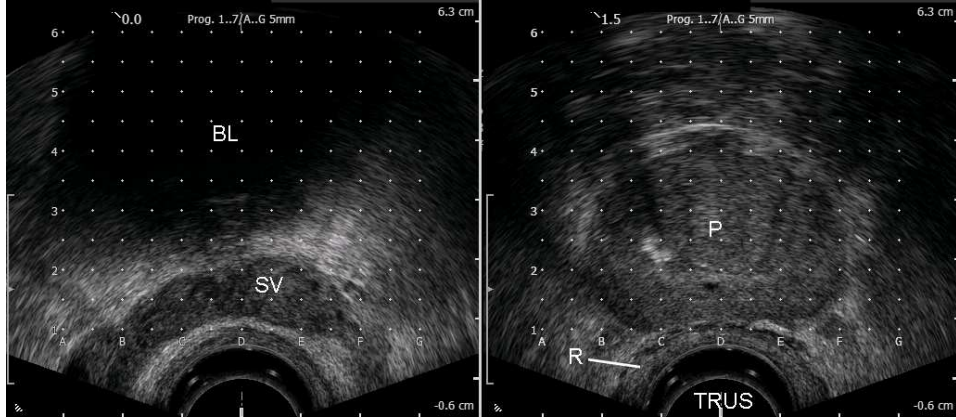
Figure 1.3: Transverse ultrasound B-mode images of the prostate at the base (left) and mid-gland (right). The seminal vesicles (SV) and the shadow of the bladder (BL) are visible at the base. At the mid-gland, the location of the transrectal ultrasound (TRUS) probe inside the rectum (R) is labeled. The various zones of the prostate (P) are not always distinguishable in TRUS images. However, in this case the neurovascular bundles can be faintly seen at locations 1-B and 1-F of the grid.

B-mode images do not always delineate the prostate reliably. As a result, manual extraction of the prostate boundary becomes a highly subjective process, depending on the experience, skill, and technique of the contourer. This is particularly evident in the base and apical regions of the gland, where the prostate boundary blends into the surrounding anatomy in TRUS images, becoming more ambiguous and difficult to delineate. Consequently, there is substantial inter-observer variation in the contours for a given patient in these regions. Smith et al. [98] have evaluated the reproducibility of prostate contouring, after brachytherapy implants, using 3DTRUS, T2-weighted MR and CT imaging. Prostates from 10 patients with early-stage prostate cancer (T2b or less) were segmented twice by seven observers. Their results showed high contouring variability of the anterior base and apex in 3DTRUS, whereas the prostate-rectum interface had the smallest variability. A study by [15, 108] showed that prostate volume measurement by transrectal ultrasound may vary among observers when patients have large prostates ($\geq$30 cm^3). The average volume difference between 101 prostates measured by two experienced observers was reported as 6.00 cm^3 for prostates with a mean measured volume $\geq$30 cm^3 and 1.51 cm^3 for prostates with a mean measured volume $\leq$30 cm^3. These numbers increased to 6.84 cm^3 and

3.99 cm^3, respectively, when measurements were performed by one experienced and one less experienced observer (110 prostate volumes measured in this case). Manual contouring is also time consuming. This is a major drawback if an intraoperative treatment procedure is to be performed.

The motivation for an automatic segmentation method is to reduce user dependence of contouring, replace a repetitive and time-consuming task, and develop a technique which is fast enough to be used intraoperatively. Automated contouring can also be integrated into other intraoperative treatment methods such as for LDR brachytherapy where imaging the prostate, segmenting the boundary and creating the treatment plan can all be carried out inside the operating room.

Improving the visibility of the prostate gland can further aid segmentation. To this end, various attempts have been made and reported in the literature. These vary from processing ultrasound B-mode images [85, 89], to the use of additional information from other modalities such as MRI [20]. Another recently developed option is the use of ultrasound elastography. Elastography has the ability to highlight differences in the mechanical properties of tissue, such as stiffness, therefore, it can be used for highlighting the prostate boundary since the gland and its periphery are known to have various stiffness values. However, it is important to evaluate the appearance of the gland in such images to determine the usefulness of these images in diagnosis and treatment of malignancies. For example, the volume of the prostate is an important measure for post-operative assessment in LDR brachytherapy. To be able to use elastography images for segmenting the prostate, it is required that the gland volume extracted from the images is valid, either being similar to that shown in a standard modality, such as B-mode, or the difference being known.

Furthermore, the ability to distinguish internal structures of the gland, especially cancerous tumors, can aid diagnostic and treatment methods. Guided prostate biopsy, with knowledge of lesion locations, can reduce the false negative rate in detecting cancer and the need for repeating the procedure. Additionally, localized treatment (e.g. surgical removal of the gland or LDR brachytherapy) as opposed to general treatment can be pursued when the location of disease is known. This can potentially reduce treatment side-effects.

In this thesis, which is based on the importance of developing tools which aid diagnosis and treatment of prostate cancer, two main topics are studied: *(i)* Segmentation of the prostate boundary and *(ii)* Visibility of the gland in elastography images. Chapters 2 and 3 present a prostate segmentation tool and Chapter 4 addresses the visibility of the gland in

vibro-elastography images. In Chapter 5 the methods and results of the aforementioned chapters are utilized to develop an automatic segmentation tool and finally, in Chapter 6 initial results of the appearance of prostate cancer in vibro-elastography images is reported and compared to other work.

1.2 Background

A literature review on various prostate segmentation methods is first provided in Section 1.2.1. Our proposed prostate segmentation algorithm is applied to and evaluated for prostate brachytherapy, hence, an introduction to low dose rate prostate brachytherapy is deemed necessary and is provided in Section 1.2.2. As an attempt to improve the visibility of the prostate, ultrasound elastography, more specifically vibro-elastography, which has been proposed in our group, is used for imaging the prostate. Section 1.2.3 provides an introduction and a brief literature review of ultrasound elastography and describes the data collection apparatus and the procedure for this method.

1.2.1 Prostate Segmentation

Various prostate segmentation methods have been proposed in recent years [76]. These can be classified into those which solely rely on image data, and those which incorporate prior information about the expected shape of the prostate. The advantage of not constraining the solution to certain geometrical classes may result in more robust segmentation of irregular prostate shapes and some prostate surface abnormal deformations that may be caused by cancer. Examples of image-based segmentation methods used in the literature are contrast enhancement, image smoothing and Canny's edge detector [85], multi-resolution discrete wavelet pyramids for coarse-to-fine segmentation [11] and the use of phase symmetry for outlining dominant edges which are then linked to create a final contour [123].

The disadvantage of methods that rely solely on image information is that they are more sensitive to factors such as image quality and noise, and generally require more effort to achieve reasonable results. Because they do not use prior shape data, a majority of the proposed general segmentation methods do not work on ultrasound images of the prostate. Deformable models such as active contour models (ACM) and snake models have been used widely for medical image segmentation. They are curves or surfaces of which the deformation (e.g. with the means of Gabor filters) is guided by internal forces (e.g. the constraint of the curve being smooth) and external

7

forces (e.g. edges in the image). Because they can not tolerate the large amount of noise in ultrasound images very well, for such methods to work, additional constraints must be imposed. For example, the deformation must be limited by an a priori shape, or alternatively, significant user interaction must be used [76].

Active shape models (ASM) [18] use shape models that deform within some constraints. These constraints and the initial shape model are derived, statistically, from a training set. [25, 39, 42, 45, 55, 72, 73, 87, 95, 105, 119, 125, 126]. Active shape models are used in the 2D segmentation method proposed by Hodge et al. [39]. This method is extended to 3D by using a rotational-based slicing method. After each 2D image is segmented, manual editing (required in 26.3% of the 2D images in each case) is allowed, after which the modified points are clamped and the model is re-deformed. They report an average mean absolute distance and maximum distance of 1.09 ± 0.49 mm and 7.27 ± 2.32 mm between manual (the average of three repeated manual delineations performed by three trained graduate students) and automatic contours (on 36 patient data sets). The average run time is reported to be 6.9 ± 2.1 minutes which includes the time needed for manual editing of the 2D images.

Yan et al. [117] use adaptive learning during segmentation, in addition to global population-based shape statistics for 2D segmentation of the entire gland in TRUS video sequences. Their adaptive learning method is reported to improve segmentation of the base and apex. They report a mean absolute distance of 1.65 ± 0.47 mm and a Dice similarity coefficient value of 0.91 ± 0.03 between automatic and manually delineated TRUS video sequences of 19 patients.

The use of ellipses, ellipsoids, superellipses and other similar shapes has been a relatively attractive approach for prostate segmentation as most prostates conform well to these representations, and the reduced parameter space results in fast segmentation algorithms. In the work by Kachouie et al. [46] the velocity of an evolving ellipse initially placed on the center of the prostate is guided by the first and second moments of the Gaussian probability density function fitted to the image histogram. However, further work is said to be needed for robustness to poorer images. Gong et al. [33] have used deformable superellipses; ellipses that can be deformed by adjusting their aspect ratio, squareness, tapering and bending. Their extensive comparison of manual and computer-generated contours on 125 prostate ultrasound images resulted in a mean error of less than 2 mm between computer generated and manual contours. The segmentation duration was reported to be less than 5 seconds for each 256×256 image on a Pentium 4 PC running at 2

GHz. However, this method only generates 2D contours.

In the method proposed by Badiei et al. [6] an ellipsoidal volume is generated. The method is based on fitting ellipses and ellipsoids with the aid of initial points defined by the user and the Interacting Multiple Model Probabilistic Data Association (IMMPDA) [2] edge detection technique. It has the benefit of being fast, owing to solving a convex problem, but often results in relatively large false positive regions mainly in the anterolateral and inferior regions of the gland. This is due to the tapering of most prostates both in the 2D transverse plane and in the 3D volume along the main axis from the base to the apex.

The need for using 3D models as opposed to 2D is specifically seen when the quality drops in some image slices, specially at the base and the apex. With the use of a 3D model and the higher quality mid-region images, contours can be generated for the lower quality base and apical images based on the shape of the mid-gland. Additionally, surface smoothness from one image to the other is more easily maintained. Amongst the many proposed methods for segmentation of the prostate in ultrasound images, only a small number offer 3D segmentation of the gland [3, 39, 41, 86, 113, 118, 125]. The method proposed by Penna et al. [86] uses Fourier ellipsoids as the 3D surface model. This method requires 90 seconds to create the prostate surface model and generate the solid models necessary for HIFU therapy planning. Of this duration, only 10 seconds are required to model the surface. Manual tracing of approximately 5 transverse and 3 sagittal images of the prostate is needed to initialize this algorithm, which, as reported, requires another 1.5 minutes and introduces operator variability that has not been quantified. In the work of Tutar et al. [113], 3D semi-automatic segmentation is based on fitting the best surface to a set of images under shape constraints. These constraints are derived by modeling the shape of the prostate using spherical harmonics. A measure of percent volume overlap (the intersection divided by the union of two volumes) between automatic and manual (average of three observers' manual contours) of 83.5% is reported on a data set of 30 patients, while the inter-observer variability is 82.8%. However, this method also requires the user to manually segment the mid-gland axial and sagittal contours for initialization. After initialization, the 3D prostate shape is identified in 1-4 minutes, of which the authors report initialization times of approximately one minute. In [125] Zhan et al. use a deformable model based on statistical matching of both texture and shape on 3D TRUS images ($256 \times 256 \times 176$ volume size, 0.312 mm/voxel). They report a mean overlap volume error of 4.16% compared to manual segmentation on six patients and a segmentation time of 3 minutes. Since their method is

applied to 3D TRUS images, how it would fare relative to a conventional prostate volume acquired with a brachytherapy stepper, where the slices are at 5 mm intervals (resulting in 8-12 images per case), is not discussed in the paper.

To conclude this section, it is worth noting that when evaluating a segmentation algorithm, it is important to measure the intra- and inter-observer variability in addition to accuracy. Unfortunately this is not commonly reported in the literature. These two measures provide information about the repeatability of a method when various individuals perform segmentation or an individual produces contours at different times. It also indirectly provides information about the data set used for evaluation. Authors each have their own set of images for assessment of their algorithm, hence direct comparison of reported accuracy numbers is not reasonable. Obviously a high quality set of images provides better results compared to a lower quality set. One set may have more challenging images than another and therefore, lower accuracy results. If the accuracy of a method, compared to the gold standard (usually manual contours) falls within the inter- and intra-observer variability measured from the same data set, this method can be regarded as a suitable replacement for manual contouring (needless to say, in terms of accuracy).

In this thesis, the presented 3D semi-automatic segmentation algorithm is based on fitting warped and tapered ellipsoids as the shape prior. Volumetric and dosimetric evaluation of this method as applied to LDR brachytherapy is then performed. Also, intra- and inter-observer variability of the method is studied. This method is partially automated with the use active shape models and stiffness information from vibro-elastography images.

1.2.2 LDR Prostate Brachytherapy

LDR brachytherapy is generally recommended as a treatment option for early stage and organ confined cancer [69]. Details of the procedure may differ among various centers, therefore, a more general description will be provided here and details specific to the method at the Vancouver Cancer Center (VCC) will be given in Chapter 3. Prior to the procedure, a volume study is performed in which transverse ultrasound B-mode images of the prostate are collected, usually in the transverse plane. A grid with marker spacing of 0.5 cm, a horizontal axis labeled as 'A a B a $\cdots$ G' and a vertical axis labeled '1.5 2.0 2.5 $\cdots$ 6.0' is overlaid on the images such that the prostate is symmetrical around the mid-line D and the most posterior aspect of the gland lies on or slightly below one of the horizontal grid lines

(usually 1.0, 1.5, or 2.0). The boundary of the prostate is then identified and a treatment plan is generated based on the prostate boundary. In some centers (such as VCC) a planning target volume (PTV) is created from the delineated prostate boundary (also known as the clinical target volume (CTV)), and is used to generate the treatment plan. The treatment plan specifies the locations of 50-160 radioactive seeds (depending on the PTV volume) placed selected grid points. Most or all of the seeds are placed at grid points falling within the boundary of the PTV. Two commonly used radioisotopes are ^{125}I [36] and ^{103}Pd [10]. The goal is to cover the PTV with the 100% isodose surface while maintaining tolerable dose to sensitive tissues such as the urethra and rectum, thereby avoiding complications such as urinary incontinence and erectile dysfunction. However, since an ideal dose distribution is not physically achievable, guidelines for allowable exceptions and maximum margins outside the PTV are given.

Commonly used parameters for evaluating the dose distribution are the $V_{100}, V_{150}, V_{200}$, where for example a PTV V_{100} of 98% means that the isodose surface providing 100% or more of the prescribed dose (a prescription being 144 Gy) covers 98% of the PTV. Ideally, the PTV V_{100} should be 100% whereas to prevent overdose, the V_{150} should typically be around 50-60%. Other parameters are the D_{80} and D_{90} which indicate the minimum dose recieved by 80% or 90% of the PTV. The shape of the isodose surface is also important. For example, at some centers, the 150% isodose generally has an upright horseshoe shape with very little margin at the posterior (to avoid overdosing the rectum) and the hollow region around the urethra.

The seeds are delivered via pre-loaded radioactive needles (typically, for monotherapy, 144 Gy for ^{125}I and 115-120 Gy for ^{103}Pd) through the perineum and guided by the TRUS probe and a template with guide holes that match the grid that was overlaid on the images during planning, placed in front of the perineum. Fluoroscopy may be used sparingly throughout the procedure to evaluate the position of the implanted seeds and evaluate the implantation process.

If treatment plans are created pre-operatively, the position of the TRUS probe is adjusted intra-operatively to provide images of the prostate similar to the pre-operative images. This is necessary due to the fact that the orientation (mainly due to patient positioning), shape and size of the prostate may change from pre-operative to intra-operative imaging sessions. Occasionally, despite the adjustments, the treatment plan may need to be updated by the physician by adding or relocating seeds to adhere to the changed prostate boundary. The adjustment of the images and the plan are usually performed manually, which is time consuming and not free from

error. These adjustments are of less concern if intra-operative planning, which has been established and is being used in some centers, is performed [1, 4, 71].

Many factors cause the implanted seed positions to deviate from the treatment plan. These include motion of the prostate during implantation of the seeds and changes in the size, position and shape of the prostate, which are effected by inflammation and progress of the disease (although this is not common), position of the patient between the volume study and treatment sessions, and pressure of the TRUS probe. Factors such as interference of the pelvic bone may also require the plan to be changed. As a result, post-implant dosimetry is recommended by the American Brachytherapy Society for all patients undergiong LDR permanent brachytherapy [70]. This is required to identify regions where less or more than the prescribed dose is delivered to the tissue. These regions mainly include the prostate boundary (for coverage) as well as the anterior rectum and prostatic urethra (for rectal and urinary morbidities), the neurovascular bundle and penile bulb (for erectile dysfunction) [19]. The standard imaging modality for post-implant assessment is CT where the seed locations, prostate and peripheral organ boundaries are defined. Parameters such as the prostate D_{100}, D_{90} and V_{100} are then obtained and compared to the intended dose distribution.

Figure 1.4 shows a snapshot of the software used at VCC for LDR brachytherapy treatment planning (VariSeed^{TM}, Varian Medical Systems Inc., Palo Alto, CA, USA) and 10 B-mode images of a sample prostate taken at various depths. In the selected image, at depth 5, the planning grid is overlaid on the image. Both the contours and the plan are symmetric about the D column of the template through which the center of the ultrasound probe passes. Guided by the CTV (red) and PTV (cyan), needles (hollow circles) and seeds (cyan) are placed at grid locations. Isodose lines are calculated and displayed based on the prescribed dose and the location of the seeds, here showing the isodose lines corresponding to 200%, 150% and 100% of the prescribed dose (in this case 144 Gy). Notice that the seeds are placed such that large doses are avoided in the center of the prostate, where the urethra lies, and in the posterior, close to the rectum.
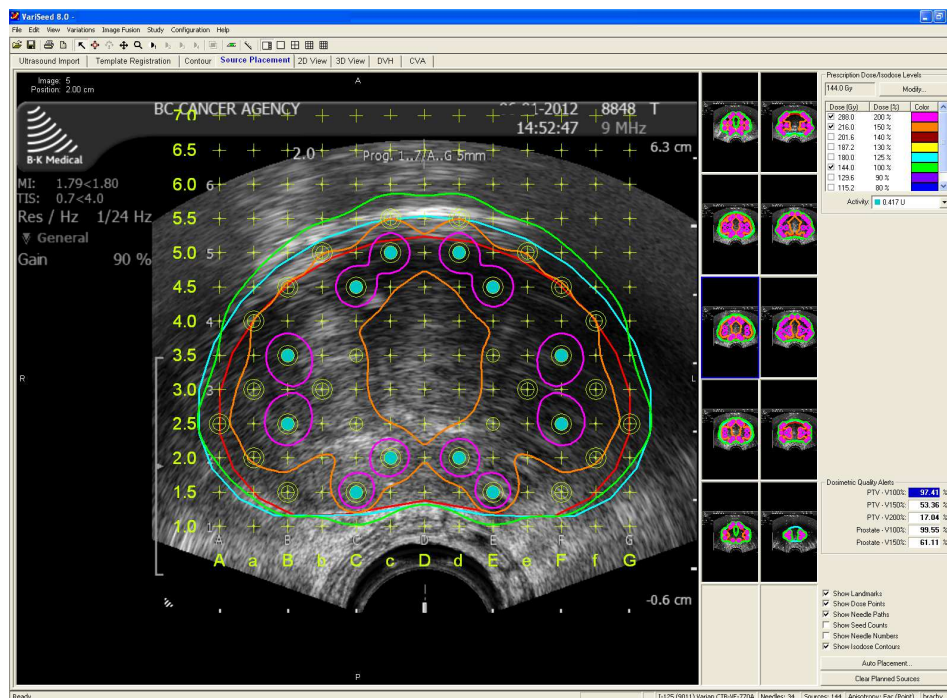
Figure 1.4: A snapshot of the software used for treatment planning (VariSeed^{TM}), showing the B-mode images of the prostate taken at 10 depths (smaller images at right). In the larger image, the CTV (red) and PTV (cyan), needle locations (hollow circles), and the seed locations (cyan circles) are shown. The 200%, 150% and 100% isodose lines are also displayed.

1.2.3 Ultrasound Elastography

Elastography [78, 79] is a promising technique for imaging soft tissues, it relies upon measuring tissue strain in response to excitation, and and is based on the fact that, when compressed, softer tissue will compress more than stiffer tissue, and therefore experience larger strain. Ultrasound, as a means for measuring tissue deformation, is a low-cost, portable, real-time and safe modality and therefore, widely used. Another popular modality for measuring tissue motion is MRI [67]. MR elastography (MRE) offers high sensitivity, a large field of view, and the ability to obtain full 3D displacement information throughout the 3D volume. Its applications are vast and still growing [44, 97, 120]. However, our main focus in this thesis will be ultrasound-based elastography.

Tissue motion can be achieved using external excitation, such as the inward motion of the ultrasound transducer in the image axial direction (usually strain levels of less than 2%), or internal excitation, such as from the natural motion of the cardiac muscle in myocardial elastography [52]. The type of excitation can be static/quasi-static, in which the tissue is slowly compressed and only the static behavior of the tissue, the stiffness, is measured [37]. In transient (impulsive or short tone burst) elastography, the propagation of a shear wave is imaged with parallel receive ultrasound [14, 103]. When the excitation is dynamic, the shear modulus can be estimated as a complex function of frequency, thus providing information on the viscoelastic properties of tissue [40].

During tissue excitation, ultrasound radio-frequency (RF) signals are collected and tissue motion is estimated. This is done in various ways such as cross-correlation techniques [79], peak searching methods [26], zero-crossing [100], and speckle tracking [77]. Alternatively, tissue vibration induced by the exciter can be measured with Doppler ultrasound [56], with larger vibrations corresponding to softer tissue. Motion estimation can be performed in 1D, in the direction of beam propagation where ultrasound resolution is higher, or the lateral and/or elevational directions resulting in 2D and 3D estimation [51, 53, 58, 103]. For more details related to the basics of elastography, various excitation techniques, and computation methods we refer the reader to [30, 35, 40, 80, 84, 88]. A concise review on the fundamental principles of elastography, developments in various categories of elastographic imaging in the last 20 years and recent clinical results, can be read in [83].

Clinical applications of elastography include, but are not limited to, breast lesions [32, 47, 57, 94, 97], liver fibrosis [13, 43, 120], vascular vulnerable plaque [93], elastic properties of skeletal muscle [23], thyroid gland
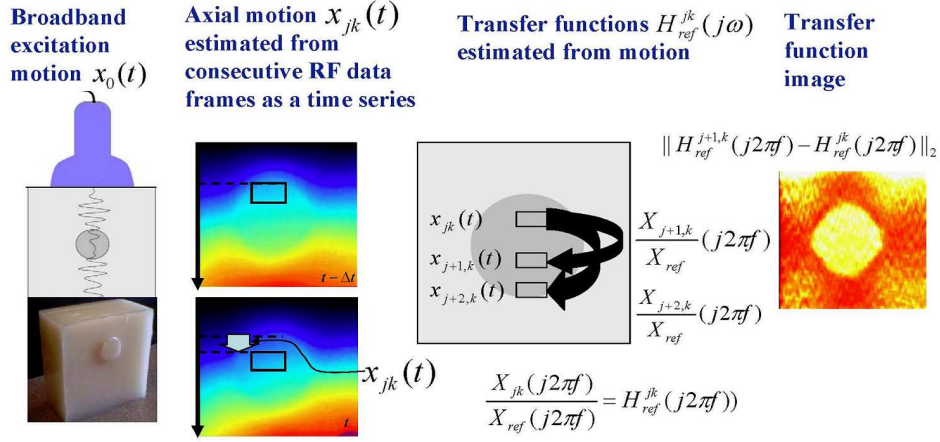
Figure 1.5: Schematic representation of vibro-elastography imaging. From left to right, a broadband external mechanical excitation $x_0(t)$ is applied to the sample; the axial motion $x_{jk}(t)$ of a tissue block indexed axially by j and laterally by k within the ultrasound image is obtained from RF images at time t and $t - \Delta t$; transfer functions from a reference to each of the tissue blocks are estimated, with the illustration showing the reference being the motion $x_{jk}(t)$ of block jk; images are produced by displaying the L_2-norm of the difference in transfer functions.

tumors [59], assessment of thermal tissue ablation [116], and detection of prostate cancer [16, 29, 34, 48, 65, 82, 99, 127]. A recent review on clinical applications of elastography is presented in [31].

Vibro-Elastography

Vibro-elastography is a dynamic ultrasound elastography method which models viscoelastic properties of tissue [112]. The approach is illustrated in Fig. 1.5. The technique relies on the continuous real time acquisition of unprocessed ultrasound echo data as a time series of 'radio-frequency' (RF) data images, while, simultaneously, tissue is externally vibrated with a mechanical excitation that generates low-frequency broad-band compression waves. A time-series of tissue displacement or strain images is computed from consecutive RF data images. The tissue displacement as a function of time at a given spatial location can be viewed as the output of a linear system whose input is the motion of the exciter as a function of time. Therefore a frequency response or Transfer Function (TF), $H_{ref}^{jk}(\omega)$, that relates

the tissue motion at any spatial location, x_{jk}, with the exciter motion as a reference, x_{ref}, can be computed in the frequency domain. Alternatively, if the exciter motion is not measured, a tissue region, typically in the focal area of the ultrasound beam, can be selected as the reference. The transfer function can provide elastic properties of tissue such as viscosity and stiffness. At zero frequency, $\left| H_{ref}^{jk}(0) \right|$ gives the amount of axial tissue deformation at location x_{jk} as a response to unit displacement at location x_{ref}. In order to reduce the displacement estimation errors, usually an average of the TF at low frequencies is computed instead of at zero frequency. In this sense, computing the stiffness based on the TF is superior to the static method. The reliability of the transfer function can be assessed using the corresponding coherence function, $C_{ref}^{jk}(\omega)$. Its value, being between 0 and 1, indicates what portion of the input energy at location x_{ref} at frequency ω appears as the output energy at location x_{jk} at frequency ω. A value of 1 indicates that the system is linear and the signal-to-noise ratio is high.

Figure 1.6 shows the transrectal ultrasound (TRUS) VE actuation system developed in our research group for VE imaging of the prostate. A LDR brachytherapy stepper (EXII, CIVCO Medical Solutions) was modified to enable acquisition of RF data volumes. The rotation of the cradle was motorized to enable smooth rotation of the TRUS transducer and a shaker was mounted on the transducer cradle in order to radially vibrate the TRUS probe. Figure 1.7 displays a close-up view of the motorized cradle. A PC-based control interface allows the user to control the rotation motion range (-45 to 50 degrees, 0 degrees being the mid-sagittal plane), the amplitude, and frequency range of the transducer vibration. Synchronized with the motion of the probe, frames of RF data are collected from a SonixRP ultrasound machine with the sagittal array of a dual-plane linear/microconvex broadband 5 - 9 MHz endorectal transducer (Ultrasonix Medical Corp.). The RF sampling frequency is 20 MHz.

For the collection of a majority of our data, the vibrating TRUS probe, with a vibration range of 2-10 Hz and vibration amplitude of approximately 1 mm, was swept from $-45°$ to $45°$ covering a fan of longitudinal planes passing through the axial transducer axis with a predefined angular separation. At each angle, one B-mode image and frames of RF data were collected continuously from which vibro-elastography images were created. Figure 1.8 displays the orientation of the fan of longitudinal planes at which data is collected, with respect to the prostate and TRUS probe. These planes, which we will simply refer to as 'longitudinal', pass through the transducer axis and include the mid-sagittal plane at angle $0°$.

16
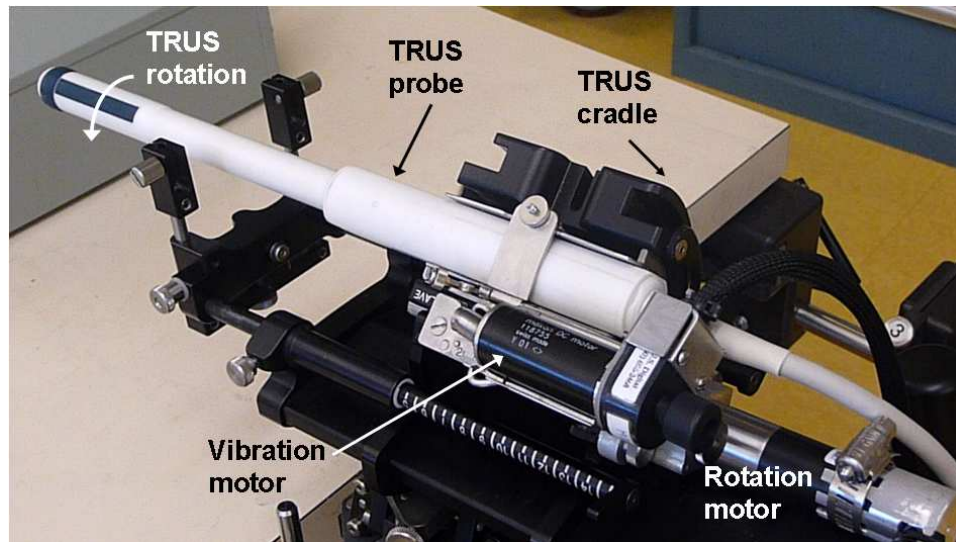
Figure 1.6: System setup for vibro-elastography data acquisition
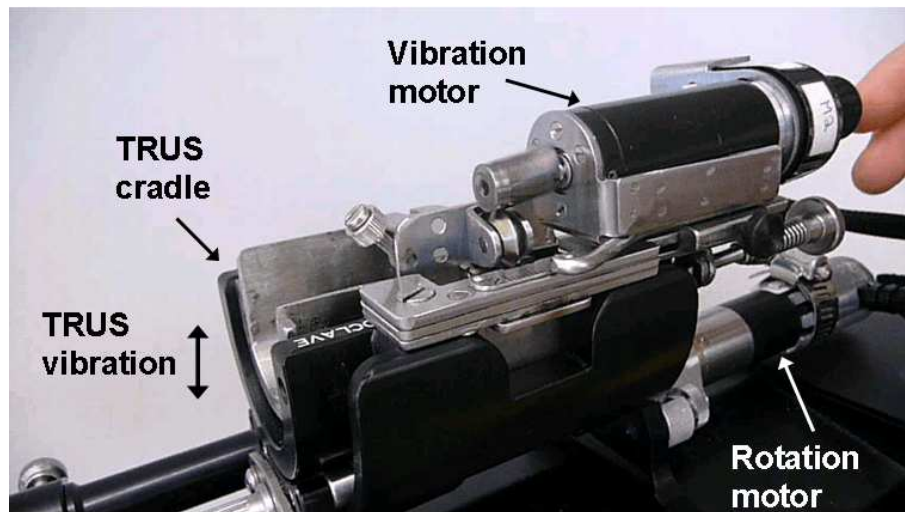
Figure 1.7: Details of the motorized cradle

Further details of the data collection and processing will be explained in Chapter 4.
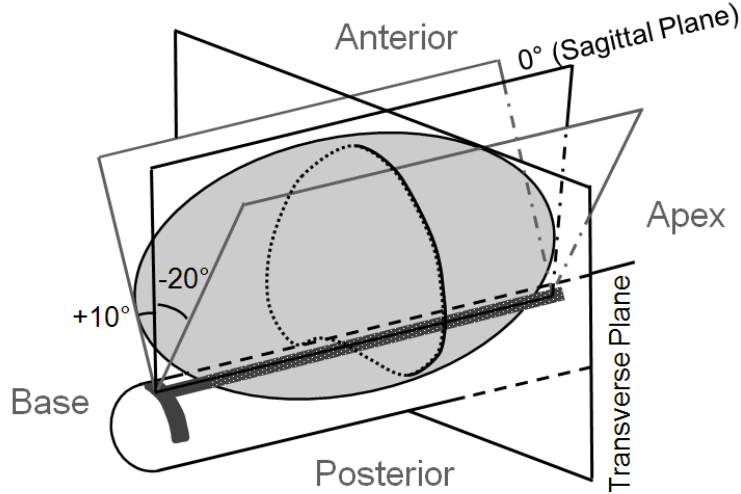
Figure 1.8: An illustration of the longitudinal planes at which data is collected, with respect to the prostate and TRUS probe. Here, the mid-sagittal plane, at 0°, and two other planes at angles of -20° and +10° are shown. The orientation of a transverse plane in the mid-gland is also displayed.

Appearance of the prostate in vibro-elastography images

Figure 1.9 shows a mid-sagittal and transverse image of the prostate as seen in VE. In general, the prostate appears as a darker (stiffer) structure compared to its periphery, with the prostate apex exhibiting more stiffness contrast with respect to the surrounding tissue. On the other hand, the base of the prostate has less contrast. This could be due to the anatomy of this region or the base merging into the bladder. Another possibility is that since the base is imaged using the distal end of the probe and the probe in motion acts like a cantilever, the desired excitation frequency may not properly propagate to the end of the probe. Hence, tissue in this region is not excited with the desired motion. Similar to B-mode images, it is sometimes possible to see the path of the urethra. This is seen as a softer (brighter) region passing from the base to the apex. A contrast between central and peripheral region of the prostate can be seen in some cases.
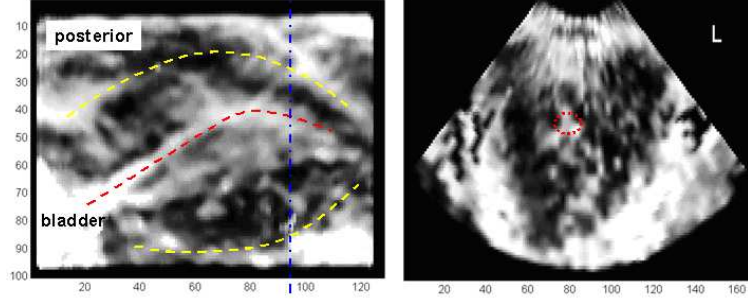
Figure 1.9: A mid-sagittal (left) and transverse (right) VE image of the prostate showing the urethra (dashed red). The prostate boundary is marked by the dashed yellow lines. The section from which the transverse image is displayed is marked by the dashed blue line.

1.3   Thesis Objectives

The specific objectives of this thesis are as follows:

1. Developing a clinically acceptable prostate segmentation method.

2. Evaluating ultrasound vibro-elastography as an imaging method for visualization of the prostate boundary.

3. Incorporating ultrasound vibro-elastography in the proposed B-mode-based prostate segmentation method to enhance segmentation.

4. Studying the feasibility of using ultrasound vibro-elastography as a tool for detecting prostate cancer.

In the course of achieving these objectives, the following contributions were made:

- A semi-automatic prostate segmentation tool was developed and is currently being used as part of the clinical procedure for prostate brachytherapy at Vancouver Cancer Center. It has also been introduced to other centers of the BC Cancer Agency.

- The proposed segmentation algorithm has been thoroughly evaluated both volumetrically and dosimetrically for nine regions of the prostate and has shown to be suitable for replacing manual delineation, which is currently the standard.

- Ultrasound vibro-elastography (VE) has been evaluated for prostate imaging. The shape and volume of the prostates shown in VE have been compared to ultrasound B-mode and with MRI as the gold-standard. Additionally visibility of the prostate boundary and the contrast of the gland in VE images have been compared to those of ultrasound B-mode.

- The fusion of information from vibro-elastography and B-mode images has led to the development of a fully automatic prostate segmentation algorithm.

- Groundwork for studying the visibility of prostate cancer in vibro-elastography images has been laid.

MATLAB$^{©}$ was the main environment in which algorithms are implemented. Visual C++$^{©}$ was also used for processing the RF data.

1.4   Thesis Outline

This chapter introduced the research topic, motivation for performing this research and the thesis objectives and contributions. Related background accompanied by an overview of the current literature of prostate segmentation, prostate brachytherapy, ultrasound elastography and prostate cancer detection methods has also been presented.

In Chapter 2, a semi-automatic segmentation method for delineating the prostate in ultrasound B-mode images is described. Volumetric accuracy evaluation of this method is performed by comparing semi-automatic contours with manual contours and physician corrected semi-automatic contours. Repeatability of the method is assessed by computing inter- and intra-observer variability in semi-automatic segmentation and comparing the results to inter- and intra-observer variability in manual contouring.

The proposed semi-automatic segmentation algorithm is clinically used for delineating the prostate in LDR brachytherapy. Since the goal of prostate brachytherapy is to deliver a sufficient amount of radioactive dose to the diseased prostate while sparing critical regions, it is important to assess the dosimetric impact of using the semi-automatic segmentation algorithm, as opposed to conventional manual contouring. This is the subject of Chapter 3.

In Chapter 4, visualization of the prostate in ultrasound vibro-elastography images is evaluated. Ultrasound B-mode imaging is well known for its poor

quality, especially at the prostate base and apex. Methods that improve visibility of the gland can greatly aid delineation and cancer detection. In this chapter delineated prostate surfaces from vibro-elastography images are compared to those of B-mode with MRI as the gold standard. The quality of edges and contrast of the images is also compared to those of B-mode.

Based on results obtained from Chapter 4, we concluded that vibro-elastography images are superior to B-mode in some aspects. In Chapter 5 the combination of information from ultrasound B-mode and vibro-elastography is used for developing a fully automatic 2D prostate segmentation algorithm, which is then used to automate the 3D semi-automatic segmentation algorithm proposed in Chapter 2.

Finally, in Chapter 6 we provide preliminary results of the visibility of cancer in vibro-elastography images. We suggest that although, at this stage, VE alone can not always be used for detecting cancer, it can potentially be combined with other image types for developing an automatic cancer detection method. This final chapter does not report peer reviewed contributions but provides tools and the foundation for future work in the area of cancer research.

Chapter 2

Semi-automatic Segmentation of the Prostate: Method Description and Volumetric evaluation

2.1 Introduction

In this chapter a semi-automatic prostate segmentation method for use in LDR prostate brachytherapy is proposed.

For an algorithm to improve the efficiency and consistency of the brachytherapy treatment, it needs to satisfy the following important requirements. First, it should be able to produce contours that are not distinguishable from those generated by medical practitioners. Second, it should produce contours that are amenable to the design of uncomplicated treatment plans. Third, it should not require considerable changes to the conventional clinical procedure. Moreover, a fast and automatic solution to manual contouring would greatly facilitate intra-operative planning, where additional and significant gains in treatment quality are likely to be realized.

In the proposed method, the boundary of the prostate in TRUS images is delineated based on prior knowledge of the shape of the gland, resulting in smooth, symmetric and less user dependent contours. The 3D geometric model of the prostate is created based on the assumption that the prostate has a tapered ellipsoidal shape and is slightly warped posteriorly due to the presence of the TRUS probe. Using an a-priori shape – in this case, a tapered, warped ellipsoid – aids segmentation in the less visible base and apex of the gland. Manual initialization of the algorithm makes use of the practitioner's experience. The simplicity of the algorithm and the formulation

of the most intensive part of the computation as a convex problem results in a fast, close to real-time, and repeatable segmentation method.

Symmetry and smoothness are two other desired features which greatly aid treatment planning. The use of symmetric contours with respect to the sagittal plane for treatment planning is an accepted practice at the BC Cancer Agency and some other centers. Symmetric contours lead to simple treatment plans that are also easier to change to ensure adequate dose coverage, should the shape, size and position of the prostate change significantly with respect to the volume study. A population study of biochemical and survival outcomes on a total of 1006 consecutive prostate brachytherapy interventions (July 1998 to October 2003) performed at the BC Cancer Agency, the institution where we collected the patient data, shows excellent oncologic outcomes for men with favorable-risk disease, with very low rates of biochemical or metastatic recurrence [66].

2.2 Methodology

Given a series of 2D trans-rectal transverse B-mode ultrasound images of the prostate, from the *base* to the *apex*, the goal is to generate a 3D volume of the gland in a real (or close to real) time, preferably using the least user interaction. The images are collected using a B&K Pro-Focus System B-Series machine (BK Medical, Peabody, MA), with the MFI Biplane Transducer. The image specifications are: image size 640×480 pixels, 0.155 mm $\times$ 0.155 mm 2D image pixel size, 5 mm image spacing. It is assumed that the prostate is positioned in the TRUS images such that symmetry is maintained with respect to the mid-sagittal plane. This is usually met since the current treatment planning procedure requires such a condition. If such a condition is not met, an initial rotation and translation can be easily applied to the images.

TRUS images of the prostate show posterior warping of the gland due to the presence of the TRUS probe. Additionally, tapering is often seen both transversally, toward the anterior aspect of the gland (creating a pointed appearance), and axially, with the gland narrowing toward the apex. Our method is based on the assumption of separability between the probe-induced warping, the tapering, and ellipsoidal fit, so that each can be handled independently. In doing so, the fitting and hence, the segmentation problem, is simplified into the convex problem of fitting an ellipsoid to the preprocessed data. Figure 2.1 shows a snapshot of the graphical user interface used in the Vancouver Cancer Centre for prostate contouring using the proposed

method. Figure 2.2 illustrates the main steps of the segmentation algorithm. Details of each step are presented below. We will hereafter and in Chapter 3 refer to the algorithm and the resulting contours as the 'Tapered Ellipsoid Segmentation algorithm' (TES) and 'TES contours'.
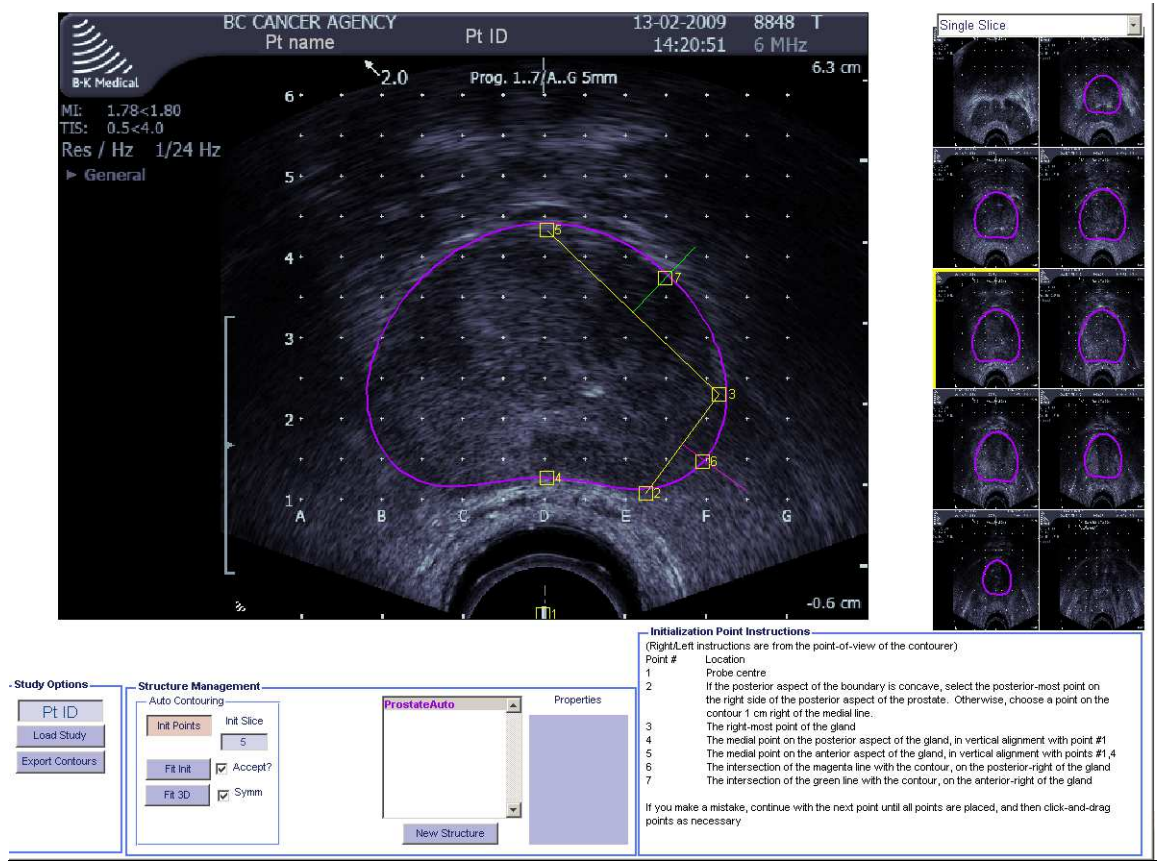
Figure 2.1: A snapshot of the graphical user interface for automatic prostate segmentation used at the Vancouver Cancer Centre.

p_5 p_7 p_4 p_3 p_6 p_1 p_2

| Initialization | → | Image un-warping | → | Image un-tapering | → | Mid-gland ellipse fitting |

| Semi-ellipsoid fitting | → | Slice contour propagation | → | Tapered ellipsoid fitting | → | Contour tapering, warping |
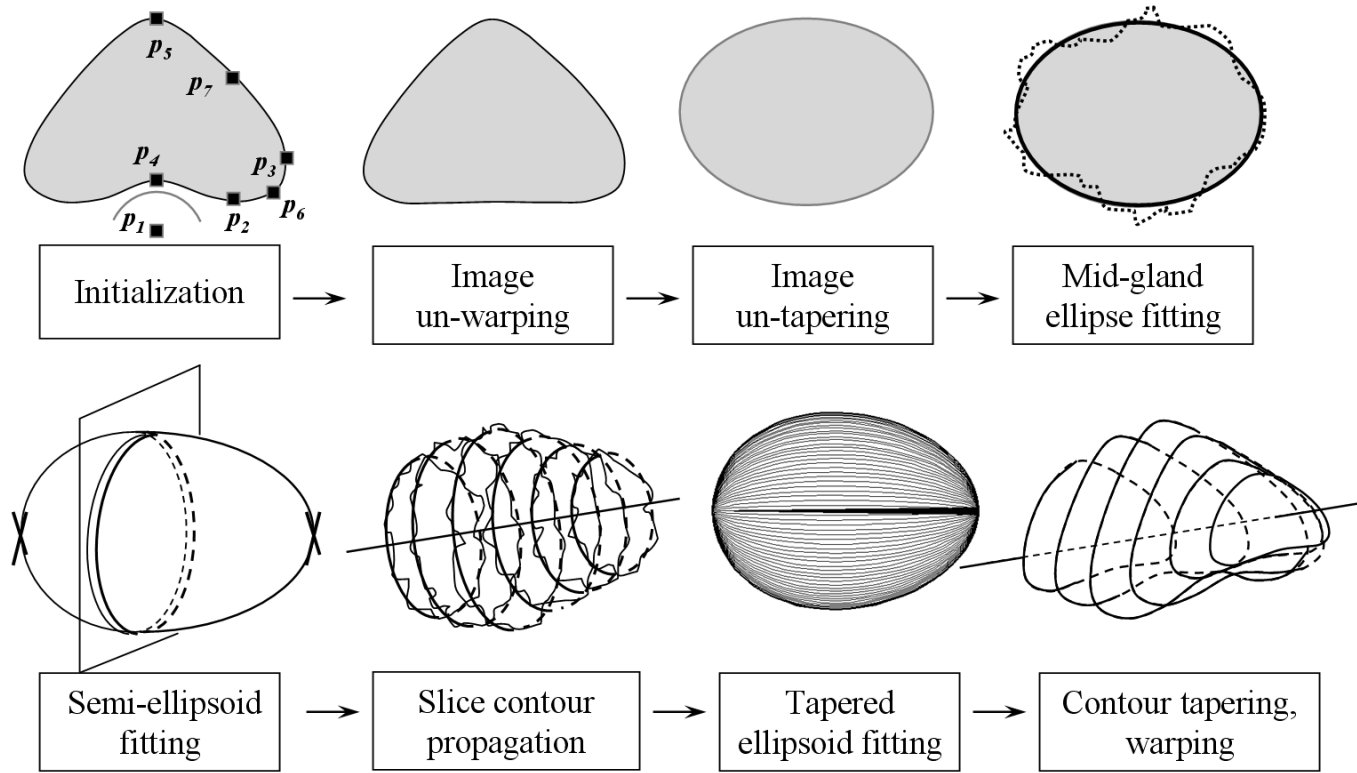
Figure 2.2: The main steps of the segmentation algorithm.

2.2.1   Algorithm

Initialization

A prostate volume study used for brachytherapy treatment planning consists of a set of transversal prostate images. Selection of the mid-gland, apex, and base images is the first step in the semi-automatic segmentation algorithm. The mid-gland image is where the initial 2D segmentation will be carried out. It contains the largest and most visible section of the gland. The base and apex are the extreme superior and inferior images of the prostate, respectively. They are not always visible in TRUS images, and will not be used in the TES algorithm. Their contours will be defined by projection of the final 3D shape on the respective planes. However, the depth of the base and apex images is important in order to extend the segmentation from 2D, on the mid-gland, to 3D. The term 'slices', hereafter, will refer to the images starting from image $base + 1$ to image $apex - 1$.

On the mid-gland image, the user selects six boundary points which, in addition to p_1 - the TRUS probe center, initiate the algorithm. These boundary points are: p_2-lowest posterior lateral, p_3-extreme right, p_4-mid-posterior, p_5-mid-anterior, p_6- intersection of the mid-perpendicular line between p_2 and p_3 with the boundary, and p_7- intersection of the mid-perpendicular line between p_3 and p_5 with the boundary (Fig. 2.3a). Points p_3, p_4, and p_5 are primarily determined by the size of the prostate. Points p_1, p_2, p_4 are used to calculate the amount of warping. Points p_6 and p_7 have the main contribution in determining the amount of tapering. The aim is to extract the most information from the image while keeping the variability of the point selection low by directing the user to specific regions; either to extremes (e.g. points p_3, p_4, and p_5) or by guiding lines (points p_6 and p_7). These points along with their symmetric reflections across the medial line will be referred to as the 'initial points'.

Image un-warping

Based on the initial points, the posterior region of the mid-gland image is un-warped to reduce the deformation caused by the TRUS probe using Eq.2.1 below. In this equation r is the current distance of an image pixel on a radial line starting from the probe center with angle ϕ ($\phi = 90°$ being the medial line) and r_{new} is the distance of the re-located pixel. In this sinusoidal Gaussian function, the maximum deformation is achieved when
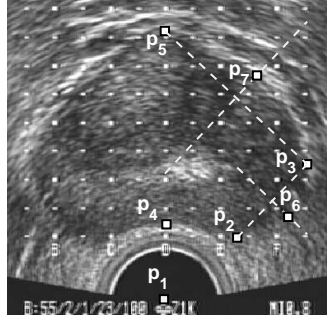
(a)
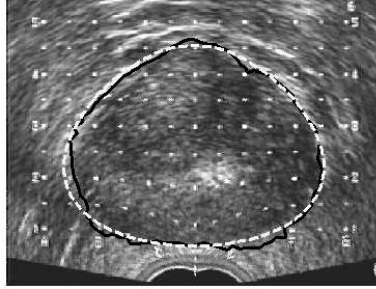
(b)
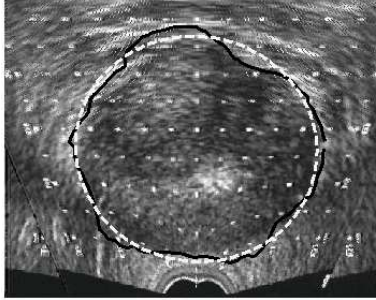
(c)

Figure 2.3: a) Initialization points, b) Image un-warping, IMMPDA edge detection and tapered ellipse fitting (dashed), c) Image un-tapering, IMMPDA edge detection and ellipse fitting (dashed).

$\phi = 90°$ and reduces as r increases.

$$r_{new} = r - r\sin(\phi)\exp(-r^2/2\sigma^2) \tag{2.1}$$

28

σ is a variable which represents the amount of radial stretch and is calculated by solving Eq. 2.1 for $\phi = 90^o$ to obtain:

$$\sigma = \sqrt{\frac{-r^2}{2\ln(1 - r_{new}/r)}}, \qquad r_{new} < r \qquad (2.2)$$

For this angle, r is set as the distance between p_1 and p_4 and r_{new} as the distance between p_1 and the reflection of p_4 about a horizontal line passing through p_2 . If $r_{new} > r$ no un-warping is required.

Eq.2.1 is also used to un-warp the initial points. Assuming that the presence of the TRUS probe causes uniform deformation along the prostate images, all the other TRUS images are also un-warped. Therefore, the effect of the TRUS probe on the gland is largely removed.

Image un-tapering and mid-gland ellipse fitting

The un-warped initial points are used to fit an initial tapered ellipse on the now un-warped mid-gland slice (Fig. 2.3b). The tapered ellipse parameters $P = (x_0, y_0, a_x, a_y, t_1)$ are found by solving the following problem using the recursive Levenberg-Marquardt algorithm [7]:

$$\min_P \left\{ e^T e \mid e_i = \sqrt{a_x a_y}[(\frac{x_i'}{a_x})^2 + (\frac{y_i'}{a_y})^2 - 1] \right\} \qquad (2.3)$$
$$x_i' = (x_i - x_0)/(\frac{t_1}{a_y}(y_i - y_0) + 1),$$
$$y_i' = (y_i - y_0)$$

with a_x and a_y being the radii along the axes, $-1 \le t_1 \le 1$ the tapering parameter and $[x_0, y_0]$ the center of the shape. $[x_i, y_i]$, $i = 1 \dots N$, are the coordinates of the boundary points with N being the number of initial points as previously defined. Figure 2.4 shows the effect of changing the tapering value, t, in a tapered ellipse from -1 (thick dashed line) to +1 (thick line).

Throughout this algorithm, 2D segmentation is carried out with the aid of the IMMPDA edge detector [2]. In this edge detector, the evolution of the radius from an arbitrary seed point inside the contour to the contour edge is modeled as a dynamic system in the radius angle. Multiple models can be incorporated in the dynamic system to accommodate abrupt changes in the edge. Two constant velocity models (Eq. 2.4) have been used in our approach.
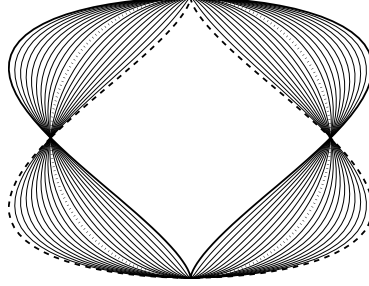
Figure 2.4: The effect of changing the tapering parameter from -1 (thick dashed line) to 1 (solid line). A tapering value of zero corresponds to an ellipse (dotted line).

$$X_j(k+1) = \begin{bmatrix} 1 & \delta\theta \\ 0 & 1 \end{bmatrix} X_j(k) + V_j(k) \qquad (2.4)$$

$$Z_j(k+1) = \begin{bmatrix} 1 & 0 \end{bmatrix} X_j(k) + \omega_j(k)$$

where $j = 1, 2$ is the number of trajectory models used to describe the boundary, $X_j(k) = \begin{bmatrix} d_j(k) & d_{\theta_j}(k)^T \end{bmatrix}$ are the system states at the kth radius in which $d_j(k)$ is the distance of the prostate boundary from the arbitrary seed point inside the prostate and $d_{\theta_j}(k)$ is its derivative with respect to angle θ. $V_j(k)$ is the process noise vector with covariance $Q_j(k)$. $Z_j(k)$ is the process output (measured boundary location) and $\omega_j(k)$ is the measurement noise with covariance $R_j(k)$. The two models used in our implementation have the following process noise vector and measurement noise covariances:

$$Q_1(k) = \begin{bmatrix} \delta\theta^4/4 & \delta\theta^3/2 \\ \delta\theta^3/2 & \delta\theta^2 \end{bmatrix} 10^1$$

$$Q_2(k) = \begin{bmatrix} \delta\theta^4/4 & \delta\theta^3/2 \\ \delta\theta^3/2 & \delta\theta^2 \end{bmatrix} 10^5$$

$$R_{1,2} = 20$$

where the numerical values have been obtained by trial and error in prior work [5, 6] and have not been adjusted for any of the patient data they

were used in. Each trajectory model is associated with a Kalman filter. The output of these filters is combined with a probabilistic data association filter for more accurate contour extraction. Since no numerical optimization technique is used in the IMMPDA method, it is fast enough to be used repetitively within a segmentation algorithm. Meanwhile, the interacting multiple model (IMM) estimator increases its accuracy and robustness when noise is present in the images. For further details please refer to [2]

The initial tapered ellipse fitted to the initial points is used to guide the IMMPDA edge detector by setting limits on how far from this contour the edge detector can search. These limits prevent the edge detection from drifting away from the prostate boundary in regions with low image contrast. The resulting edge points are once again fed to the Levenberg-Marquardt algorithm to obtain an improved fit of the tapered ellipse. The tapering value of this contour, t_1, is used to un-taper the ultrasound images. We assume that the prostate is most tapered at the mid-gland and the tapering linearly reduces to zero superiorly and inferiorly. Using the negative of the tapering value for each slice, all images along with the initial points on the mid-gland slice are un-tapered. The result of this step is transverse images in which the prostate has an elliptical shape.

An ellipse is fitted to the un-warped and un-tapered initial points. This can be done in many ways; we use the simple and fast generalized eigenvector solution of [114]. The ellipse guides the IMMPDA edge detector and to the extracted edges, a second ellipse is fitted on the mid-gland slice (Fig. 2.3c).

Semi-ellipsoid fitting for slice contour propagation

An IMMPDA edge detection and second ellipse fitting similar to that applied to the mid-gland slice is carried out on the rest of the slices. However, since there are no user defined points on these images, the initial ellipses are created by fitting two semi-ellipsoids; one that extends superiorly toward the base, and another inferiorly toward the apex (see Fig. 2.2). Each is fitted to the union of the data points on the mid-gland contour and the point on the intersection of the axial line passing through the center of the mid-gland contour with the respective $base - 1$, or $apex + 1$ slice. This is again solved as a generalized eigenvector problem. Two semi-ellipsoids were found to give a better initial approximation than a single ellipsoid because the prostate tapers more rapidly toward the apex.

The intersections of these two semi-ellipsoids with each of the slices are used to guide the subsequent IMMPDA edge detection on each slice. A line

is fitted to the centers of the resulting 2D contours. This line represents the main axis of the prostate and will be later used for re-aligning the final 2D contours.

Tapered ellipsoid fitting

At this stage, 2D contours have been generated from all un-warped and un-tapered images. Yet there is no guarantee that smoothness and continuity is maintained from one contour to the next, in the direction of the TRUS probe. Hence, a tapered ellipsoid with an elliptical cross-section and tapering along its main axis is fitted to these contours. Similarly to the 2D tapered ellipse fitting, $P = (x_0, y_0, z_0, a_x, a_y, a_z, t_2, t_3)$ is obtained by solving the following problem using the Levenberg-Marquardt algorithm:

$$\min_P \left\{ e^T e \mid e_i = \sqrt{a_x a_y a_z} \left[f(x_i, y_i, z_i, P) - 1 \right] \right\} \tag{2.5}$$

$$f(x_i, y_i, z_i, P) = (\tfrac{x_i'}{a_x})^2 + (\tfrac{y_i'}{a_y})^2 + (\tfrac{z_i'}{a_z})^2$$

$$x_i' = (x_i - x_0)/(\tfrac{t_2}{a_z}(z_i - z_0) + 1),$$

$$y_i' = (y_i - y_0)/(\tfrac{t_3}{a_z}(z_i - z_0) + 1),$$

$$z_i' = (z_i - z_0),$$

where a_x, a_y, a_z are the radii along the axes, $[x_0, y_0, z_0]$ is the position of the center of the volume and t_2 and t_3 are the respective x and y tapering values in the direction of the TRUS probe. $[x_i, y_i, z_i]$, $i = 1 \ldots M$ are the coordinates of the M boundary points generated by segmenting all image slices.

The fitting of this 3D shape to the boundary points is no longer a convex problem and is the most time consuming part of the algorithm. Suitable selection of the initial parameters can greatly reduce the search period and prevent the optimization algorithm from converging to local minima. To aid the optimization algorithm, the center of the 3D shape, $[x_0, y_0, z_0]$, and the axes, a_x, a_y, a_z, are determined by first fitting an ellipsoid to the data cloud consisting of the ellipse contours of all slices. Since this is a generalized eigenvalue problem, the one and only minimum is found almost instantly. The six derived parameters are used along with two tapering parameters, t_2 and t_3, initially set to zero to define an ellipsoid, as starting values for the optimization algorithm (Eq.2.5).

Contour tapering and warping

We have assumed that the prostate is parallel to the TRUS probe and not rotated about its main axis. This reasonable assumption simplifies the fitting problem since introducing three additional rotation parameters into the optimization algorithm will increase both the running time and the possibility of the algorithm converging to local minima. To take account of the possibility that the prostate may be slightly pitched or yawed, the best line fitted to the centers of the extracted 2D contours of all images before 3D shape fitting is used as the actual axis of the final 3D shape. After slicing the 3D tapered ellipsoid at the corresponding image depths, the centers of the final 2D contours are repositioned to align with this axis.

Finally, the repositioned contours are tapered and warped to match the original images (Fig. 2.5a, 2.5b). The negative of the same tapering values initially used to un-taper the images is used to taper the contours. However, to ensure that the posterior aspects of the contours do not overlap with the rectum, the warping parameter may need to be modified. When the mid-posterior point on the final contour is lower than the initial posterior point selected by the user, the σ is re-calculated using (2.2) but with r and r_{new} respectively set to the distance between p_1 and p_4 and the distance between p_1 and the mid-posterior point on the final mid-gland contour. This change in σ is only made if $r > r_{new}$, otherwise, the previous value of σ is used.

2.2.2 Evaluation

The presented semi-automatic prostate segmentation algorithm is currently being used by all the radiation oncologists who practice prostate brachytherapy at the Vancouver Cancer Centre, BCCA. Prior to treatment planning, initial delineations of the prostate, hereinafter called 'Raw TES contours', are approved and modified, if deemed necessary, by the radiation oncologist (RO) in charge of the patient treatment. We will call these approved contours, whether modified or not, 'RO reviewed TES contours'. The RO reviewed TES contours are used by medical physicists to generate a treatment plan, which in turn is again checked by the radiation oncologist before the actual implant takes place. Thus, while our semi-automated prostate segmentation is used to provide initial contours, these are not used for treatment without the treating radiation oncologists having the final say.

Modifications applied to the contours are not always due to segmentation errors, but are mainly required for brachytherapy treatment planning purposes, to ensure that the treatment plans created on these contours are
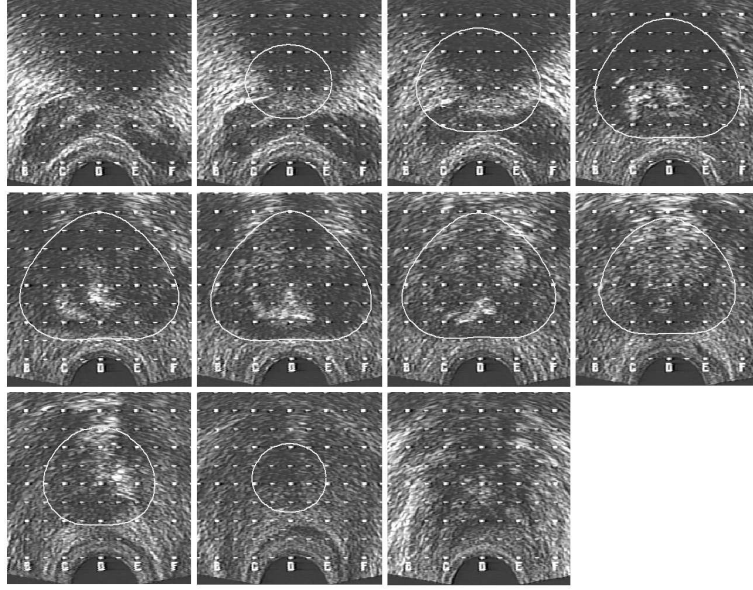
(a)
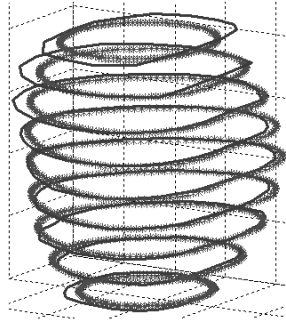
(b)

Figure 2.5: a) Final contours on the TRUS B-mode images, b) Final semi-automatic 3D volume (thick lines) compared to manual segmentation (thin lines).

robust and implantable. This is also observed in manual segmentation where the physician may not necessarily follow the prostate boundary, e.g. to avoid needle interference with the pubic arch or manage dose distribution in a certain region.

To evaluate this algorithm we have carried out two sets of studies: evalu-

34

ation of the accuracy of the algorithm, and evaluation of the repeatability of the algorithm. We start by comparing the semi-automatic contours before and after modification to indicate to what extent and in which regions the performance of the algorithm was not satisfactory for brachytherapy treatment planning. In order to understand how biased the physicians' modifications are by the initial semi-automatic contours, we compare the RO reviewed TES results with those of manual segmentation on the raw images. In order to evaluate our method based on a commonly used approach in the literature, we compare the Raw TES results with that of manual, generally used as the reference in the literature. In the next step we measure inter- and intra-observer variability of both manual and semi-automatic segmentation. A comparison of these two provides a judgment on the repeatability of the algorithm. The acceptable range for the segmentation error is provided by the intra- and inter-observer variability of manual contouring.

The term 'reference', used throughout this work refers to the prostate geometric shape relative to which the comparison is carried out. Depending on the study, this can be manual segmentation results, RO reviewed TES contours, etc. The term 'case' refers to a set of patient images. An 'observer' is an individual carrying out segmentation. All observers who perform contouring in this chapter have adequate knowledge in manual and/or semi-automatic segmentation and include an expert radiation oncologist, a radiation therapist and a graduate student with significant training in ultrasound prostate segmentation.

The comparison measures used are:

- Mean Absolute Distance, MAD : the average absolute radial distance between contours C_A and C_B, in a slice.

- Maximum Distance, $MaxD$: the maximum absolute radial distance between contours C_A and C_B in a slice.

Since the boundary of the prostate in the mid-gland slice is visible enough for accurate manual segmentation, these two measures are calculated for this slice only.

- Percent volume difference, V_{diff} : the difference between the volumes of two delineated prostates defined as:

$$V_{diff} = (V_A - V_{ref})/V_{ref} \times 100 \qquad (2.6)$$

in which ref in this equation is the reference and V denotes the volume.

- Percent volume error, V_{err} : the volume of the non overlapping region between two delineated prostates defined as:

$$V_{err} = |(V_A + V_B - 2(V_{A \cap B}))|/(V_A + V_B) \times 100 \qquad (2.7)$$

35

where V_{err} is in fact $1 - Dice\ similarity\ coefficient$ [21]. V_{diff} and V_{err} provide measures of size similarity and shape similarity, respectively. They are either calculated for the entire prostate, or for each of the nine sectors of the gland (Fig. 2.6). The nine sectors are created by first subdividing the prostate into posterior, anterior, and two lateral sectors, the latter of which are considered as a single region. The axis of division is the axis of the reference shape. These regions are then partitioned according to whether they are in the base, mid-gland or apex (respectively 0.3, 0.4, 0.3 of the length of the base-apex axis), forming a total of nine sectors for the purposes of analysis.
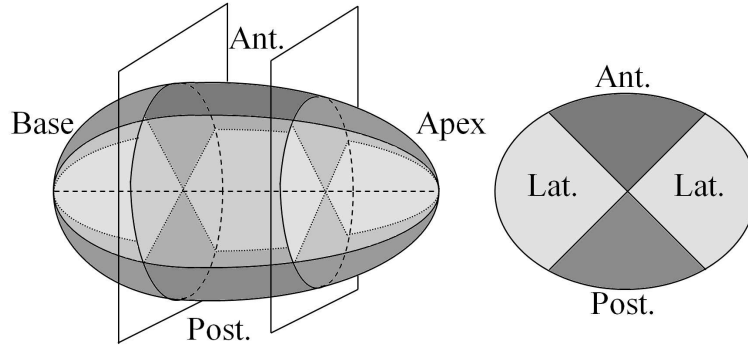
Figure 2.6: Division of the gland into nine sectors.

Quadrant-based division of the prostate is a common approach in the literature [96, 106]. However, for our application, this subdivision scheme provides more detailed reporting of results for different regions of the gland and is clinically motivated by the different consequences of segmentation errors with respect to treatment planning in these regions. For example, because the posterior aspect of the prostate is adjacent to the rectum, over-estimating the boundary there can result in high doses to the radiosensitive rectal wall and subsequently higher rates of rectal morbidity. This analysis aims to consider contouring performance in the context of treatment.

Accuracy

This consists of a comparison between 3D shapes generated from: (*i*) Raw TES contours and RO reviewed TES contours (the reference), (*ii*) manually segmented contours (the reference) and RO reviewed TES contours, (*iii*) manually segmented contours (the reference) and Raw TES contours.

Comparison between Raw TES and RO reviewed TES contours can give a measure of how satisfied the physicians are with the results of the algorithm and which regions of the prostate need the most modifications. It can indicate the degree to which semi-automatic contouring alone is successful in providing reasonable prostate contours for treatment planning. In this analysis, a total of 40 cases (randomly selected) was semi-automatically segmented by various radiation therapists and then modified by radiation oncologists (a similar study on a larger population of 140 cases is presented in [63]).

Modifications by the physicians to the TES contours may be biased by the initially given contours. To measure this bias, we compare manually created contours for 10 prostate image sets with RO reviewed TES contours, generated by three observers (one expert and two trained by experts) for the same image sets.

Finally, to include a commonly used method of evaluation reported in the literature, a comparison between prostate shapes generated by the TES algorithm and by manual segmentation, is also carried out. For this purpose, 21 cases were manually segmented by an expert and two individuals trained by an expert and the average of their contours was compared to TES segmentations of an observer experienced with the algorithm and blind to the manual contours.

Repeatability

This analysis is performed to evaluate the consistency of the contours across different observers and at different times. It consists of a comparison between (*i*) manual contours generated by different observers vs. the 'average' manual contour (the reference) and Raw TES contours generated by different observers vs. the 'average' TES contour (the reference) and (*ii*) initial Raw TES (the reference) vs. repeated Raw TES and initial manual (the reference) vs. repeated manual contours. For this aim, 10 cases were segmented by different observers once manually and once using the algorithm. Five of these cases were segmented again, both manually and using the algorithm, after approximately 2 weeks. All observers were blind to each others contours, their previous segmentations and patient data. (*i*) gives a measure of inter-observer variability and in (*ii*) intra-observer variability is quantified. Manual intra-observer and inter-observer variability also provide means of evaluating the accuracy obtained in the previous analysis.

The 'average' manual/TES contours are the average of the manually/TES delineated gland, by each observer, on each slice.
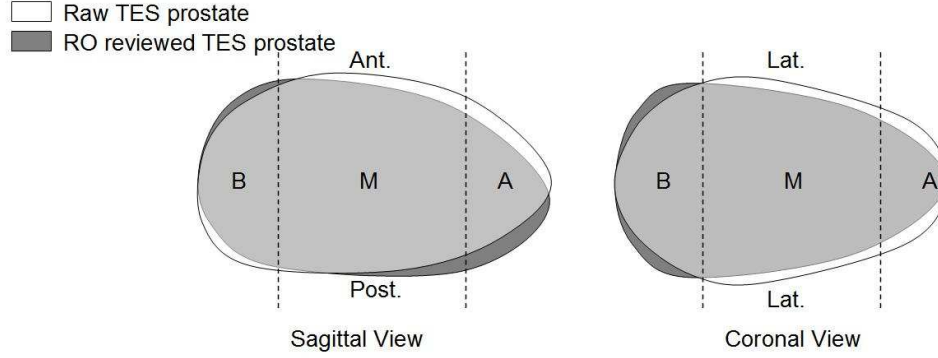
Figure 2.7: Schematic of changes made to each sector of the TES contours after modification as computed in Tables 2.1a and 2.1b (B: base, M: mid-gland, A: apex).

2.3   Results

The results of each evaluation study are as follows:

2.3.1   Accuracy

The mean and standard deviation of the percent volume error and volume difference between Raw TES (segmentation algorithm's results) and RO reviewed TES contours (expert approved contours used for treatment planning) are calculated for the nine sectors and the total gland and presented in Tables 2.1a and 2.1b. The average prostate volume created from Raw TES contours and RO reviewed TES contours is 42.2 ml and 41.5 ml, respectively. The average whole gland V_{err} of 5.82 $\pm$ 4.15% corresponds to a non-overlapping volume of 4.7 ml.

Whether these errors are clinically considered large or not will be determined in the following section. Based on these two tables, a schematic of the modifications made in each sector is drawn in Fig. 2.7. From the sagittal view it appears that on average, the algorithm over-estimates the mid-anterior, anterior-apex and posterior-base and under-estimates anterior-base, mid-posterior and posterior-apex. This may be a result of the algorithm not entirely capturing the tilt of the prostate. The coronal view shows that laterally, the size of the base is increased and the mid and apex are reduced in size after modifications.

The average MAD and MaxD between Raw TES and RO reviewed TES contours for the 40 cases on the mid-gland slice is 0.71$\pm$0.75 mm and

%	Base	Mid	Apex
Ant.	6.22 ± 8.18	5.14 ± 4.78	9.38 ± 9.40
Lat.	5.39 ± 5.10	4.65 ± 4.86	10.18 ± 8.99
Post	7.97 ± 8.07	4.52 ± 4.44	11.31 ± 14.42
Total		5.82 ± 4.15	

(a) V_{err}

%	Base	Mid	Apex
Ant.	-1.09 ± 19.67	6.75 ± 13.31	16.75 ± 30.02
Lat.	-2.22 ± 11.94	4.66 ± 13.74	12.91 ± 28.67
Post	11.13 ± 14.80	-4.33 ± 9.35	-13.05 ± 24.35
Total		2.11 ± 9.93	

(b) V_{diff}

Table 2.1: Comparison of prostate sectors created from Raw TES and RO reviewed TES contours showing the volume error (a) and volume difference (b).

2.00±1.87 mm with 11 out of the 40 mid-gland contours requiring absolutely no modifications.

Tables 2.2a and 2.2b show the average and inter-observer standard deviation of the absolute percent volume error and volume difference between manual and RO reviewed TES contours of 10 cases created by three observers. This comparison measures the amount of bias in the physicians' contouring when segmentation is done entirely manually as opposed to when initial TES contours are given to be approved. Most of the difference between the manual and RO reviewed TES contours is seen in the base and apex where visibility of the gland is low or absent. In these regions, the observer tends to rely more on the given TES contours. In the mid-gland region (which consists of over 50% of the prostate volume) the bias is lower and similar to the other computed errors for this region (Raw TES vs. RO reviewed TES and Raw TES vs. manual contours). A negative V_{diff} in all regions indicates that the prostate volume created from manual contours tends to be larger than that of RO reviewed TES. The average manually created volume is 55.6 ml and the V_{err} of $7.25 \pm 0.39\%$ corresponds to 8.2 ml.

Tables 2.3a and 2.3b show the absolute percent volume error and volume difference between manual and Raw TES contours created on 21 cases. The average MAD and MaxD between the manual and TES contours on the

%	Base	Mid	Apex
Ant.	7.65 ± 0.16	5.68 ± 1.50	8.66 ± 1.46
Lat.	10.52 ± 3.71	5.33 ± 0.52	10.17 ± 2.35
Post	13.97 ± 1.28	5.27 ± 0.54	14.05 ± 2.64
Total	7.25 ± 0.39		

(a) V_{err}

%	Base	Mid	Apex
Ant.	-1.15 ± 7.33	-0.98 ± 7.53	-6.75 ± 3.42
Lat.	-12.15 ± 4.14	-4.23 ± 3.59	-9.92 ± 3.99
Post	-11.56 ± 8.24	-2.44 ± 4.93	-13.71 ± 6.18
Total	-6.64 ± 2.36		

(b) V_{diff}

Table 2.2: Comparison of RO reviewed TES and manual prostate sectors showing the volume error (a) and volume difference (b).

mid-gland slice are respectively 1.38±0.61 mm and 3.49±1.10 mm.

%	Base	Mid	Apex
Ant.	7.77 ± 4.96	6.16 ± 4.08	11.27 ± 5.95
Lat.	6.45 ± 2.30	5.18 ± 1.40	9.59 ± 2.90
Post	7.71 ± 3.59	5.49 ± 2.66	11.83 ± 7.87
Total	6.63 ± 0.90		

(a) V_{err}

%	Base	Mid	Apex
Ant.	-0.92 ± 16.84	8.31 ± 13.57	2.79 ± 25.80
Lat.	0.23 ± 10.54	2.24 ± 6.98	1.08 ± 16.85
Post	3.63 ± 15.65	6.77 ± 9.92	0.19 ± 29.86
Total	2.43 ± 6.08		

(b) V_{diff}

Table 2.3: Comparison of Raw TES and manual prostate sectors showing the volume error (a) and volume difference (b).

Since the initial boundary points are selected on the mid-gland slice, and the mid-gland choice is not unique, we measured the sensitivity of the algorithm to the mid-gland slice selection. For this aim, 11 randomly selected

cases were semi-automatically segmented twice by an experienced individual. In the first round, the mid-gland slice was chosen as the first candidate, i.e. the largest and most visible image of the gland. In the second round it was selected as the next best candidate, one slice above or below the selection in the first round. The whole gland volume error between manually created surfaces and surfaces created using the best mid-gland candidate was 5.56±1.21% and between manually created surfaces and surfaces created using the next best mid-gland candidate was 6.96±1.81%. Finally, the whole gland volume error between the two TES surfaces with different mid-gland slices was 6.16± 2.16%.

2.3.2   Repeatability

Tables 2.4-2.7 show the inter- and intra-observer variability for manual and TES segmentation. In the presented tables, the mean and standard deviation (shown by the bars and error bars respectively) of V_{err} and V_{diff} are derived from the average performance of each observer over all cases (i.e. from the mean value of V_{err} and V_{diff} for each observer over all cases). It is the standard deviation that determines the observer variability in segmenting the prostate.

As shown in Table 2.4c and Table 2.5c, the inter-observer variability of TES contouring is less than that of manual segmentation in most of the sectors. The only sector in which manual inter-observer variability is less (as seen in both the V_{err} and the V_{diff} bar graphs) is the posterior-apex sector. Additionally, the relatively small manual V_{diff} mean values along with the large standard deviation values (Table 2.5) compared to that of TES, indicates that most regions of the prostate can be simultaneously over-estimated by some observers while under-estimated by the others in manual segmentation, whereas in TES segmentation, there is more agreement between observers in under-estimating or over-estimating different regions of the gland.

Figures 2.6c and 2.7c show the intra-observer variability in manual and TES contouring. As in inter-observer variability, in most sectors, intra-observer variability is less in TES contouring compared to that of manual. The sectors in which manual intra-observer variability is noticeably better are the anterior-apex and lateral-apex. However, similar to inter-observer variability, intra-observer variability is less on the entire gland in TES segmentation.

A comparison of manual V_{err} values in Table 2.4 and Table 2.6 with Table 2.1a shows that the error between the TES contours and those modified

%	Base	Mid	Apex
Ant.	9.62 ± 2.98	4.40 ± 0.83	5.47 ± 1.38
Lat.	5.77 ± 1.00	3.60 ± 0.69	5.36 ± 0.97
Post	6.73 ± 1.15	3.90 ± 1.40	4.93 ± 0.89
Total	4.65 ± 0.77		

(a) manual

%	Base	Mid	Apex
Ant.	3.32 ± 0.62	1.86 ± 0.30	3.59 ± 0.64
Lat.	3.26 ± 0.30	2.45 ± 0.48	4.64 ± 0.48
Post	4.95 ± 0.47	3.96 ± 1.02	6.21 ± 1.38
Total	3.04 ± 0.30		

(b) TES
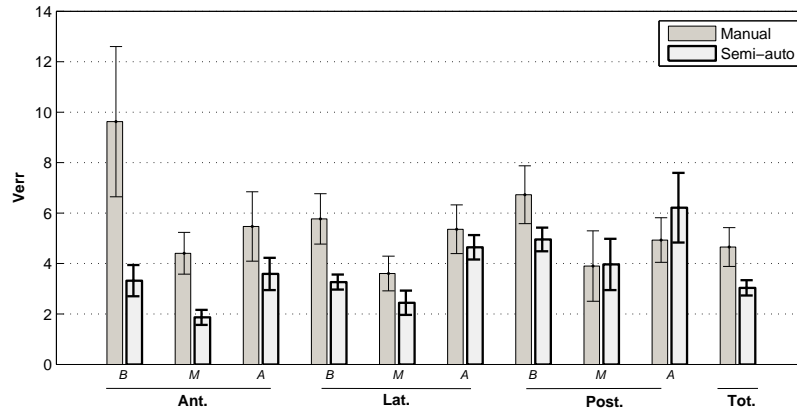
(c) V_{err} (%), manual vs. TES

Table 2.4: Inter-observer variability in manual and TES contouring - as characterized by the volume error V_{err} (Ant.: anterior, Lat.: lateral, Post.: posterior, B: base, M: mid-gland, A: apex, Tot.: total gland).

for treatment planning is in the order of the difference in the segmentations done by different observers or by an individual at different times. Therefore, based on the above results, it is reasonable to claim that if the TES contours were not to be modified by physicians and were to be used directly for treatment planning, they are just as likely to provide adequate results as manual or modified contours.

%	Base	Mid	Apex
Ant.	0.59 ± 16.91	-0.42 ± 3.89	-0.67 ± 6.75
Lat.	-0.01 ± 6.02	-0.41 ± 4.32	-0.24 ± 7.84
Post	-0.19 ± 6.13	-0.69 ± 7.80	-0.39 ± 7.43
Total	-0.31 ± 4.10		

(a) manual

%	Base	Mid	Apex
Ant.	-1.97 ± 3.12	-1.80 ± 1.11	-2.08 ± 2.87
Lat.	-1.07 ± 1.14	-1.10 ± 2.14	-0.65 ± 4.75
Post	-1.24 ± 4.59	-1.36 ± 4.93	-1.29 ± 7.86
Total	-1.23 ± 2.02		

(b) TES
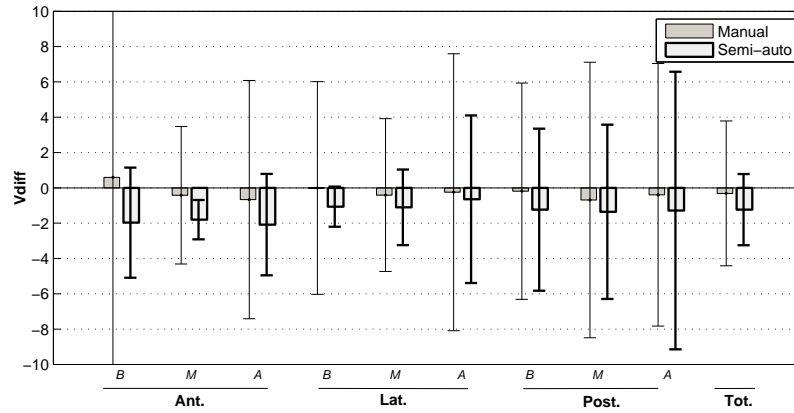
(c) V_{diff} (%), manual vs. TES

Table 2.5: Inter-observer variability in manual and TES contouring - as characterized by the volume difference V_{diff} (Ant.: anterior, Lat.: lateral, Post.: posterior, B: base, M: mid-gland, A: apex, Tot.: total gland).

2.3.3 Performance

The graphical interface used at the Vancouver Cancer Centre for semi-automatic segmentation gives the user the opportunity to modify the initial points to best fit a 2D contour to the mid-gland image. After approval of this contour, the algorithm proceeds to the 3D shape fitting. This can be repeated until a satisfactory delineation is achieved. The contours are then exported for further brachytherapy planning to the VariSeed software

%	Base	Mid	Apex
Ant.	9.77 ± 7.04	6.01 ± 3.19	7.99 ± 1.66
Lat.	6.65 ± 2.45	4.55 ± 1.36	7.73 ± 0.69
Post	7.20 ± 0.91	3.90 ± 1.43	9.75 ± 1.91
Total		5.95 ± 1.59	

(a) manual

%	Base	Mid	Apex
Ant.	4.30 ± 2.01	2.16 ± 0.40	5.20 ± 2.41
Lat.	4.07 ± 1.06	3.21 ± 0.86	6.18 ± 2.57
Post	4.23 ± 1.05	2.46 ± 0.90	6.04 ± 2.23
Total		3.48 ± 0.95	

(b) TES
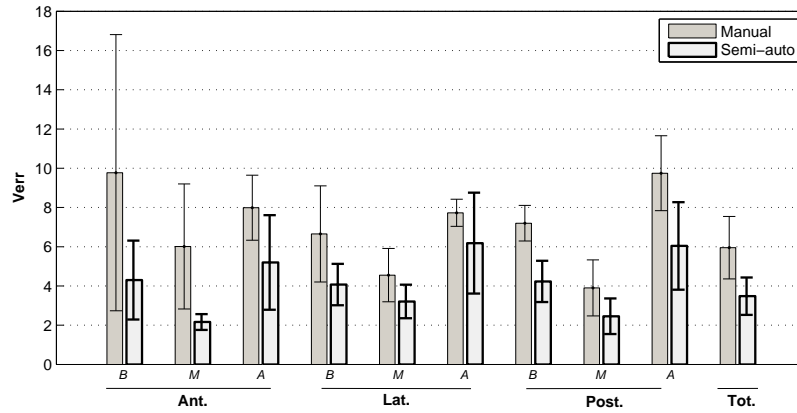
(c) V_{err} (%), manual vs. TES

Table 2.6: Intra-observer variability in manual and TES contouring - as characterized by the volume error V_{err} (Ant.: anterior, Lat.: lateral, Post.: posterior, B: base, M: mid-gland, A: apex, Tot.: total gland).

(Varian Medical Systems, Palo Alto, CA).

The average duration of the TES segmentation per case (calculated for the 40 cases used in the accuracy study), from after initialization until the final contours are created is 14.36 ± 1.39 s on a standard PC (Intel Xeon CPU, Intel; Santa Clara, CA, 2.27 GHz, 3.23 GB RAM). Of this duration, the most time-consuming sections are the 3D tapered ellipsoid fitting, being an iterative process (2.72 ± 0.27 s), and the image un-warping of all

%	**Base**	**Mid**	**Apex**
Ant.	11.59 ± 7.51	8.09 ± 5.17	8.84 ± 2.97
Lat.	-4.22 ± 5.98	3.88 ± 4.03	2.59 ± 8.02
Post	-4.60 ± 5.15	2.57 ± 5.45	-5.31 ± 6.38
Total	2.29 ± 3.74		

(a) manual

%	**Base**	**Mid**	**Apex**
Ant.	3.55 ± 7.20	1.60 ± 1.13	0.98 ± 8.07
Lat.	1.20 ± 5.48	1.42 ± 3.98	3.11 ± 9.71
Post	-0.74 ± 6.85	-1.11 ± 2.08	-2.76 ± 2.94
Total	0.90 ± 2.83		

(b) TES
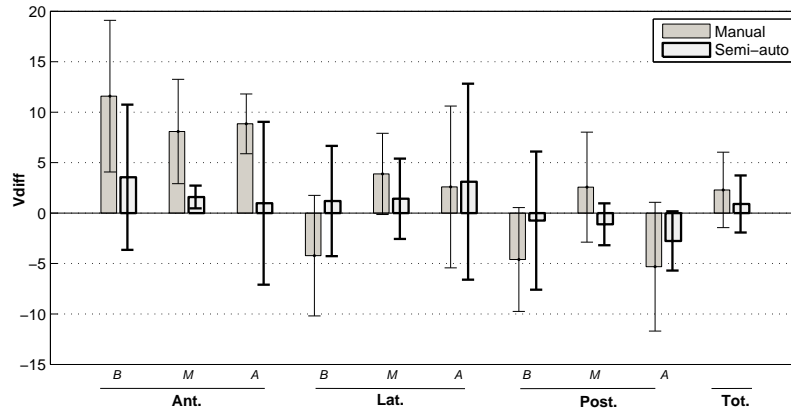
(c) V_{diff} (%), manual vs. TES

Table 2.7: Intra-observer variability in manual and TES contouring - as characterized by the volume difference V_{diff} (Ant.: anterior, Lat.: lateral, Post.: posterior, B: base, M: mid-gland, A: apex, Tot.: total gland).

TRUS images (4.23 ± 0.38 s). However, with further code optimization, these durations can be reduced. The selection of the initial slices and the 7 initial points requires 32.3 ± 14.0 s for someone familiar with TRUS images of the prostate. The physicians using the results of this algorithm have reported an average modification time of 1-3 minutes. Their modifications are reported to mainly consist of shifting or changing the overall size of the contour (especially the base and apex) which is done with ease in the

VariSeed software. Based on the above, the total segmentation duration, including initialization, is less than 1 minute. Including contour modifications for prostate brachytherapy purposes, it is expected to fall within the range of 2-4 minutes.

The time required for manual segmentation varies between users, and depends on their experience. An experienced radiation oncologist requires approximately 5-10 minutes per case to perform manual segmentation. Clinical fellows, during training, require up to 30 minutes for manual segmentation, but reach the 5 to 15 minute range after 1-3 months of brachytherapy training. However, a study to measure manual prostate segmentation time has not been performed

By visual observation of the pre- and post-modified contours, it was seen that out of the 369 segmented images of 40 patients, 28% needed either absolutely no modification (26%) or very little modification (2% - contour displacement of 1 mm or less).

2.4 Discussion and Conclusions

In this chapter, we presented a semi-automatic prostate segmentation algorithm in TRUS images and performed various clinical studies to evaluate the algorithm. Clinical results show that the inter-observer and intra-observer variability of the semi-automatic contours are less than that of manual contours in most sectors. The regions in which the variability is higher in semi-automatic segmentation is mainly the apical region of the gland. Comparison of Raw TES and RO reviewed TES contours shows a percent volume error of $5.82\pm4.15\%$ on the entire gland which is comparable to both the manual inter-observer ($4.65\pm0.77\%$) and manual intra-observer ($5.95\pm1.59\%$) variability. Comparison of RO reviewed TES contours and manual contours, a measure of physician bias when modifying the contours, shows a percent volume error of $7.25\pm0.39\%$ for the whole gland. The duration of segmentation after initialization has been reduced from a few minutes (as seen in the literature) to less than 15 seconds (14.36 ± 1.39 s). By including the initialization and possible modification time, the total segmentation time is less than 4 minutes. With the above results, we conclude that the proposed semi-automatic prostate segmentation method is accurate and consistent enough to replace manual segmentation of the gland. By applying slight modifications, such as removing the need for manual initialization, this method has the potential to be used as a real-time intra-operative segmentation method. This is the subject of Chapter 5.

We observed that poor image quality could in some cases lead to unsatisfactory results. However, the algorithm is guided by the manually selected initial mid-gland boundary points and the positions of the base and apex, from which initial contours and surfaces are produced. Since the edge detection is performed within a certain limit of these initial contours and surfaces, artefacts inside the prostate, such as calcifications should not pose a problem and, as long as the image quality at mid-gland is adequate for the observer to perform initialization, our method should provide consistent results.

The region-based volume measure of physicians' modifications applied to our semi-automatic contours (Fig. 2.7) suggests that our tapered ellipsoid shape assumption is reasonable. Other models based on priors could also be implemented, and may improve segmentation in terms of accuracy. For example, a statistically obtained prostate model, which includes possible prostate shape abnormalities (e.g. due to tumors), would be a good choice. However, in addition to possibly increasing the segmentation time, such a model will complicate the process of treatment planning and treatment modification, as the plans may be assumed to change continuously with the parameters describing the prostate shape. A tapered ellipsoid parameterizes the shape with only a few parameters that are intuitive and easy to understand.

As per the BCCA protocol, the contouring algorithm assumes that a smooth and symmetric clinical target volume is the aim of the oncologist, who consequently positions the prostate symmetrically across the mid-sagittal plane during TRUS image acquisition. The use of symmetric contours for treatment planning is widely practiced as part of the popular Seattle preplanning technique [102]. Symmetric contours lead to simple treatment plans that are also simple to modify to ensure adequate dose coverage should the shape, size, or position of the prostate change significantly with respect to the volume study. By maintaining symmetry during the preoperative volume study, reproducing the prostate image intra-operatively is relatively simple since the body's long axis can be identified easily in the dorsolithotomy position and does not change over time or in response to shifting leg positions and tissue relaxation. However, replicating a specific arrangement of misalignment is not easily accomplished since there are numerous ways to misalign the axes of the TRUS probe and the prostate, each of which creates a somewhat different visual pattern of asymmetry on the TRUS images. We emphasize the need to maintain proper body alignment throughout both the TRUS image acquisition and intra-operatively since, in most cases, maintaining this is sufficient to achieve symmetry on all slices. Effective implementation of a symmetric planning approach is demonstrated

47

by the results of a population-based analysis that showed only 35 recurrence events among the first 1006 consecutive BCCA prostate brachytherapy patients who underwent implant between July 1998 to October 2003 [66].

Since the semi-automatic segmentation algorithm is currently being used in practice (to this date, more than 1000 patients have been treated based on our segmentation method), it is possible to analyze the growing collection of segmented prostate images. The existance of any pattern or bias in the modifications could also be studied. Finally, we suggest the formation of a complete, randomly selected standard clinical data set. A comparison of the available segmentation methods on such a data set may be a suitable topic for further work.

Chapter 3

Semi-automatic Segmentation of the Prostate: Dosimetric evaluation

3.1 Introduction

In this chapter we provide a clinical validation of the tapered ellipsoid segmentation (TES) method from chapter 2.Currently, the semi-automatic contour is first approved and modified, if required, prior to treatment planning. The volumetric results in chapter 2 suggested that such modifications are so minor that they may not be necessary in many cases. Indeed, a volumetric study showed that the semi-automatic segmentation error is within the range of inter- and intra-observer variability of manual contours in most regions of the prostate, which suggests that on average, no greater variation is introduced by utilizing the algorithm than would be expected if a different oncologist performed the contour. Here, we aim to show that the segmentation error leads to a dose error that is negligible. The dosimetric comparisons were designed to investigate what the impact on coverage of the RO reviewed PTV would have been if planning had been performed directly on the Raw TES PTV. To do this, treatment plans were originally created on Raw TES contours, while satisfying the BC Cancer Agency (BCCA) planning goals, and subsequently superimposed on the corresponding RO reviewed TES contours. Plans derived from Raw TES PTVs were also compared to the plans created on the manual contours of different observers on the same image set. Details of each of the evaluation methods are described in the following sections. The terminolgy used below is defined in Chapter 1.2.2.

3.2 Patient Characteristics and Treatment Planning

LDR brachytherapy is indicated at the BCCA for low and intermediate-risk prostate cancer (all of: pretreatment prostate-specific antigen [iPSA]≤20, Gleason score [GS]≤7, clinical stage [CS]≤T2c [International Union Against Cancer (UICC) 1997]). Three to four weeks before the implant, a radiation oncologist performs a volume study in which 2D ultrasound images are obtained at 5 mm intervals with the use of a trans-rectal ultrasound probe (B&K Pro-Focus System B-series ultrasound machine; BK Medical, Peabody,MA, with the MFI Biplane Transducer, 640×480 pixels image size, 0.155 mm × 0.155 mm pixel size). The patient is in the dorsal lithotomy position during imaging. For applying the TES algorithm on these clinical images appropriate institutional and ethics committee approval have been obtained. The TES algorithm is initiated by a radiation therapist to produce a clinical target volume (CTV) called the 'Raw TES CTV'. The contours are then transferred to the treatment planning system (VariSeed, Varian Medical Systems, Palo Alto, CA) where they are modified if necessary and then approved for planning by a radiation oncologist (RO). This volume will be referred to as the 'RO reviewed TES CTV', which is used to produce the planning target volume (PTV). For the purposes of comparing the dosimetric effect of the RO modifications, a second PTV was also generated directly from the Raw TES CTV, which will be referred to as the 'Raw TES PTV'. The guidelines for the creation of the PTV at this institution recommend applying 0.3 to 0.5 cm lateral, 0 to 0.3 cm anterior, and 0.5 cm superior margins to the CTV. No planning margins are added posteriorly or inferiorly to spare the rectum and penile bulb. Although small variations in the size of the margins were present among clinically generated PTVs, the margins applied to generate the Raw TES PTVs for this study complied with the guideline recommendations (0.3 cm lateral, 0.2 cm anterior, and 0.5 cm superior). An additional component of this study involved the use of contours that were generated completely manually (i.e. without the presence of any preliminary contours on the image sets) by multiple blinded observers (radiation oncologists, radiation therapists and/or individuals trained by experts). We will describe these contours and their derivative structures as 'manually' generated to distinguish them from the 'RO reviewed TES' contours which are initially produced by the TES algorithm.

Brachytherapy treatment plans were developed for the PTVs by a single medical physicist. These plans adhered to the standard BCCA plan-

ning algorithm, which can be generally described as following a low-activity (0.424 U) modified peripheral loading strategy using custom loaded, stranded seeds (RAPIDStrand, Oncura, Arlington Heights, IL). The goal is to have the 100% isodose (the surface at which the radiation dose measures 100% of the prescribed dose) cover the PTV on all slices. Since this is not usually achieveable, guidelines are provided for maximum and minimum margins as well as allowable exceptions. These guidelines may vary from one center to the other. At VCC, each plan is designed to provide ≥97% coverage of the PTV and ≥99% coverage of the CTV by the 100% (144 Gy) isodose, with a CTV V_{150} between 56 and 65% and PTV V_{150} between 50 and-60%. The V_{150} is geometrically biased to the posterolateral aspects of the target. The volume that does not reach prescription dose in planning is confined to a small region of the anterior base of the PTV whenever possible.

3.3 Evaluation Measures

The following measures were used for dosimetric evaluation of the TES method. These measured were calculated for nine sectors of the prostate as described in chapter 2.

The standard dose parameter, V_{100}: the volume of the PTV receiving ≥ 100% of the prescribed dose, computed for the nine sectors of the PTV and the whole PTV. These values were calculated by the VariSeed software.

The External Index 150, EI_{150}: To characterize extraprostatic dose, the External Index (EI) [92], defined in Equation 3.1, measures the amount of tissue external to the PTV that receives doses 150% of the prescribed dose.

$$EI_{150} = (isoV_{150} - V_{150})/V \qquad (3.1)$$

$isoV_{150}$ is the total volume of the 150% isodose surface, V_{150} is the volume of the PTV receiving ≥150% of the prescribed dose (the volume of the intersection between the $isoV_{150}$ and PTV surfaces) and V is the volume of the PTV. Ideally, EI_{150} is zero.

The Conformity Index 100, CI_{100}**:** A 3D extension of the conformity index (CI) defined by Otto and Clark [81] is used, which measures both under-coverage of the target as well as over-treatment of the normal tissues.

$$CI_{100}\% = 100 \times \frac{V_r - (V_u + V_h)}{V_r} \qquad (3.2)$$

where V_r is the volume of the PTV (or one of its nine sectors), V_u is the volume of the PTV (or one of its nine sectors) that is receiving less than 100% of the prescribed dose and V_h is the volume of the region outside the PTV (or one of its nine sectors) that is receiving $\geq 100\%$ of the prescribed dose. A maximum conformity index of 1 shows perfect conformity of the 100% isodose to the region being observed.

We would like to note that although the above mentioned dose parameters are computed to evaluate the TES method, the planning process places quantitative constraints only on the whole prostate and whole PTV V_{100}, V_{150}, and V_{200} (i.e. a constraint of V_{150} between 50 and-60% is for the whole PTV, not a region). On the other hand, regional PTV coverage by the 100% isodose, location and shape of the 150% isodose, and the extent of extraprostatic dose are evaluated and constrained on the basis of visual (qualitative) inspection of the isodose distributions, rather than by adherence to regional constraints on V_{100} or CI_{100}. Hence, in this study, we refer to the values of the dosimetric parameters in each region, after planning, as the *observed clinical baselines* (which do not necessarily adhere with the whole PTV constraints) and compute the dosimetric *paired differences* from these observed clinical baselines in each region rather than reporting the absolute values.

3.4 Dosimetric Evaluation of the Algorithm

3.4.1 Impact of Planning using TES Contours

The aim of the dosimetric evaluation is to examine the clinical impact of planning using Raw TES contours. This helps to put differences in volumetric coincidence in perspective, because if such differences do not result in a significant degradation in dosimetry when a TES-derived plan is used to treat a reference contour, then it is reasonable to suppose that the TES and reference contour are of equivalent utility for planning purposes.

To investigate this, 41 anonymized consecutive patients (seen between January-April 2009) had treatment plans generated using their Raw TES PTVs as described in the "Patient characteristics and treatment planning" section. The aforementioned dose parameters for these plans were calculated for the PTV and the nine sectors and used as the observed clinical baselines.

These plans were then overlaid on the reference (RO reviewed TES) contours, and the resulting dose parameters calculated for the PTV and the nine sectors. The distribution of *paired differences* in the dose parameters was calculated (i.e. dose parameter of the plan generated using Raw TES PTVs and overlaid on RO reviewed TES PTVs minus the *observed clinical baseline* values).

3.4.2   The Effect of Contour Variability on Planning

Although the impact of TES-based planning is readily calculated, establishing a sensible threshold for the acceptable amount of dosimetric degradation below which the adoption of TES-based planning is unacceptable is challenging. For example, a plan with a whole PTV V_{100} below 97% would not be accepted for implant at our institution, so it may seem natural to set this as a target for TES-based planning. However, the patient might have been seen by any of a number of oncologists, none of whose plans are explicitly required to meet the 97% criterion on the contours of their colleagues. To avoid a double standard, the evaluation of any automatic contouring algorithm cannot ignore the implicitly accepted differences in dosimetry which arise from the endemic variability in target definition between observers. Consequently, TES-based planning in this study is evaluated in this context, by elucidating the range of variability in dosimetric quality that is entirely attributable to manual inter-observer variability, and then examining how the impact of TES-based planning compares to this range. This is performed in two tests. First, in a subset of five (of the 41) cases, the treatment plan produced on the set of contours originally used in the patient's treatment was overlaid on the contours of all 10 observers with the exception of the implanting radiation oncologist. In the second test, in one of the 41 cases, the set of plans produced on the 10 observers' PTVs were mapped back on to the original planning PTV. In all of these tests, the observers were radiation oncologists, blinded to their colleagues' contours. In this study we argue that if TES-based plans fall within the range of manual variability, it is reasonable to conclude that planning on the Raw TES CTVs is as reliable, in a statistical sense, as planning on the contours drawn by a colleague.

3.5   Results

Figures 3.1 and 3.2 display the paired differences in the V_{100} and CI_{100} when the plans created on the Raw TES PTVs are mapped to the RO reviewed

TES PTVs. In both figures, each data point represents the difference in the respective dose parameters for each of the 41 cases, for each sector of the gland as well as the whole PTV. Overlaid on the raw data are the means and 95% confidence intervals. Where this interval does not include zero, the impact is considered to be statistically significant, and the corresponding p-value is displayed for each region. The greatest impact on V_{100} was seen in the anterior base, anterior apex, posterior base and posterior apex. In all regions except the anterior base and apex, a statistically significant decrease in V_{100} was found (p<0.05). For the whole gland, the mean PTV V_{100} fell from 98.62±0.12% (observed clinical baseline), to 96.45±0.70% when the Raw TES derived plans were applied to the RO reviewed TES contours.

With respect to CI_{100}, variability in the CI_{100} was most pronounced in the apex and lowest in the mid-gland. The greatest mean decrease was observed in the anterior apex, which is consistent with the volumetric analysis establishing a tendency of TES to over-contour this region (see Table 2.1). However, in neither this nor any other region was there a statistically significant impact on the CI_{100} (p>0.05). For the PTV as a whole, the mean CI_{100} of 0.68±0.02 fell to only 0.66±0.3 when the Raw TES derived plans were mapped to the RO reviewed contours.

The mean and 95% confidence interval of the PTV 150% isodose external index EI_{150} (data not shown), increased from 0.065±0.004 (range 0.037-0.109) to 0.072±0.010 (range 0.025-0.160), a statistically insignificant increase in extra-target dose (p=0.22). The most significant increases (p<0.05) in the EI_{150} were in the mid-anterior (0.01±0.004 to 0.02±0.01, p=0.03) and lateral apex (0.21±0.02 to 0.27±0.06, p=0.04). However, significant decrease (p<0.05) in the extra-target dose was observed in the lateral base (0.18±0.02 to 0.15±0.02, p=0.00) and posterior base (0.10±0.01 to 0.07±0.01, p=0.000). No significant changes were observed in other regions.

The planning goals in our center require a CTV V_{100} of 99% or greater and a CTV V_{150} between 56 and 65%. Out of the 41 cases, 11 (27%) had a CTV V_{100} less than 99%, 3 of which were less than 98% (96.0%, 97.8% and 97.3%). In 6 of these 11 cases the CTV V150 was also below 56% (range 50.3-55.9%).

Substantial variability in dosimetric coverage and conformity arising from manual variability in target delineation is evident in Figs. 3.3 and 3.4, which look at the V_{100} and CI_{100} parameters respectively. The subfigures in each case indicate whether the reference plan was (a) mapped to other observers' PTVs, or (b) other observers' plans were mapped back to a reference PTV. The reference PTV and plan were those of the oncologist who treated the patient. For the test in which there was a reference plan, the figures show the mean and 95% confidence intervals of the dose parameter resulting from the application of the reference plan to each of 10 alternate contours produced by the other observers. This was repeated for five cases, and a mean and interval is shown for each of these cases, for each region of the gland. For the test in which there was a reference PTV, only one of these five cases was analyzed (the second of the five cases shown in Figs. 3.3a and 3.4a), and so only a single interval is shown in each region. The raw data points associated with the data derived from manual contours are hidden in order to highlight the relationship between the special case (marked by the triangle symbol) in which the test involved the Raw TES PTV or its derived plan, with the distribution of manual variability (i.e., using the Raw TES PTV or its derived plan instead of the manual PTV or its derived plan, in each test).

Extensive inter-observer and inter-case variability of the V_{100} in the anterior base, anterior apex, posterior base, and posterior apex and of the CI_{100} in the apex is noticeable. It is clear from the figures that in most of the examined situations, the impact on dosimetric quality resulting from utilizing the TES algorithm is indistinguishable from the mean impact expected when using another observer's contours. In many cases where the impact is not within this range, the degradation is less pronounced when using TES contours than its manual alternatives.

A one-way analysis of variance test confirmed that in most regions of the prostate in the test of a reference plan (Figs. 3.3a and 3.4a), the dose distribution accuracy of the plans created on Raw TES PTVs, in terms of the V_{100} parameter, was better than, or indistinguishable from that of the manual distribution. The exceptions are in the anterior base and anterior mid regions in three of the five cases ($p<0.05$). In terms of the CI_{100}, the TES results are superior in almost all regions of the prostate for all five cases ($p<0.05$) with the exceptions of the anterior base in two cases and the mid-posterior and posterior apex sectors in another. For the tests in which there was a reference PTV (Figs. 3.3b and 3.4b), the majority of the TES results are either superior to or fall within the manual variability of the manual results. The exceptions are in the anterior base for the V_{100} and

55

in the anterior base and mid posterior sectors for the CI_{100}.

It is clear from the figures that the dose parameters computed from overlaying the reference treatment plan on contours from different observers greatly differs from overlaying their plans on the reference treatment contour (compare Figs. 3.3b and 3.4b with the second of the five cases in Figs. 3.3a and 3.4a). For this case, the V_{100} values in Fig. 3.3b are in general less than those in Fig. 3.3a. However, the opposite is observed for the CI_{100} values in Fig. 3.4. This was expected since the radiation oncologist who created the reference treatment plan for this case tends to create larger PTV's. Thus, the plans created on the other radiation oncologists' contours, can not completely cover the reference treatment PTV, resulting in lower V_{100} coverage. However, the reference plan created on the relatively large PTV, when overlaid on other radiation oncologists' manual contours, will result in overdose. This is confirmed by more regions having negative CI_{100} values in Fig. 3.4a. Therefore, it is important to consider the dynamics of both parameters in evaluating impact, especially if only one of the above two tests are performed. Looking at V_{100} in isolation obscures the inherent bias towards over-treatment, as a plan generated for a high volume target is more likely encompass the volumes of other observers and result in good coverage.
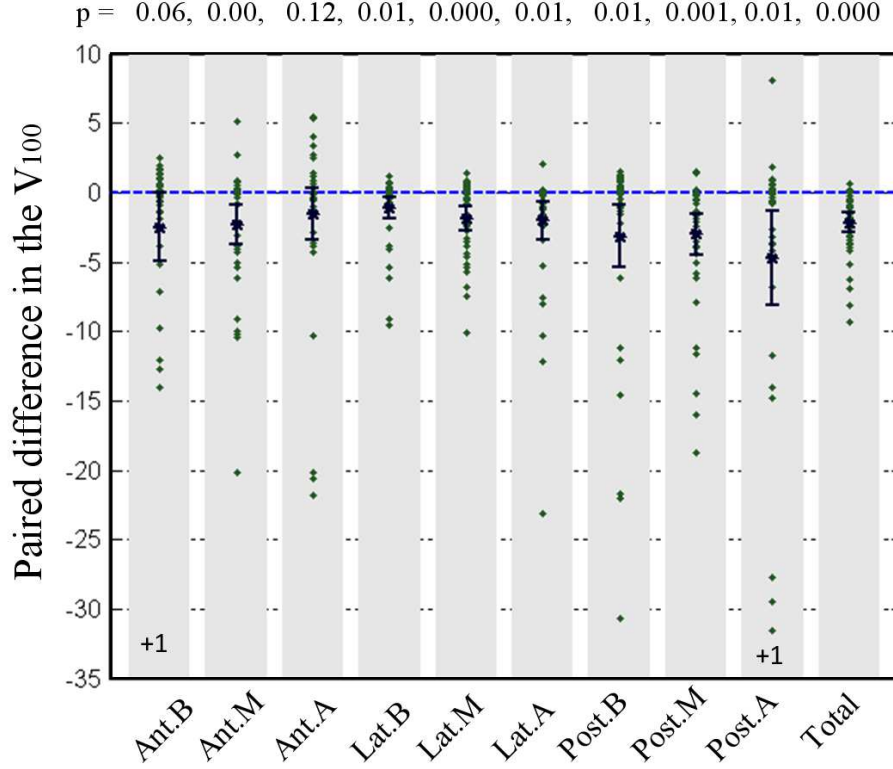
Figure 3.1: Plot illustrates the means and 95% confidence intervals of the paired difference in the V_{100} when the treatment plans generated based on Raw TES PTVs are overlaid on RO reviewed TES PTVs (i.e. V_{100} of the plan generated on Raw TES PTVs with respect to the Raw TES PTVs, the observed clinical baselines, subtracted from V_{100} of the plan generated on Raw TES PTVs with respect to the RO reviewed TES PTVs). A negative result indicates a decrease in V_{100}. Each column of data represents a particular region, labeled at the bottom. Each data point represents the result of each of the 41 cases analyzed. The p-values for a null-hypothesis of no effect in each region are presented at the top of the figure. Two data points fall outside the range of this figure, and are indicated by '+1'. Their values are -46.5% (anterior base) and -50.4% (posterior apex). A statistically significant reduction in V_{100} is evident in most regions, although the mean magnitude of the reduction is less than 5% (Ant.: anterior, Lat.: lateral, Post.: posterior, B: base, M: mid-gland, A: apex).
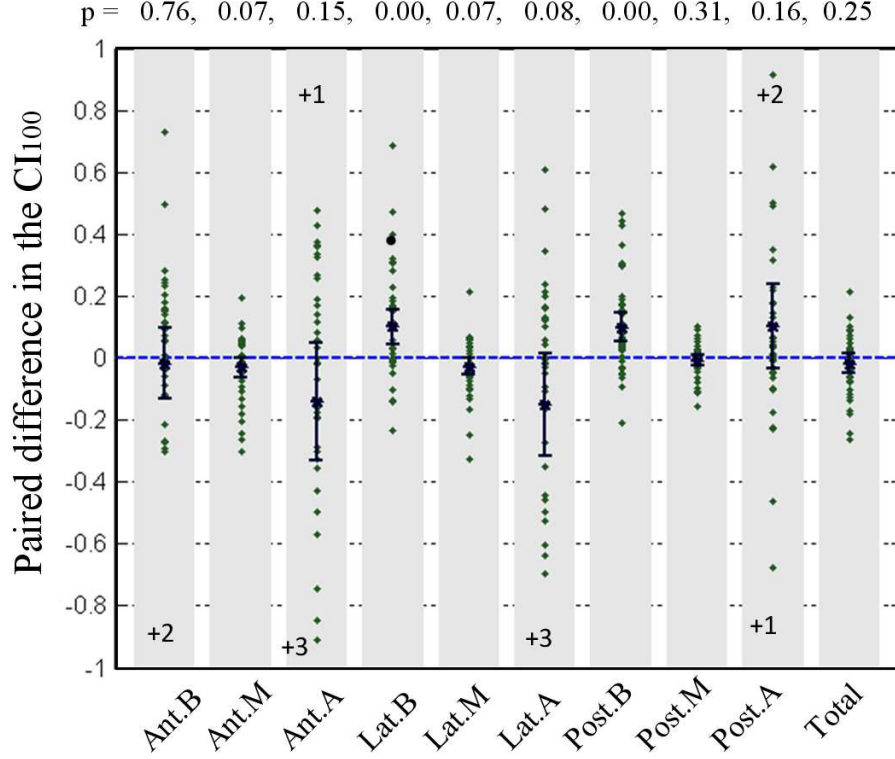
Figure 3.2: Plot illustrates the means and 95% confidence intervals of the paired difference in the CI_{100} when the treatment plans generated for Raw TES PTV's are overlaid on RO reviewed TES PTVs (i.e. CI_{100} of the plans created on Raw TES PTVs with respect to the Raw TES PTVs, the observed clinical baselines, subtracted from the CI_{100} of plans created on Raw TES PTVs and overlaid on RO reviewed TES PTVs). Each column of data represents a particular region, labeled at the bottom. Each data point represents the result of one of the 41 cases analyzed. A negative value result indicates a CI_{100} less than that of the observed clinical baseline. The number of data points falling outside the displayed range in each region, are indicated. The range of values for these four sectors: Ant. B, Ant. A, Lat. A, and Post. A, are: [-1.70 0.73], [-2.32 1.36], [-2.10 0.61], and [-1.24 1.49]. The lateral base and posterior base exhibit a statistically significant increase in conformity (Ant.: anterior, Lat.: lateral, Post.: posterior, B: base, M: mid-gland, A: apex).

(a)
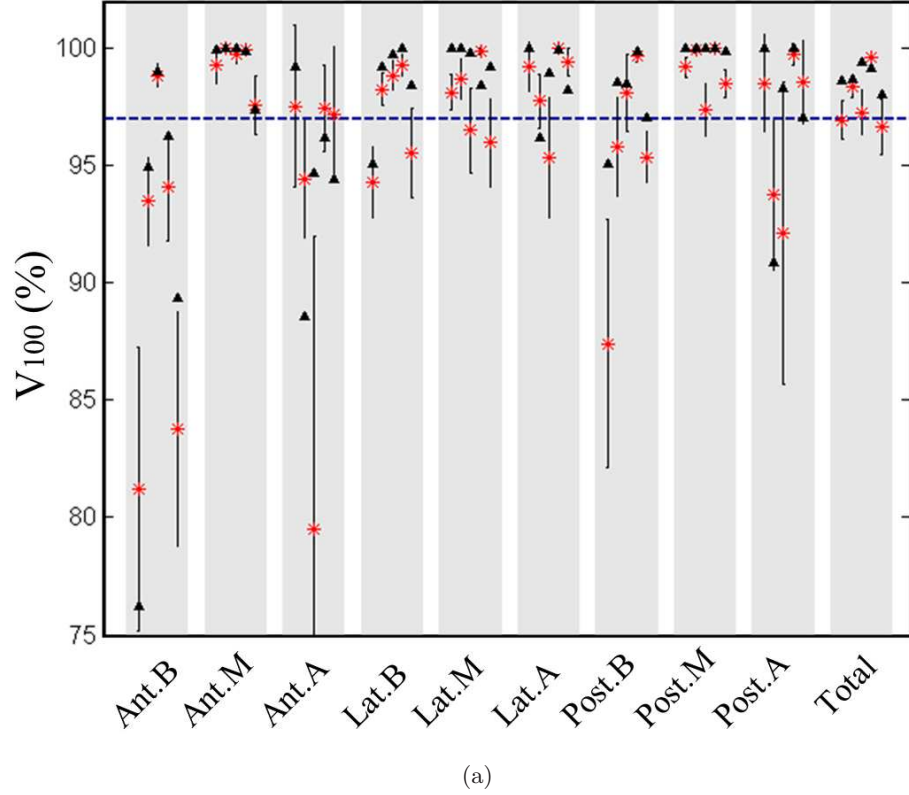
Figure 3.3: The means and 95% confidence intervals of the V_{100} when (a) a reference plan, created for one set of contours, is overlaid on the manual contours of 10 other observers in 5 patients. The typical goal V_{100} goal of 97% is shown as a dashed horizontal line. For comparison, the results of performing the test using the TES contours or their derived plans are displayed using the triangle symbols (Ant.: anterior, Lat.: lateral, Post.: posterior, B: base, M: mid-gland, A: apex).

(b)
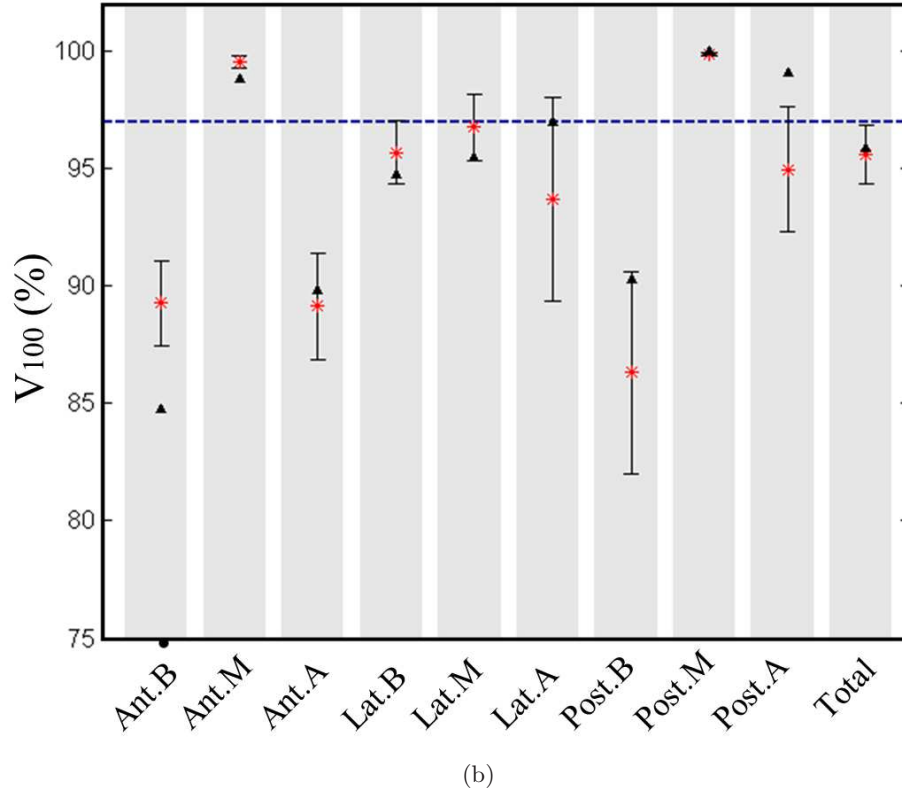
Figure 3.3: Continued. The means and 95% confidence intervals of the V_{100} when (b) a reference PTV is overlaid on the treatment plans created for the manual contours of 10 radiation oncologists, for a single patient (second of the five patients in (a). The typical goal V_{100} goal of 97% is shown as a dashed horizontal line. For comparison, the results of performing the test using the TES contours or their derived plans are displayed using the triangle symbols (Ant.: anterior, Lat.: lateral, Post.: posterior, B: base, M: mid-gland, A: apex).

(a)
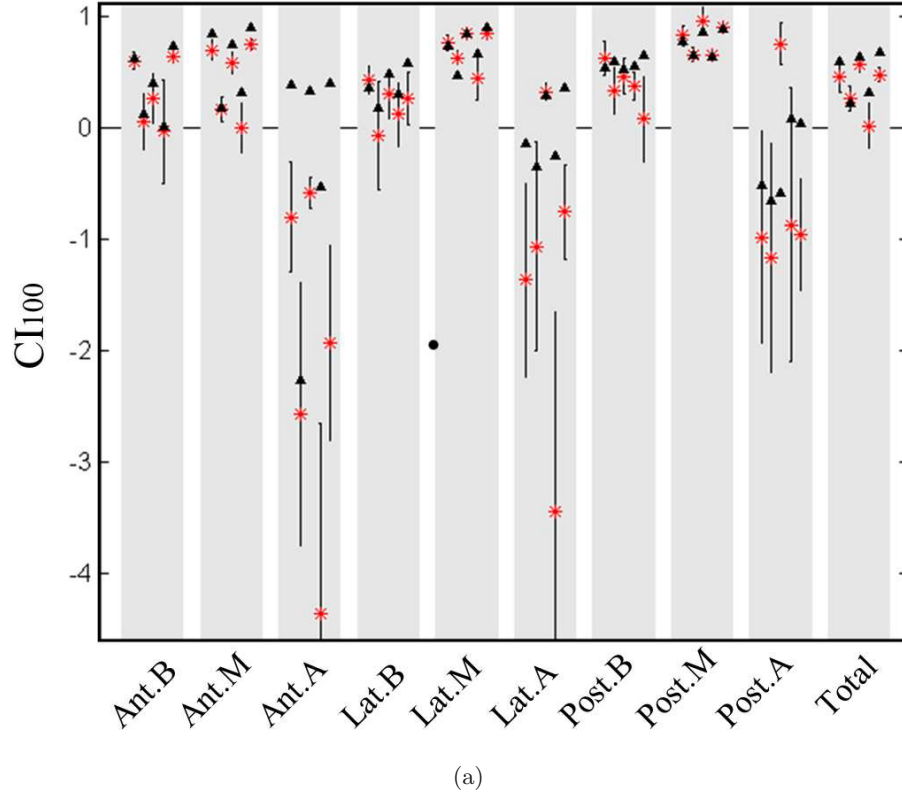
Figure 3.4: The means and 95% confidence intervals of the CI_{100} when (a) a reference plan, created for one set of contours, is overlaid on the manual contours of 10 other observers in 5 patients. For comparison, the results of performing the test using the TES contours or their derived plans are displayed using the triangle symbols (Ant.: anterior, Lat.: lateral, Post.: posterior, B: base, M: mid-gland, A: apex).

(b)
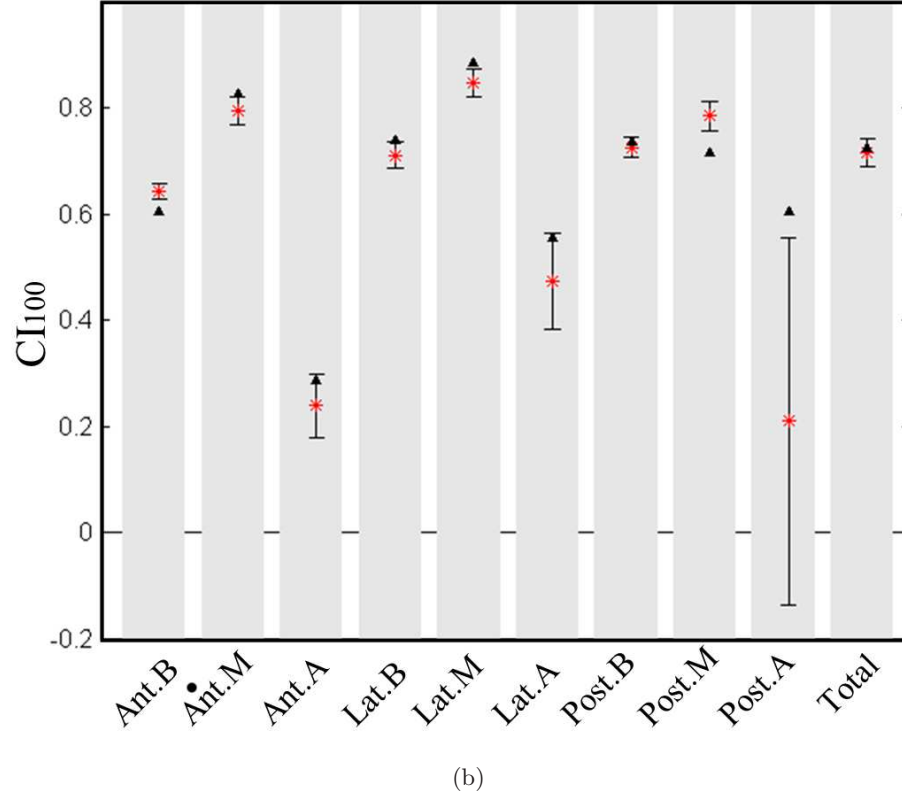
Figure 3.4: Continued. The means and 95% confidence intervals of the CI_{100} when (b) a reference PTV is overlaid on the treatment plans created for the manual contours of 10 radiation oncologists, for a single patient (second of the five patients in (a)). For comparison, the results of performing the test using the TES contours or their derived plans are displayed using the triangle symbols (Ant.: anterior, Lat.: lateral, Post.: posterior, B: base, M: mid-gland, A: apex).

3.6   Discussion

In this chapter we presented a dosimetric evaluation of our semi-automatic prostate segmentation algorithm (TES) for ultrasound images [60]. For 41 cases we measured the difference between the V_{100} and CI_{100} dose parameters of treatment plans created for the Raw TES PTV, used as the baseline, and treatment plans created for the Raw TES PTV's but overlaid on RO reviewed TES PTV's. The mean decrease in V_{100} and CI_{100} was less than 5% and 0.2 respectively, in all regions of the gland. The greatest degradation in quality occurred in the posterior base and apex, and anterior base and apex for the V_{100} and in the apex for the CI_{100}. However, this study has demonstrated, in a subset analysis of 5 cases with 10 blinded observers, that any differences in the distribution of dose when planning using TES contours are largely comparable with manual dosimetric variability between observers. Moreover, this variability only considered a single institution, and may be even greater between experts at different institutions due to diversity in training backgrounds and treatment strategies.

Our program regards the reproducibility of the alignment between the prostate, the probe and the patient's craniocaudal axes to be important, as the accurate registration of the pre-planned PTV with the prostate as visualized on the day of the implant to be a vital component in streamlining the procedure and reducing setup complications. This is facilitated by ensuring that the prostate is positioned so as to have mid-sagittal symmetry in the planning images. In addition, a smooth CTV topography is preferred to reduce the sensitivity of coverage to misalignment. The TES algorithm achieves these two goals with a minimum of operator assistance.

In our experience, the algorithm greatly reduces the time necessary to arrive at an acceptable CTV. The initialization of the algorithm and generation of a smooth and symmetric 3D surface, which is tedious to accomplish by hand, requires less than a minute by a radiation therapist. Once this (the Raw TES) CTV is complete, only 2-4 minutes of review and modification are required by the radiation oncologist to arrive at what we have described as the RO reviewed TES CTV, which is currently used for planning.

3.7   Conclusions

The results of this study suggest that many of the modifications to the Raw TES PTVs prior to planning are superfluous, in the sense that the impact of not performing the modifications will result in a planned dose distribution

not dissimilar in quality to that which would have been delivered if the patient had been treated by a colleague. On the basis of this finding, we conclude that the proposed TES algorithm is a suitable replacement for manual prostate segmentation in a pre-planned treatment methodology.

Chapter 4

Visualization of the Prostate Gland in Vibro-elastography Images

4.1 Introduction

In this chapter, vibro-elastography (VE), an ultrasound-based method that creates images of tissue viscoelasticity contrast, is evaluated as an imaging modality to visualize and segment the prostate. We report a clinical study to characterize the visibility of the prostate in VE images and the ability to detect the boundary of the gland. Measures for contrast, edge strength characterized by gradient and statistical intensity change at the edge, and the continuity of the edges are proposed and computed for VE and B-mode ultrasound images. Furthermore, using MRI as the gold standard, we compare the error in the computation of the volume of the gland from VE and B-mode images.

4.2 Materials and Methods

4.2.1 Data Acquisition

The B-mode ultrasound, VE, and MR images used in this study were acquired from patients going through the standard LDR prostate brachytherapy procedure at the Vancouver Cancer Center, BC Cancer Agency, or radical prostatectomy at the Vancouver General Hospital. Institutional ethics approval and informed patient consent were obtained prior to data collection.

The MR images were collected between one and two weeks prior to treatment. T2-weighted transverse MR images (slice spacing 4 mm, pixel size 0.27 mm ×0.27 mm) were collected at the UBC MRI research centre, Vancouver, with a Philips Medical Systems Achieva 3.0 Tesla MRI scanner. To

minimize the deformation of the gland and for patient comfort, imaging was carried out in a supine position and a cardiac coil was used.

The ultrasound data were collected intra-operatively, just prior to the actual brachytherapy or prostatectomy intervention, using the hardware described in Section 1.2.3 and the signal processing described in Section 4.2.1.

The vibrating TRUS probe, with a vibration range of 2-10 Hz (for the first 14 cases) and 2-5 Hz (for the last 6 cases) and vibration amplitude of approximately 1 mm, was swept from $-45°$ to $50°$, covering a fan of longitudinal planes passing through the transducer axis with a predefined angular separation of $2°$. At each angle, one B-mode image and frames of RF data were collected continuously for 2 seconds at an approximate frame rate of 40 fps. Imaging depth was set to 5 cm (or 6 cm for large prostates).

The entire procedure, including setting up the system, adjusting the TRUS probe in order to see the entire prostate in the ultrasound image (performed by a physician) and collecting the data requires approximately 20 minutes of the OR time.

VE system signal processing

The RF data were processed to obtain longitudinal VE transfer function images. Single DOF axial motion estimation was used in processing the RF data. Each RF data frame has 128 lines of RF data, each having 1296 samples (1424 for larger prostates). The collected RF data lines are split into blocks of 26 samples, or equivalently 1 mm, with 50% block overlap. The axial displacement $x_{jk}(t)$ of each block at axial location k and lateral location (line) j, and subsequently the axial strain, were computed from one RF data frame to the next by using a correlation-based method, as described in [122], resulting in axial displacement images of 128 lines by 100 blocks.

An image-based reference was used to compute the transfer function images. It was computed as the average strain, at half the tissue imaging depth, of all the 128 lines. This specific depth was chosen for to two reasons. First, the ultrasound imaging focal point is usually set at this depth, resulting in a more accurate motion estimation. Second, in our images, the half depth line is more likely to be enclosed entirely within the prostate, resulting in more uniform mechanical properties along the line.

The transfer functions $(H_{ref}^{jk}(j2\pi f)$ from this reference to each of the blocks in the strain images were computed using standard signal processing methods described in [90]. Vibro-elastography images used in this chapter

were generated by computing:

$$VE_{jk} = \frac{1}{f_2 - f_1} \int_{f_1}^{f_2} \left| H_{ref}^{jk}(j2\pi f) - H_{ref}^{j-1,k}(j2\pi f) \right| df \qquad (4.1)$$

where VE_{jk} is the pixel intensity value at axial location k and lateral location (line) j and $[f_1, f_2]$ describes the frequency range of interest, which in this work coincides with the range of the broad-band vibration applied to tissue.

If we assume that the Fourier transform of the reference described above is unity, then the contrast in the transfer function image from one spatial location (e.g. a reference) to another corresponds to the strain energy difference between these locations in the frequency range f_1 to f_2. By computing the 'difference' between transfer functions of consecutive blocks j and $j - 1$ on line k, with respect to reference ref (equation 4.1), changes in stiffness, including the prostate boundary, are highlighted. Throughout this chapter, and this chapter only, we will refer to these vibro-elastography 'difference' images as VE images.

From these sets of longitudinal images, 3D VE volumes were generated by interpolation (slice spacing in transverse direction, 0.43 mm, pixel size 0.5 mm ×0.5 mm). Similarly, the 3D B-mode volume (slice spacing in transverse direction 0.43 mm, pixel size 0.37 mm ×0.37 mm) was created from the collected longitudinal B-mode images. Various approaches to creating 3D volumes are described in detail in [27]. Our method of constructing a 3D volume by interpolating longitudinal images suffers from a decrease in image accuracy as the depth increases. However, the accuracy can be increased by using finer angle increments at the expense of scan time. Another alternative is to use the transverse (convex) array of the TRUS probe to generate a 3D sector view by changing the depth of the transducer with respect to the prostate. This approach also has the issue of decreasing accuracy at increased depth because the scan is acquired with a convex array. Furthermore, such a transverse plane sweep changes the TRUS position in the rectum causing the prostate to move as a function of probe depth, which is clearly undesirable. The analysis performed in this work uses the transverse plane of the constructed 3D volumes for evaluation. This choice was made because of the preference of the transverse view by the clinicians, and also for agreement with the transverse MRI images.

Figure 4.1 shows transverse VE, B-mode and MRI images of the prostate mid-gland of two patients. Half of the prostate boundary is delineated in one of the image sets. In Fig. 4.2 mid-sagittal VE (top row) and B-mode (bottom row) prostate images of three different patients can be seen. The prostate is the stiffer region as outlined in the VE image.

Table 4.1 describes the image types and number of cases used in this chapter. VE and B-mode images were obtained from 20 patients. Among these 20 cases, which consist of 178 co-registered VE and B-mode image pairs, 107 images are in the transverse plane and are used for edge evaluation. The remaining 71 images are in the longitudinal plane at multiples of 5° intervals with the mid-sagittal plane and are used along with the 107 transverse images, for CNR analysis. MRI data were also available for nine of the patients. These nine data sets are used for volume evaluation. The initial study started by recruiting patients for VE imaging at the time of the volume examination. However, we found that the patients were nervous and very uncomfortable with the additional time required to take the images with a different ultrasound machine. In some cases we were able to collect US data, but the same patients were not available for MRI, due to illness, ineligibility for MRI, and difficulty traveling for the additional medical exam. For the data acquired during the volume study, the acquisition time had to be minimized. Therefore the number of MRI scans that we have used in our study is limited. Nevertheless, this number is similar to that used in [98] that compares B-mode based prostate segmentation to MRI. Furthermore, in [98] and most of the studies cited therein, *post-operative* MRI is compared with TRUS. However, tissue will change as a result of treatment. We believe that comparison based on *pre-operative* images is necessary for general assessment of the gland's visibility and treatment planning.

Table 4.1: Description of the data used in this chapter

	Data set size	Image type	Image plane
Volume analysis	9 cases	MRI, VE, B-mode	transverse
CNR analysis	178 images (20 cases)	VE, B-mode	107 transverse, 71 longitudinal
Edge analysis	107 images (11 cases)	VE, B-mode	transverse

4.2.2   Evaluation Methods

In order to assess the visibility of the prostate in VE images, we utilize several evaluation measures. These include image-based measures, which consist of contrast-to-noise ratio, edge continuity and edge strength, and volume-based measures, which consist of volume error and volume difference.

68
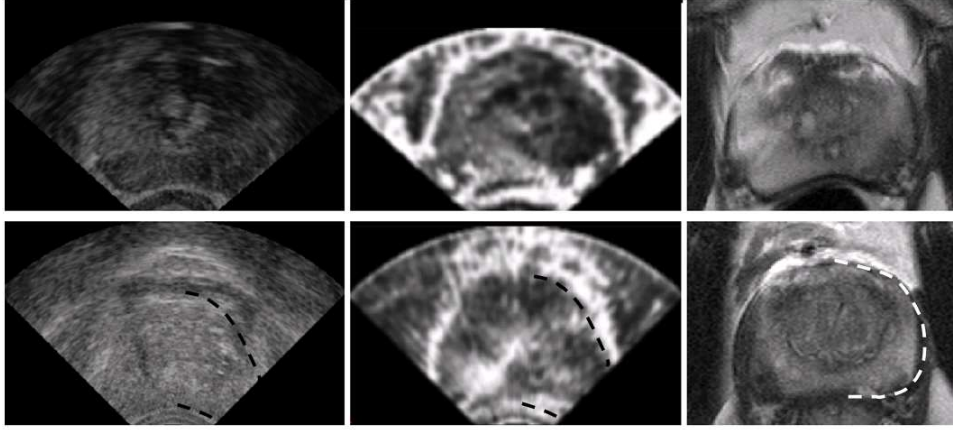
Figure 4.1: Transverse B-mode (left), VE (middle) and MRI (right) prostate images of two patients. The boundary of the prostate is partially segmented in the second set of images.
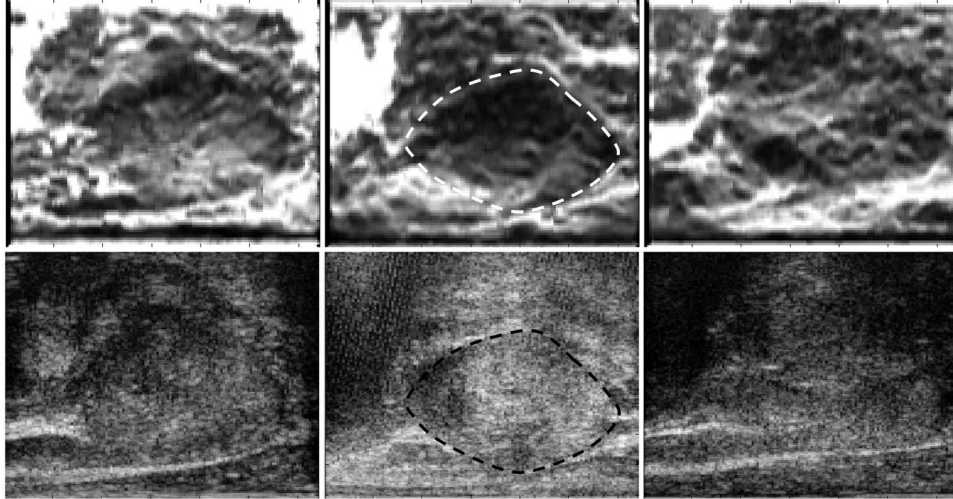
Figure 4.2: VE (top) and B-mode (bottom) sagittal images of the prostate of three different patients. The boundary of the prostate is outlined in one of the patients.

For more accurate region-based evaluation, the results of these measures will be reported for nine sectors of the gland, similar to those used in the previous
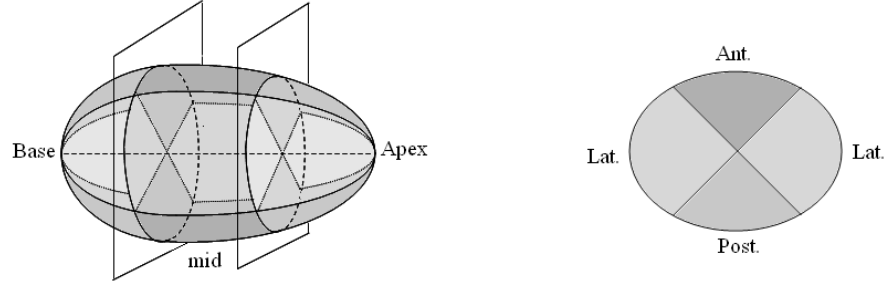
Figure 4.3: Division of the prostate into nine sectors

chapters and as shown in Fig. 4.3.

Image-based measures

Accurate delineation of the prostate is affected by how the prostate is visualized. A "good" image of the prostate is one in which the prostate has high contrast relative to the background and has well-defined edges. A good edge should be both "continuous" and "strong". In this analysis, VE images of the prostate are compared to B-mode ultrasound images using the measures of contrast, edge strength, and edge continuity as described below.

The Contrast-to-noise ratio

To compare the contrast of VE and B-mode images, the contrast-to-noise ratio (CNR) was calculated using the following equation [9]:

$$CNR = \frac{2(m_t - m_b)^2}{\sigma_t^2 + \sigma_b^2} \tag{4.2}$$

in which m and σ^2 are the mean and variance of pixel intensities of the target, t, and background, b, in a region of interest (ROI). The ROI of the target and background were manually selected in four regions of the prostate (lateral left, lateral right, anterior and posterior). The target is an area inside the prostate while the background is an area outside the prostate close to the target ROI (respectively yellow and blue boxes in Fig. 4.4). The physical size and position of the ROI in VE and B-mode images were similar.

(a) B-mode ultrasound   (b) VE
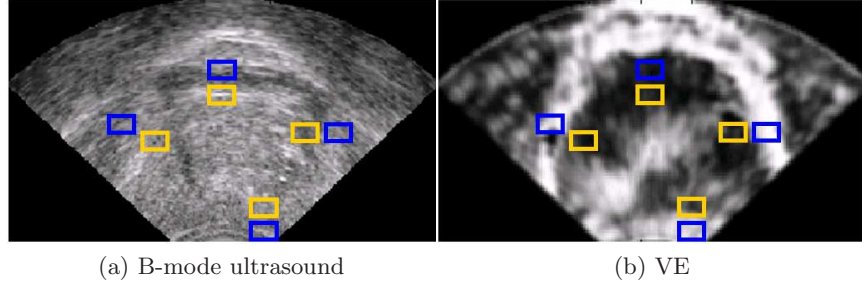
Figure 4.4: Selection of inside (yellow boxes) and outside (blue boxes) regions of the prostate for CNR computation in (a) B-mode and (b) VE images.

Additionally, to ensure similarity between the intensity range in both set of images, histogram stretching [0-255] was initially applied to the images.

The contrast between the prostate and its background is typically low in B-mode ultrasound images (see Fig. 4.1). However, due to the presence of a visible edge, delineation of the prostate is still possible. Therefore, CNR alone can not evaluate the visibility of an object in an image and edge evaluation is also required.

Edge strength

An edge can be defined as the boundary between two regions in an image that are different from each other with respect to some local property [50]. While conceptually clear, this definition is difficult to quantify. However, for the purpose of this study we need quantitative measures. Two different measures of edge strength are presented here. One is a conventional gradient-based edge filter and the second one is a test that identifies the statistical changes in image intensity. The edge strength measures are computed for radial edge profiles formed as follows: On each transverse image, we extended radii at $\theta_i = i \times 30°, i = 1, ..., 12$ in polar coordinates originating from a manually selected center point, C, inside the prostate. The intersections $r_{\theta_i}, i = 1, ..., 12$, of these radii with the prostate boundary were manually identified for each angle θ_i. For each edge point, a radial edge intensity profile $I_{\theta_i}(r)$ was extracted. The measures of edge strength were calculated for the window of $r \in [r_{\theta_i} - \Delta d, r_{\theta_i} + \Delta d]$, where Δd is half the length of the edge intensity profile (see Fig. 4.5).
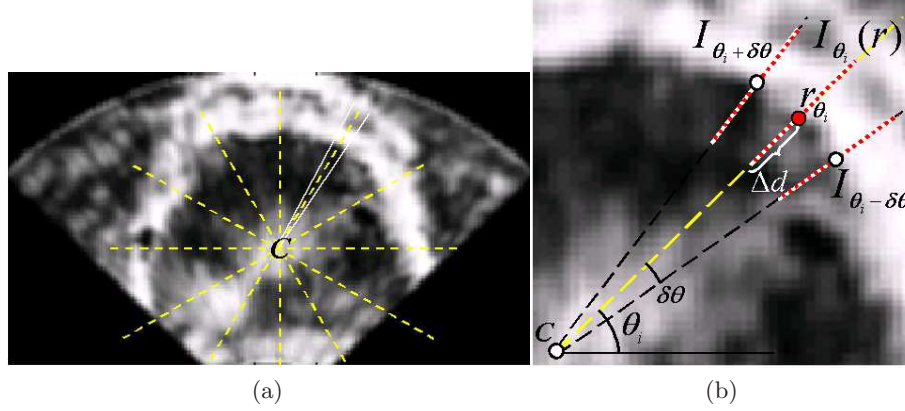
Figure 4.5: (a) The radii used for edge profile extraction in a VE image, originating from C and with angles $\theta_i = i \times 30°, i = 1, ..., 12$. For one of the radii, the two neighboring radii are also illustrated. (b) A close-up view of one of the rays used for extracting the edge profile $I_{\theta_i}(r)$. The measures of edge strength are calculated for the window of $r \in [r_{\theta_i} - \Delta d, r_{\theta_i} + \Delta d]$, where r_{θ_i} is a manually selected edge point along the ray. The neighboring edge profiles $I_{\theta_i \pm \delta\theta}$, are extracted similarly and used along with I_{θ_i} in the edge continuity measure.

Gradient-based measure of edge strength: The following gradient formulation, also used in [2], was used as the edge filter acting on a radial edge intensity $I(r)$, where we remove, for convenience, the θ_i index of I:

$$f_{edge}(r) = 1/3 \times [I(r+2\Delta r)+I(r+\Delta r)+I(r)-I(r-\Delta r)-I(r-2\Delta r)-I(r-3\Delta r)]^2 \tag{4.3}$$

where Δr is the physical size of the image pixel.

M, our measure of edge strength, is the sum of the filter outputs on windows of size n pixels (n an odd integer) normalized to the sum of edge filter values on the entire edge profile:

$$M(r) = \sum_{j=r-(n-1)\Delta r/2}^{j=r+(n-1)\Delta r/2} f_{edge}(j) \ / \ \sum_{j=r_{\theta_i}-\Delta d}^{j=r_{\theta_i}+\Delta d} f_{edge}(j) \tag{4.4}$$

The normalization is performed so that we can compare results for dif-

ferent areas. M is computed along $r \in [r_{\theta_i} - \Delta d, r_{\theta_i} + \Delta d]$, and is expected to have a strong peak at the edge. In our implementation, parameter values were set to $\Delta d = 0.5$ cm and $n = 5$ pixels.

DF statistical test: The performance of the gradient-based edge detector can be plagued by local minima in US images. Therefore, we present a new approach that models the difference of the radial edge intensity profile as an autoregressive process. The edge strength is characterized based on the degree of stationarity of this process. The stationarity of the edge profile is tested using the statistical test proposed by [22]. Each radial intensity profile, was considered as a time series $I_{\theta_i}(k) := I_{\theta_i}(k\Delta r)$, where the discretized radial distance k, such that $k\Delta r \in [r_{\theta_i} - \Delta d, r_{\theta_i} + \Delta d]$, replaces the usual time index.

The edge profiles, $I_{\theta_i}(k)$, can be modeled as a first order autoregressive AR(1) processes as follows:

$$I_{\theta_i}(k) = \rho I_{\theta_i}(k-1) + e_r \qquad (4.5)$$

where ρ is a real number and e_r is a sequence of independent normal variables with mean 0 and variance σ^2. In order to show that an AR(1) model is sufficient for modeling the edge profiles, we computed the partial autocorrelation function (PACF) of $I_{\theta_i}(k)$. The PACF of an AR(1) process has significant values only at lag=1. In 78% of the edge profiles extracted from both B-mode and VE images, at the significance level of 0.05, the PACF function only has significant values at lag=1.

$I_{\theta_i}(k)$ is stationary if $|\rho| < 1$. If a unit root exists ($|\rho| = 1$), then the variance of $I_{\theta_i}(k)$ is $r\sigma^2$, and therefore $I_{\theta_i}(k)$ is non-stationary. In many economics applications, the existence of the unit root, which is an indication of a "trend" or a "shock", is important for modeling and forecasting the future observations of a time series. Dickey et al. in [22] provided a statistical method to test an AR model for the null hypothesis of the existence of a unit root. If we re-write (4.5) as follows

$$\begin{aligned} \Delta I_{\theta_i}(k) &= I_{\theta_i}(k) - I_{\theta_i}(k-1) \\ &= (\rho - 1)I_{\theta_i}(k-1) + e_r \\ &= \gamma I_{\theta_i}(k-1) + e_r \end{aligned}$$

then the DF test is formulated as follows:

$$H_0 : \rho = 1 \leftrightarrow H_0 : \gamma = 0 \qquad (4.6)$$

$$H_1 : \rho < 1 \leftrightarrow H_0 : \gamma < 0 \qquad (4.7)$$

Note that the test is performed on the residuals and not the time series samples. Therefore, the standard t-distribution cannot be used. Dickey and Fuller provide a non-standard statistic τ, which depends on the number of observations, and provide tables of critical values for it. In other words, based on the calculated value of τ, they provide the significance level at which the null hypothesis above can be rejected. We used the implementation reported in [49] to perform the DF test.

The statistical properties of the intensity profile are altered at the edge. The existence of a strong edge in the time series is an obvious trend. A signal with a trend cannot be stationary, since its statistical moments depend on time, or in our model, on distance. In other words, if one traces the image in the radial direction, the intensity profile tends to become non-stationary upon passing through an edge. To evaluate the edge quality, we compute and report the percentage of edge profiles for which, according to the DF test, the stationarity hypothesis is strongly rejected ($p < 0.05$) for the edge profile. For an image with strong edges, one expects to see a high percentage of edge profiles for which the unit root exists and the stationarity hypothesis is strongly rejected.

Edge continuity

Detecting an edge point on a single edge profile can not guarantee the presence of an edge. Continuity of the presence of such a point within a neighborhood is an important factor for the visibility of the edge. We measure this continuity by measuring the similarity of the edge region within a neighborhood.

For a continuous edge, two neighboring edge profiles are expected to be similar, although slight differences may be present due to image noise or in the case of ultrasound, speckle. The normalized cross-correlations $R_{\theta_i, \theta_i \pm \delta\theta}(r)$ of the two neighboring edge intensity profiles $I_{\theta_i}(r)$ and $I_{\theta_i \pm \delta\theta}(r)$, $r \in [r_{\theta_i} - \Delta d, r_{\theta_i} + \Delta d]$ and the average $c(\theta_i)(r) = \frac{1}{2}[R_{\theta_i, \theta_i + \delta\theta} + R_{\theta_i, \theta_i - \delta\theta}]$ were calculated for each point, r_{θ_i}, at which the radius r_{θ_i} intersects the edge (see Fig. 4.5). The parameters we used for this implementation were $\theta_i = i \times 30^o$, $i = 1, ..., 12$, $\Delta d = 0.2$ cm, and $\delta\theta$ such that the arc length between the two adjacent edge profiles is 0.2 cm.

For a large similarity between adjacent edge profiles, c_{θ_i} should have a shape similar to the shape of a Gaussian function with large peak at the edge

point and a small standard deviation. Thus, we propose that the following edge continuity measure, $K(\theta_i)$, be calculated:

$$K_{\theta_i} = \frac{P^2(\theta_i)}{\sigma(\theta_i)} \tag{4.8}$$

in which $P(\theta_i)$ and $\sigma(\theta_i)$ are the peak and standard deviation of a Gaussian function fitted to c_{θ_i}.

Volume-based measures

The volume of the prostate is an important parameter in planning the dose distribution in LDR brachytherapy. A well defined 3D shape can also aid prostatectomy. To evaluate the shape and size of the prostate created from VE images, we compare them with the shape and size extracted from the commonly used B-mode ultrasound images. Since MR images of the prostate provide more anatomical details including visualizing the boundaries, the 3D surface extracted from MR images is used as the gold standard. Contouring in all three image types was performed manually and by three observers: one radiation oncologist and two trained by experts. The 'volume difference' and 'volume error' between surfaces created from MR and VE/B-mode images (i.e. MR vs. VE or MR vs. B-mode) provide shape and size similarity errors that can be used to compare to the gold standard provided by MRI.

The percent volume difference provides a measure of the difference in the size of the total gland for each of the nine sectors in VE/B-mode images compared to the gold standard MRI. It is defined as:

$$V_{diff}\% = 100 \times \frac{V_{VE/B-mode} - V_{MRI}}{V_{MRI}} \tag{4.9}$$

The percent volume error is the volume of the non-overlapping region between the surface of the prostate generated from VE/B-mode images and that of MR, divided by the sum of the two volumes. This is defined as:

$$V_{err}\% = 100 \times \frac{\left|(V_{VE/B-mode} + V_{MRI} - 2(V_{VE/B-mode} \bigcap MRI))\right|}{V_{VE/B-mode} + V_{MRI}} \tag{4.10}$$

In other words, it provides a measure of the difference in the shape of the gland compared to the gold standard. This definition is equivalent to $1 - DSC$, in which DSC is the Dice Similarity Coefficient [21].

The 3D shape of the prostate, in each modality, was extracted by manually segmenting the 2D images with the use of the Stradwin [109] software.
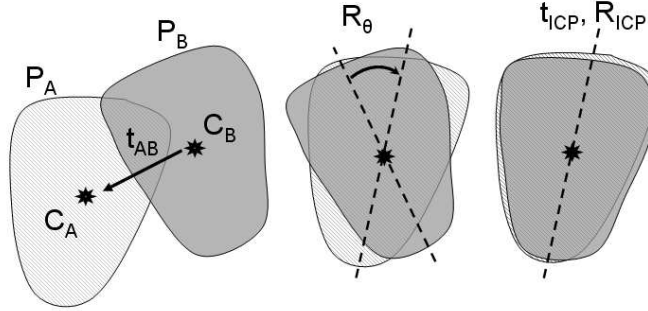
Figure 4.6: Registration of B-mode/VE prostate surfaces to MRI

This software was then used to transform the 2D contours into a 3D surface which could be opened in MATLAB$^{©}$.

To register the MRI and ultrasound images we opted for a rigid registration approach, as opposed to a deformable registration one. Indeed, these images were not acquired at the same time and the patients were in the dorsal lithotomy position during B-mode and VE acquisition and supine position during MR acquisition. Furthermore, the patients were anaesthetized and relaxed prior to the procedure, while they were awake and possibly tense during the MRI exam. A non-rigid (deformable) registration is not a suitable registration option since the goal is to understand the differences between the manually segmented surfaces. A deformable registration which maps one surface to the other will conceal these differences.

We assume that the main cause of mis-registration of the surfaces is the angle of the prostates' base-apex axis with the TRUS probe. This is mainly a result of the patients' orientation during imaging. We also assume that the size of the prostate does not change between data collection sessions and the prostate does not rotate around its base-apex axis by a large angle. For each surface, this axis was obtained by fitting a line to the centers of the prostate contours in each image slice.

With these assumptions, to register the prostate surfaces P_B (the VE or B-mode surface) to P_A (the MRI surface), a translation $\vec{t}_{AB}$ is first applied in order to match their geometric centers C_A and C_B. A rotation R_θ around the matched geometric center is then applied to rotate the base-apex axis of the translated prostate P_B to the main axis of P_A. θ is the angle between the base-apex axis of the two surfaces, obtained as described above. Finally a six degree-of-freedom Iterative Closest Point (ICP) method [8] translates

$(\vec{t}_{ICP})$ and rotates (R_{ICP}) the resulting surface to fine-tune the registration, resulting in $P_{B-registered}$ (Fig. 4.6), described as:

$$P_{B-registered} = R_{ICP}[R_\theta(P_B + \vec{t}_{AB}) + \vec{t}_{ICP}] \qquad (4.11)$$

The volume error and volume difference is calculated for the rigidly registered surfaces.

4.3   Results

4.3.1   Image Comparison

The Contrast

The CNR of VE and B-mode images, averaged over the three sections of the prostate, is shown in Table 4.2. Data from 178 images (from 20 patients) were used in this analysis. In all three regions the CNR of VE is significantly higher than that of B-mode ($p < 0.05$ for base, and $p < 0.001$ for the mid-gland and apex regions).

Table 4.2: CNR comparison of VE and B-mode images

	Base	Mid	Apex
CNR VE	10.25 ± 12.83	13.73 ± 5.85	20.51 ± 23.13
CNR B-mode	2.07 ± 1.06	1.43 ± 0.75	1.56 ± 1.16

Edge Strength: Gradient-based measure

The gradient-based measure of edge strength, M, was computed for edge profiles in the nine regions described in Section 4.2.2. The VE and B-mode images have different resolutions. This is due to the fact that the window size used for displacement estimation in VE images is larger than the B-mode pixel. Therefore, the choice of n (the window size), affects the value computed for M. We examined values of window sizes in the range of $n = 2$ to $n = 10$ and in all cases, the results of edge analysis were consistent. The reported results were acquired for $n = 5$. The result, extracted from 107 images of 11 patient datasets, is illustrated in Fig. 4.7 for the nine regions and in Fig. 4.8 for all regions combined. As illustrated in Fig. 4.7, the VE edges are notably stronger than B-mode edges with the exception of the anterior base and the posterior apex. The other observation of note is that the values of M show an evident peak in all areas of VE images, with the

exception of the anterior base. In the case of B-mode images, in some areas such as the lateral and anterior apex and the lateral mid-gland, the edges are very weak and are not represented by a dominant peak in the gradient values. In the posterior region of the prostate (the last row in Fig. 4.7) the B-mode edge strength appears to be similar or slightly higher than the VE edge strength.

It is evident from Fig. 4.8 that, overall, edges in VE images are stronger. At the edge point, the normalized M value is 2.2 times larger in VE images compared to B-mode images.
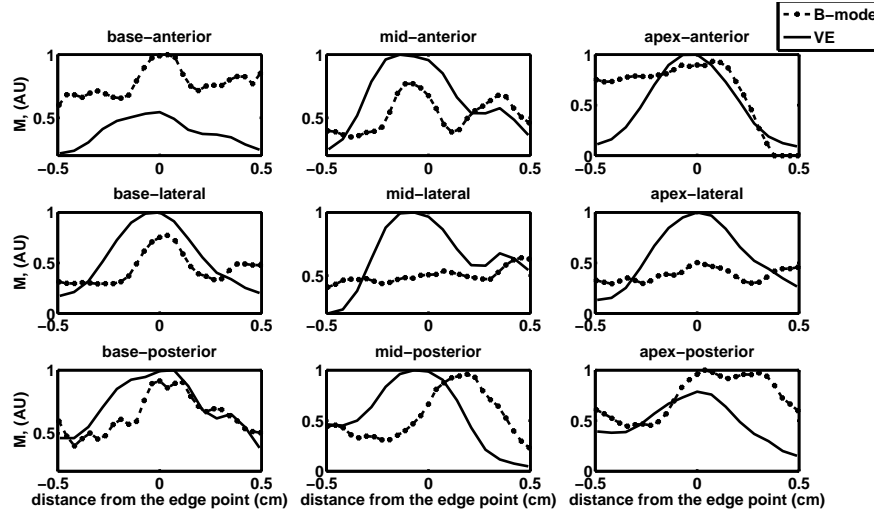
Figure 4.7: The values of the normalized gradient-based edge strength measure (M) in arbitrary units vs. the distance from the edge in cm, separated for the nine regions of the prostate gland.

Edge Strength: DF test of stationarity

Table 4.3 shows the percentage of edge profiles for which the DF test strongly shows a unit root ($p < 0.05$), and therefore, non-stationarity. 107 images from 11 patient datasets and 12 edge profiles within each image, were used in this analysis. This result is reported separately for the nine regions. The edges appear stronger in VE images in all areas, with the exception of the anterior base (matching the result from the gradient-based edge strength). In general, the edges in the base region are relatively weak in both modalities.
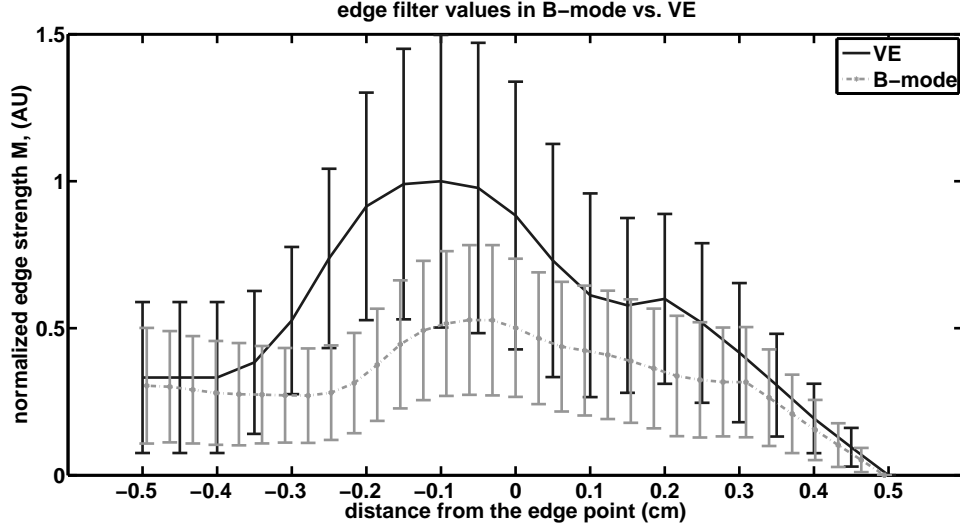
Figure 4.8: The values of the gradient-based edge strength measure (M) along the edge profiles for VE and B-mode images. Error bars represent the inter-patient standard deviation of the M values.

Table 4.3: The percentage of non-stationary prostate edge profiles in different areas of the B-mode and VE images. Standard deviations reported characterize inter-patient variations.

%	*VE*			*B-mode ultrasound*		
	Base	**Mid**	**Apex**	**Base**	**Mid**	**Apex**
Ant.	67.9±4.6	99.2±1.1	99.9±0.2	71.4±2.8	80.8±4.1	76.6±7.5
Lat.	79.5±3.1	98.8±0.9	98.1±1.7	66.1±3.5	81.3±2.5	88.9±5.1
Post.	78.6±3.5	99.2±1.9	99.8±0.2	67.9±3.2	80.8±4.1	84.1±8.1

Edge Continuity

Table 4.4 shows the edge continuity value, K, computed for VE and B-mode images in nine regions of the gland. 107 images from 11 patients were used in this analysis. The edge continuity of VE in all regions except for the anterior base and posterior apex is shown to be superior to that of B-mode images. This is also in agreement with the results of the gradient based measure of edge strength (Fig. 4.7).

Table 4.4: Average edge continuity measure, K, for the nine regions of the gland.

	$K(\theta_i)$ VE			$K(\theta_i)$ B-mode ultrasound		
	Base	**Mid**	**Apex**	**Base**	**Mid**	**Apex**
Ant.	0.64±0.37	0.87±0.33	0.84±0.37	0.71±0.52	0.69±0.41	0.50±0.32
Lat.	0.84±0.39	1.15±0.36	0.85±0.27	0.63±0.40	0.48±0.23	0.39±0.29
Post.	0.99±0.44	0.82±0.35	0.60±0.55	0.52±0.38	0.51±0.32	0.75±0.55

4.3.2 Volume Comparison

Figure 4.9 shows an example of VE (magenta) and B-mode (green) 3D surfaces compared to that of MRI (blue) for one of the patients. Figures 4.10 and 4.11 compare the percent volume error and volume difference between B-mode and MRI and between VE and MRI prostate surfaces manually created by one radiation oncologist (Figs. 4.10b, 4.11b) and two individuals trained by experts (Figs. 4.10a, 4.11a and Figs. 4.10c, 4.11c). Images from nine patient data sets were used. From Fig. 4.10 it can be seen that in most regions of the prostate, the mean volume error between VE and MRI is less than that between B-mode and MRI.

Over the total gland, a volume error of $8.8 \pm 2.5\%$ for VE vs. MRI and $10.3 \pm 4.6\%$ for B-mode vs. MRI, and a volume difference of $-4.6 \pm 11.1\%$ for VE vs. MRI and $-4.1 \pm 17.1\%$ for B-mode vs. MRI, averaged over nine patients and three observers, were obtained. However, a one sided analysis of variance does not show any statistically significant difference, which may also be due to the limited number of patients. In general because the prostate is not discernible at the base and apex, a larger error in shape (volume error) and size (volume difference) between VE or B-mode surface and the gold standard in these two regions compared to the mid-gland is expected. However, in general, and over the three observers, VE errors are smaller than those from B-mode.
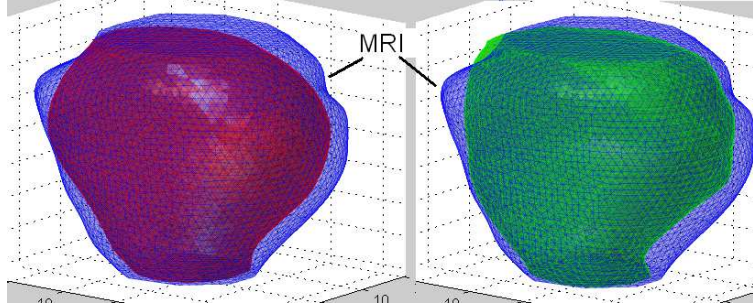
Figure 4.9: Comparison of VE (magenta) vs. MRI (blue) 3D surfaces, on the left, and B-mode (green) vs. MRI (blue) 3D surfaces, on the right, from one of the patients.

4.4   Discussion and Conclusions

In this chapter ultrasound vibro-elastography was evaluated as an imaging modality for the visualization of the prostate. We have quantitatively shown that VE is a promising imaging modality for delineation of the prostatic region and the use of such data along with B-mode ultrasound can improve the visualization of the gland.

VE transfer function (TF) images were qualitatively and quantitatively compared with the commonly used B-mode ultrasound. The evaluation measures used were both image based (CNR, edge continuity and edge strength) and volume based (volume error and volume difference). A nine sector analysis was used for more detailed characterization. The results on 178 images suggest that the VE images are significantly superior to B-mode images in terms of contrast of the gland. The gradient-based and the DF-based measures of edge strength and the edge continuity measure, on 107 images, all show that on average VE images provide stronger edges as well. It is important to emphasize that the statistically significant outcomes of our analysis of edge continuity and gradient-based edge strength are consistent: the edges in base-lateral, mid-lateral, mid-anterior, and lateral apex are significantly stronger and more continuous ($p < 0.05$ for the one-sided analysis of variance) in VE images compared to B-mode images. The K and M values, in addition to the visual inspection of the images, show that on average the anterior base and posterior apex of the prostate has weak edges on VE
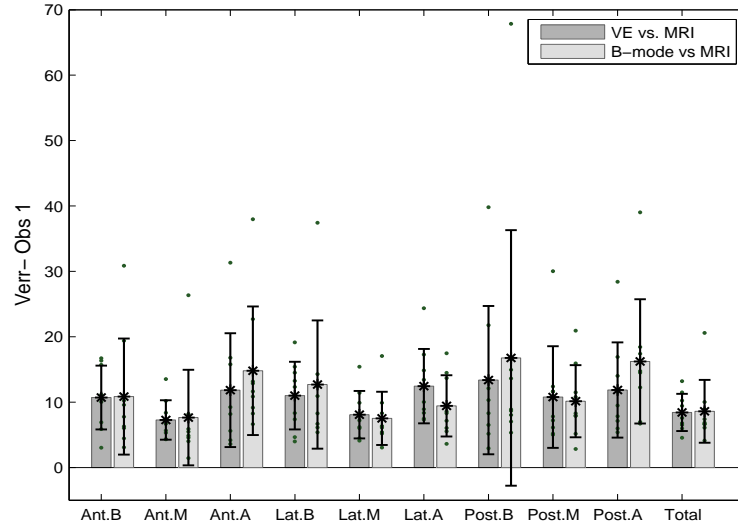
(a) Observer 1: trained by expert
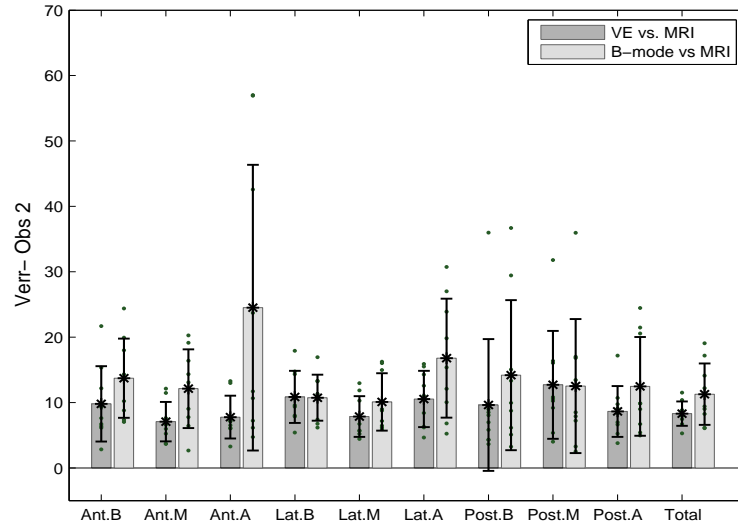
(b) Observer 2: Radiation Oncologist

Figure 4.10: A comparison between VE vs. MRI volume error and B-mode vs. MRI volume error, showing the mean and inter-patient standard deviation of $V_{err}\%$ for three observers. Sample data points are also shown as gray dots. Figure continues on the next page (Ant.: anterior, Lat.: lateral, Post.: posterior, B: base, M: mid-gland, A: apex).
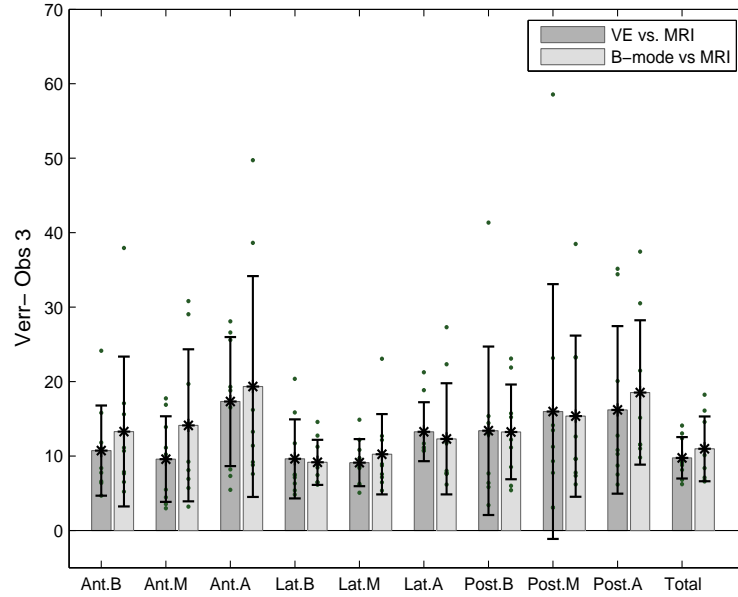
(c) Observer 3: trained by expert

Figure 4.10: continued

images.

The B-mode data used in this work was collected simultaneously with the RF data used for creating the VE images. In other words, B-mode and VE images were acquired under exactly similar conditions and are co-registered.

The comparison of volumes calculated from VE and B-mode prostate images show that VE volumes are closer to the MRI gold standard in most regions of the prostate, both in terms of shape and size. This confirms that the outlined region used in the image-based evaluation of VE, is indeed the prostate. In this comparison, prostate images from 9 patients were manually delineated by three observers (one expert and two trained by experts). The total gland volume error for VE vs. MRI was $8.4 \pm 2.9\%$, $8.3 \pm 1.8\%$, and $9.8 \pm 2.8\%$ for the three observers. For B-mode vs. MRI, these values were $8.6 \pm 4.8\%$, $11.3 \pm 4.7\%$, and $11.0 \pm 4.4\%$. The total gland volume difference for VE vs. MRI was $-5.3 \pm 11.7\%$, $-8.1 \pm 8.8\%$, and $-0.3 \pm 12.1\%$ for the three observers. For B-mode vs. MRI, these values were $-8.7 \pm 13.8\%$, $-1.4 \pm 20.2\%$, and $-2.1 \pm 17.7\%$.

It is also worth noting that V_{diff} (see Equation 4.9) measures the prostate volume ratios for B-mode/MRI and VE/MRI ($V_{diff} = V_{B-mode}/V_{MRI} - 1$).
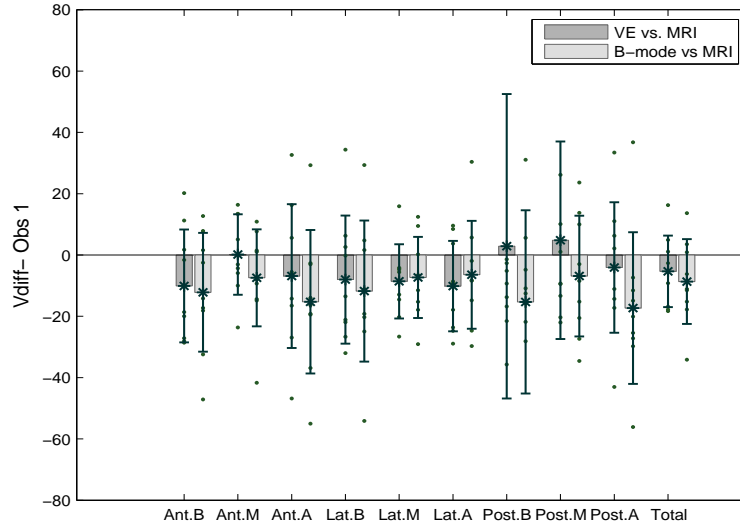
(a) Observer 1: trained by expert
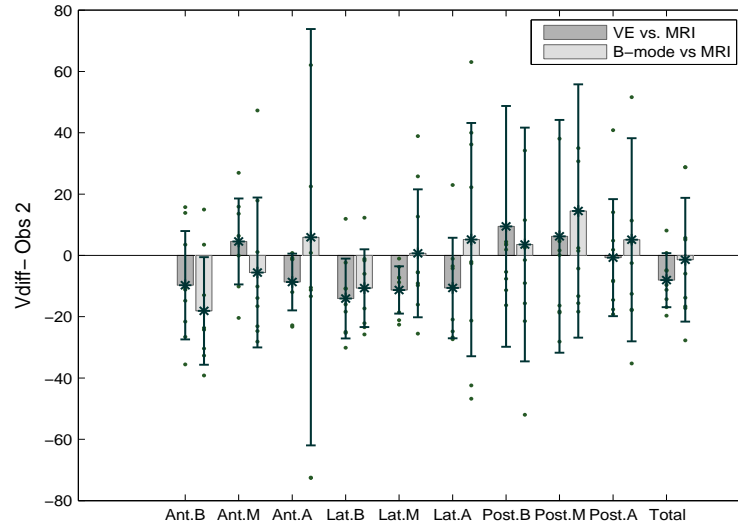
(b) Observer 2: Radiation Oncologist

Figure 4.11: A comparison between VE vs. MRI volume difference and B-mode vs. MRI volume difference, showing the mean and inter-patient standard deviation of $V_{diff}\%$ for three observers. Sample data points are also shown as gray dots. Figure continues on the next page (Ant.: anterior, Lat.: lateral, Post.: posterior, B: base, M: mid-gland, A: apex).
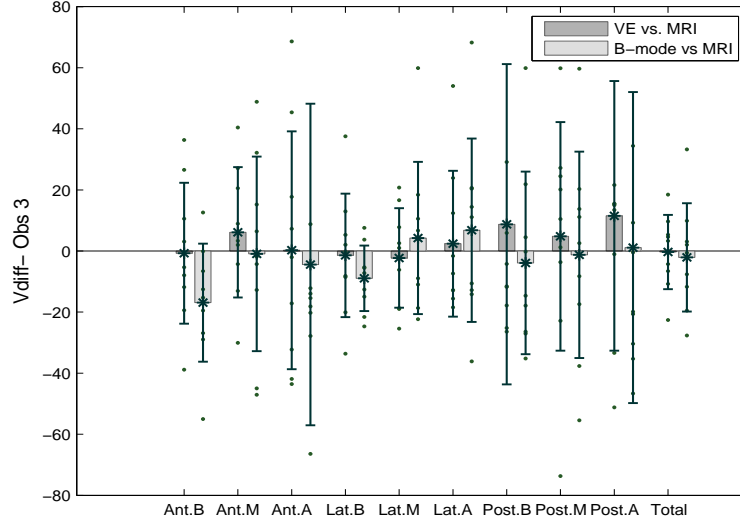
(c) Observer 3: trained by expert

Figure 4.11: continued

[98] report a MR/US prostate volume ratio of 1.11 ± 0.10 averaged over prostate surfaces from 10 patients outlined by 7 observers, repeated twice. Similar results from other work have been listed in a table therein. The MR/US prostate volume ratios for the 9 patients in our database are 1.12 ± 0.18, 1.05 ± 0.21, and 1.05 ± 0.19, for the three observers, which support previous work. For MR/VE, these values are 1.07 ± 0.13, 1.10 ± 0.10, and 1.02 ± 0.13. However, the volume ratio or V_{diff} only report differences in the *size* of the prostate, whereas two prostate surfaces can be greatly different in shape but have equal volumes. V_{err}, which we have included here, can provide useful characterization of the *shape* difference.

Currently, one dimensional axial motion estimation is used for creating the VE images. Any out of plane motion, including the lateral motions caused by the slippage between the protective sheath on the probe and the surface of the rectum during VE data collection, can affect the VE images. This can be improved upon by using 2D motion estimation techniques to account for lateral tissue motion. We have not used 2D motion tracking because most of the displacement estimates between consecutive frames of RF data are sub-sample. It has been shown that the gain based from 2D motion estimation in such cases is not significant enough to warrant its use [121] unless beam-steering is employed, such that the lateral motion is estimated from two axial measurements at different beam angles, e.g.

± 10 degrees. The increase in the number of axial measurements lowers the sampling rate and we opted not to do that in this set of experiments.

One should also keep in mind that the presence of the TRUS probe results in deformation of the posterior region of the gland in both VE and B-mode surfaces. For more accurate registration of these surfaces with those from MRI, this deformation could be accounted for. However, since the B-mode and VE images that we use are exactly registered to each other, this deformation will only result in a bias in the volume error and volume difference, especially in the posterior region, with MRI surfaces. The result of such a bias can be seen to be a generally larger mean and standard deviation in the volume error and volume difference of the posterior region in all three observers, compared to that of the lateral and anterior regions.

As a final note, the best validation of the prostate gland segmentation could be a comparison to pathology, the undisputed gold standard. Such a study requires access to the whole mount pathology, and viable solutions to the open problem of how to register the shrunk, misaligned pathology slices to pre-operative images.

Chapter 5

Automatic prostate segmentation using fused ultrasound B-mode and vibro-elastography images

5.1 Introduction

In this chapter an automatic method for segmenting the prostate is proposed. In this method, which is an extension of the semi-automatic method of Chapter 2, a combination of vibro-elastography and B-mode images is used to eliminate the need for manual initialization.

The elimination of user interaction in a prostate segmentation algorithm is desirable for various reasons. Manual interaction introduces user variability due to different user preferences and level of experience. An automatic algorithm can also be more time-efficient. Furthermore, it can be integrated into an automatic treatment method and be used intra-operatively.

In LDR prostate brachytherapy if treatment plans are created pre-operatively, the placement of the TRUS probe is initially adjusted intra-operatively to provide images of the prostate similar to the pre-operative volume study images. This is necessary due to the fact that the orientation (mainly due to patient positioning), shape and size of the prostate may change from the pre-operative volume study to the intra-operative imaging sessions. Occasionally, despite the adjustments, the treatment plan may need to be updated by the physician by adding or relocating seeds to adhere to the changed prostate boundary. The adjustment of the images and the plan is performed manually, which is time consuming and not free from uncertainty. If intra-operative planning, an established procedure used in some centers, is performed [1, 4, 71], the need for such adjustments is of less concern. Nevertheless, delineation of the prostate in a time-efficient way is needed for

intra-operative planning due to time limitations inside the operating room. Its application is not only limited to LDR brachytherapy, but can also be useful in high dose-rate brachytherapy or external beam radiation treatment and biopsy planning.

In Chapter 4 we showed that images produced by the vibro-elastography method developed in our group [90, 112] have superior prostate-background contrast compared to regular B-mode images, a result of the prostate tissue being generally stiffer than the surrounding tissue. However in some regions, and especially in the posterior region, the boundary of the prostate is better defined in B-mode images. In this chapter, we make use of the advantages of each image type and show that with the combination of elastography images and B-mode images we can achieve automatic 3D segmentation of the gland. The approach we use replaces the semi-automatic segmentation of the mid-gland slice in the method described in Chapter 2 with a fully automatic approach using an Active Shape Model (ASM).

To the best of our knowledge, this is the first report on fusion of vibro-elastography and B-mode images for prostate segmentation.

5.2   Methods and Materials

5.2.1   Data Collection and Processing

The B-mode and vibro-elastography images used in this chapter were acquired from patients going through the standard LDR prostate brachytherapy procedure at the Vancouver Cancer Center, British Columbia Cancer Agency or the radical prostatectomy procedure at the Vancouver General Hospital. Institutional ethics approval and informed patient consent were obtained prior to data collection.

Intra-operatively, prior to the procedure, RF data and B-mode images were simultaneously collected using the system described in [62]. RF data were collected using a Sonix RP ultrasound machine (Ultrasonix Medical Corp., Richmond, BC, Canada) at approximately 40 frames per second with the sagittal array of a vibrating transrectal ultrasound (TRUS) probe (dual-plane linear/microconvex broadband, 5-9MHz). The TRUS probe was vibrated with an amplitude of 0.5-2 mm peak-to-peak and frequency range of 2-10 Hz while being rotated along its longitudinal axis from $-45°$ to $45°$ to collect a series of RF data planes spanning a 3D volume in the shape of a cylinder with a sector base as shown in Fig. 5.1. The angle step size was $2°$, and data were collected for 2 seconds per angle, resulting in approximately 80 frames at each angular location. The total duration for collecting the 3D
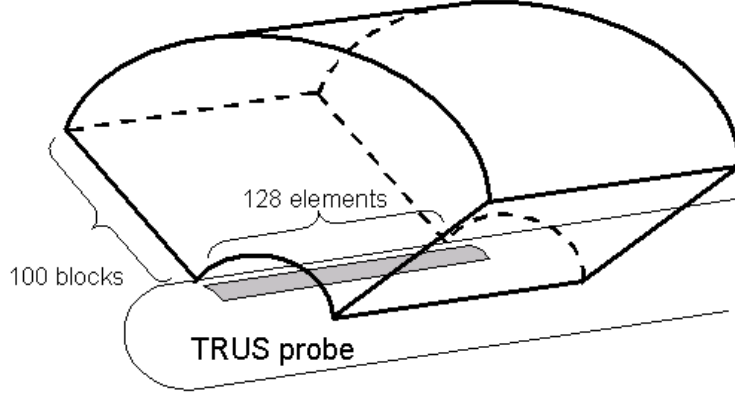
Figure 5.1: Illustration showing the span of the RF data planes with respect to the TRUS probe.

data was approximately 1.5 minutes.

Each RF data frame has 128 axial lines corresponding to the 128 probe elements. These frames were processed using the method described in [90], resulting in a time series of strain images of size 128 lines by 100 blocks for each angle for the period of vibration. For every angle one vibro-elastography image was then obtained as follows:

$$VE_{jk} = \frac{1}{f_2 - f_1} \int_{f_1}^{f_2} \left| H_{ref}^{jk}(j2\pi f) \right| df \qquad (5.1)$$

where $H_{ref}^{jk}(j2\pi f)$ is the transfer function (TF) of the strain computed using standard signal processing methods from a reference point in the image (computed as the spatially averaged strain, at half the tissue imaging depth) to a block at axial location k and lateral location j in the strain image. $[f_1, f_2]$ is the range of the broad-band vibration applied to the tissue. Further details are provided in [90] and [61].

By interpolation, 3D matrices with voxel intensities representing tissue stiffness were achieved from the longitudinal TF images.

The B-mode and vibro-elastography 3D volumes are matrices of size $162{\times}275{\times}128$ pixels and $100{\times}169{\times}128$ pixels respectively. The 128 transverse images, corresponding to the 128 transducer elements, are spaced at 0.43 mm and the pixel sizes in B-mode and vibro-elastography are 0.31 mm and 0.5 mm, respectively. For 3D segmentation, to increase the speed of the algorithm, we only used 32 out of the 128 transverse images, each spaced at

1.73 mm.

Throughout the algorithm we make use of B-mode and vibro-elastography phase symmetry images. The code and description of the calculation of phase symmetry images are available in [54]). The B-mode and VE phase symmetry images are used in the initialization of the algorithm while the weighted sum of pixel intensities in B-mode phase symmetry and B-mode image is used in the deformation of the posterior part of the prostate contour. We observed that this combination highlights the boundary of the prostate particularly well in the posterior region. Figure 5.2 shows a B-mode image, its phase symmetry image and the weighted sum of the two. A vibro-elastography image and its phase symmetry image are also shown.

5.2.2   2D Segmentation Algorithm

We use an Active Shape Model (ASM) approach [18] for 2D segmentation of the prostate. To guide the deformation of the model at each iteration we use a combination of information from vibro-elastography and B-mode ultrasound images. The algorithm steps are summarized in Table 5.1 and each step is further discussed below.

The ASM algorithm consists of an offline phase in which the training set is created and the statistics of the model are extracted and an online segmentation phase where the model is evolved based on image characteristics.

In the offline training phase:
1. Each contour in the training set is created from 30 manually selected specific points on the prostate boundary, $X = [x_1 \cdots x_{30}; y_1 \cdots y_{30}]^T$. The training set consists of $N = 25$ contours from the mid-gland images of 7 patients. The images were chosen to cover a broad range of prostate shapes and none of the training set images were used in the segmentation step. Figure 5.3 shows the location of the 30 points on the prostate boundary. 10 of these points are selected from specific anatomical locations (mid-posterior, mid-anterior, lateral left and right, lowest points and lower left (right) points of the lobes and two points between the mid-anterior and lateral points). The remaining 20 points are selected to be at equal distances between every adjacent pair of the ten points specified above.

2. The manually segmented contours are then aligned and scaled using a least-squares-based iterative scaling, rotation and translation method and the mean shape, X_{mean}, is the mean position of all corresponding boundary points. The distribution of the prostate contours and the 10 main points in the training set, after alignment, are shown in Fig. 5.3.
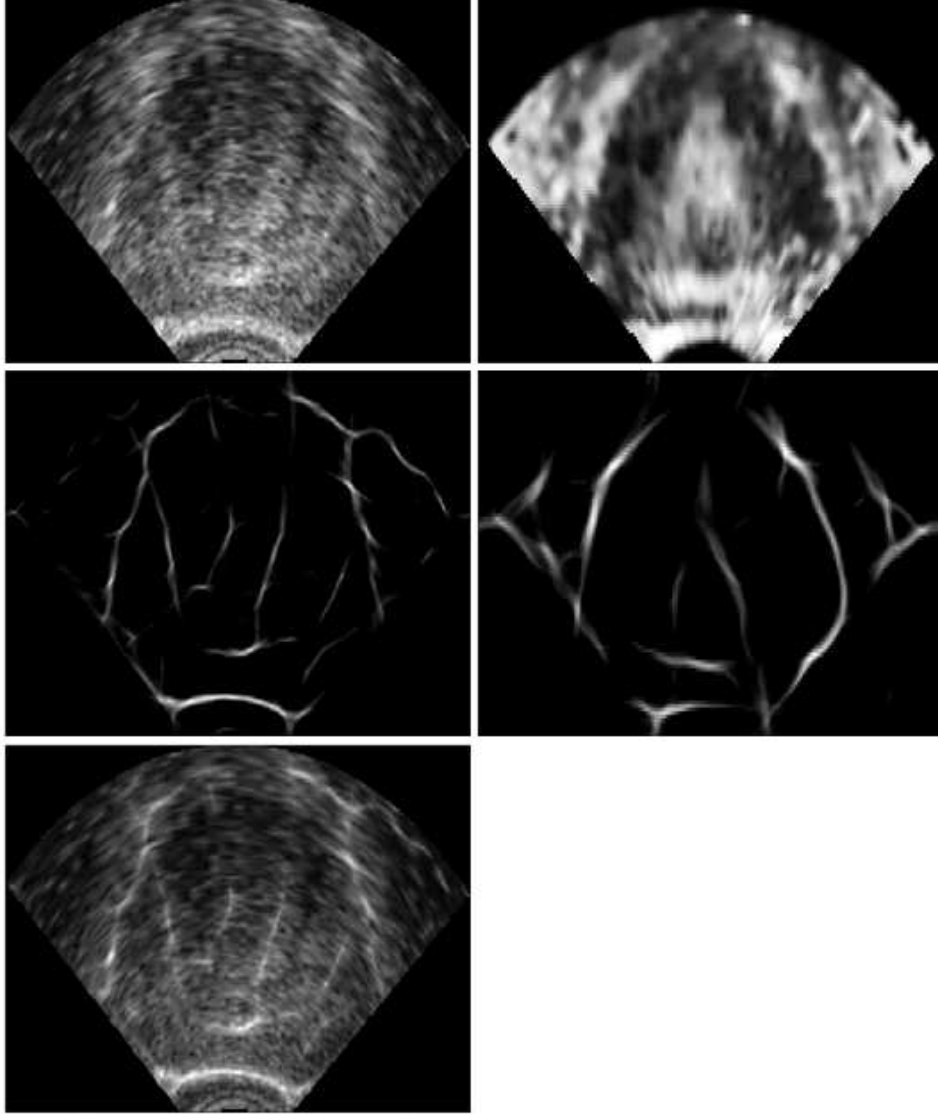
Figure 5.2: A B-mode image (top left) and the corresponding vibro-elastography image (top right) of the prostate mid-gland along with the phase symmetry of the B-mode (middle left) and vibro-elastography (middle right). The sum of the B-mode image and its phase symmetry is shown in the lower left.

Table 5.1: The main steps in the ASM algorithm.

Offline training
1. Create a training set of manually marked gland boundary points.
2. Align and scale the prostate contours and compute the mean shape X_{mean}
3. Extract the shape statistics from the training set by computing the modes of variation of the prostate shape.

Online segmentation of the target image
4. Obtain the initial shape X_{init} using X_{mean} and target image information. Set $X_{current} = X_{mean}$
5. Find the desired shape deformation:

$dX_{desired} = X_{desired} - X_{current}$

5.(i) For non-posterior boundary points use a combination of gray level similarity and edge continuity measures from B-mode and vibro-elastography images.

5.(ii) For posterior boundary points use intensity gradient information from B-mode and its phase symmetry image.
6. Calculate the required adjustments in the pose parameters which best map $X_{current}$ to $X_{desired}$.
For that, find the rotation, scale and translation adjustments $d\theta$, ds, and dt which minimize the weighted sum
$E = (X_{current} - T_{ds,d\theta,dt}(X_{desired}))^T(X_{current} - T_{ds,d\theta,dt}(X_{desired}))$
using a least-squares approach, where if, for example applied to a point $[x, y]^T$

$$T_{s,\theta,t}([x,y]^T) = \begin{bmatrix} t_x \\ t_y \end{bmatrix} + \begin{bmatrix} s\ cos(\theta) & -s\ sin(\theta) \\ s\ sin(\theta) & s\ cos(\theta) \end{bmatrix} \begin{bmatrix} x \\ y \end{bmatrix}$$

The residual shape adjustments, dx, can then be made by deforming the shape model.
7. Calculate $db = P^T dx$ to obtain the required shape adjustments in the model parameter space.
8. Update the shape parameters: $b \rightarrow b + db$ and the pose parameters: $s \rightarrow s(1 + ds)$, $\theta \rightarrow \theta + d\theta$, $t \rightarrow t + dt$.
9. Update the shape: $X_{next} = T_{s,\theta,t}(X_{init}) + Pb$, which consists of applying the updated pose parameters $(T_{\theta,s,t}(.))$ and the shape parameters (b) to the initial shape.
10. Set $X_{current} = X_{next}$ and repeat steps 5-10 until convergence.
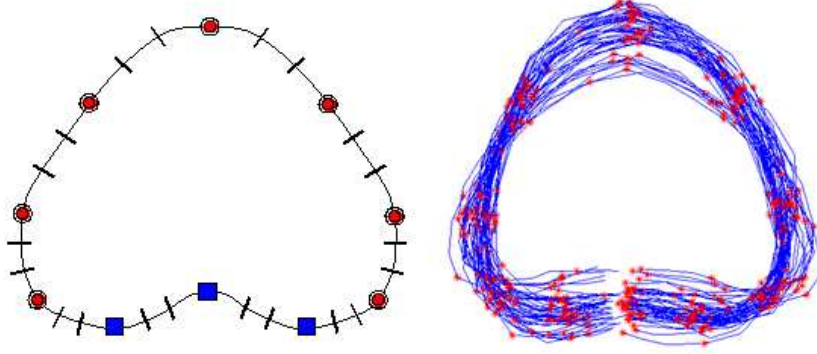
Figure 5.3: The 30 boundary points used to model the prostate boundary (left) highlighting the 10 main points as red circles and blue squares and the aligned and scaled, manually segmented prostate boundaries in the training set, showing only the 10 main points (right). We define the posterior points as the main points shown as blue squares and the four points in between them.

3. To capture the statistics of the training set, the covariance matrix is computed according to (5.2):

$$S = \frac{1}{N} \sum_{i=1}^{N} dx_i dx_i^T \tag{5.2}$$

where dx_i, in the training phase, is the vector between each point on the manual contour and the corresponding point on X_{mean}. The modes of variation of the shape are described by the eigenvalues λ_i, and eigenvectors p_i, of S, from which the n_λ largest eigenvalues are selected as the most significant modes of variation. We selected n_λ such that for $i = 1, \cdots, n_\lambda$, $\lambda_i / \sum_{i=1}^{N} \lambda_i > 5\%$. For our training set $n_\lambda = 3$ satisfied this condition.

A shape instance consistent with the training set can thus be created from an initial contour X_{init} using (5.3):

$$X = X_{init} + Pb \tag{5.3}$$

where $P = (p_1 \cdots p_{n_\lambda})$ is the matrix of the first n_λ eigenvectors of S and $b = (b_1 \cdots b_{n_\lambda})^T$ is a vector of weights, also called the shape parameters.

For each point i of each image j of the training set, a normalized edge derivative profile g_{ij}, normal to the boundary, centered at the model point, and of length $2n_p$ is extracted (Fig. 5.4). This is the derivative of the edge

93

intensity profile divided by the sum of its absolute values over the length of the profile. From g_{ij}, the mean edge derivative profile $\bar{g}_i$, (the average over all corresponding boundary points in the training set) is computed and the difference between the derivative profiles and $\bar{g}_i$ is used to compute the co-variance matrix S_{g_i} [17]. These provide a statistical description of the gray level appearance for every location of the prostate boundary, as illustrated in Fig. 5.4, and are used in computing the edge gray level similarity measure, d_g, described further in the chapter in step 5.(i).
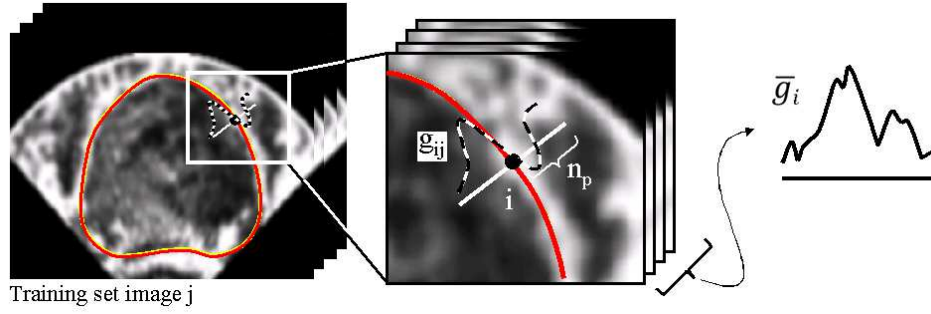
Figure 5.4: Illustration of how for point i on the model edge of training image j, a normalized edge derivative profile, g_{ij} normal to the boundary and centered at the model point and of length $2n_p$ is extracted. The average of g_{ij} over the number of training images results in $\bar{g}_i$.

In the online segmentation phase:
The goal is to find the pose (scaling, translation and rotation) and shape parameters (deformations within the model constraints) which cause the model to deform into the structure of interest. That is, starting from the initial shape X_{init}, at each iteration, we aim to deform the current shape points $X_{current}$ into a desired shape $X_{desired}$ obtained from image features.

4. To obtain the initial shape X_{init}, the mean prostate shape, X_{mean}, from the training set is scaled and translated to provide a closer shape match to the shape instance of the prostate to be segmented and hence, faster algorithm convergence. This is done by first fitting ellipses to the B-mode and vibro-elastography phase symmetry images (Fig. 5.2, second row). Using the size and center of the smaller of the two fitted ellipses we scale and center X_{mean} to obtain X_{init}. We use the scale and center position of the the smaller ellipse since it was seen that, in some cases, the presence of anatomical features in the prostate anterior may falsely be detected as

part of the prostate during the ellipse fitting process resulting in a larger than expected ellipse.

5. The computation of $dX_{desired}$, the desired change in the boundary point locations to obtain a shape which best fits the prostate, is described next.

6. Having computed $dX_{desired}$, first the pose parameters are adjusted using a least-squares approach described in [18] to find the rotation, scaling and translation which best maps $X_{current}$ to $X_{desired}$, the difference being the residual dx.

7. Then, the shape parameters, db, are adjusted given dx and using (5.4) to obtain the shape closest to $X_{desired}$ which adheres to the model:

$$db = P^T dx \tag{5.4}$$

Based on our image characteristics, we compute $dX_{desired}$ for the posterior and non-posterior points using two different methods. A combination of candidate motions from both B-mode and vibro-elastography images is used for the non-posterior points. In the posterior portion of the prostate boundary vibro-elastography images show low contrast but this boundary is more visible in B-mode images. We attribute this low contrast mainly to the slippage between the probe, its protective sheath and the soft surface of the rectum and the use of one dimensional axial tissue strain estimation. Therefore in this region we use a gradient-based motion on the weighted sum of the pixel intensities in B-mode and their phase symmetry images. Posterior points include the three posterior main points and the four points in between them as shown in Fig. 5.3 and the non-posterior points include the remaining 23 boundary points.

5.(i) To calculate the movement, $dX_{desired}$, for the non-posterior model points, we use a combination of four candidate motions, as defined in (5.5), based on the Mahalanobis distance [18] and an edge continuity measure that we derived in [62]. These two measures are computed from both B-mode and vibro-elastography images for each non-posterior boundary point i:

$$dX_{desired} = d_f u_n \tag{5.5}$$
$$d_f = \alpha_{gUS} d_{gUS} + \alpha_{gE} d_{gE} + \alpha_{KUS} d_{KUS} + \alpha_{KE} d_{KE}$$

where u_n is the unit vector normal to the boundary at the boundary point, d_{gUS} and d_{gE} are the motions of the boundary point along u_n derived from the gray level similarity in B-mode and vibro-elastography images,

and d_{KUS} and d_{KE} are the motions of the boundary point along u_n computed from the edge continuity measures in B-mode and vibro-elastography images, respectively (index i dropped for clarity). A set of weights $\alpha = [\alpha_{gUS} \ \alpha_{gE} \ \alpha_{KUS} \ \alpha_{KE}]= [0.15 \ 0.25 \ 0.25 \ 0.35]$ that works well was found by trial and error.

Details of how each of the two measures d_g and d_K are computed are as follows:

The edge gray level similarity measure, d_g

During the shape fitting phase, at each iteration and for every point, sample edge derivative profiles $h_i(d)$ $(d = -l \cdots l)$ of length $2n_p$ are extracted at the current boundary point similar to the model edge derivative profile $(\bar{g}_i)$ which was computed in the offline phase. The square of the Mahalanobis distance between these profiles from the model profile, provides a measure of edge gray level similarity, and is maximized:

$$d_g = \arg \max_d = \left\{ (h_i(d) - \bar{g}_i)^T S_{g_i}^{-1} (h_i(d) - \bar{g}_i) \right\} \qquad (5.6)$$

for each point, to compute d_{gUS} (or d_{gE}) (see Fig. 5.5).

The physical values of l and n_p are set to 8 and 2.5 mm, respectively. These particular values were used to ensure both adequate coverage of the edges and reasonable profile lengths in pixels (l=16 pixels and n_p=5 pixels for a vibro-elastography image).

The edge continuity measure, d_K

We observed that the gray level edge similarity measure alone gives many false positives due to ultrasound speckle or sharp edge-like structures since only 1D information (normal to the edge) is being analyzed. Therefore, in our approach, we incorporate the edge continuity measure proposed in [62], where an edge must not only be detected along the direction of the edge profile, but must also be present in its neighborhood.

To compute the edge continuity at a distance d $(d = -l \cdots l)$ from each boundary point i and along u_n, the edge intensity profile $e_i(d)$ of length $2n_p$ is extracted. The two neighboring edge intensity profiles, $e_{1i}(d)$ and $e_{2i}(d)$, are of the same length $2n_p$, parallel to and spaced at 1.5 mm on either sides of $e_i(d)$, as shown in Fig. 5.5. We compute the average normalized cross-correlations, $C_{1i}(d)$ and $C_{2i}(d)$, between the edge intensity profile $e_i(d)$ and its two neighboring edge intensity profiles.
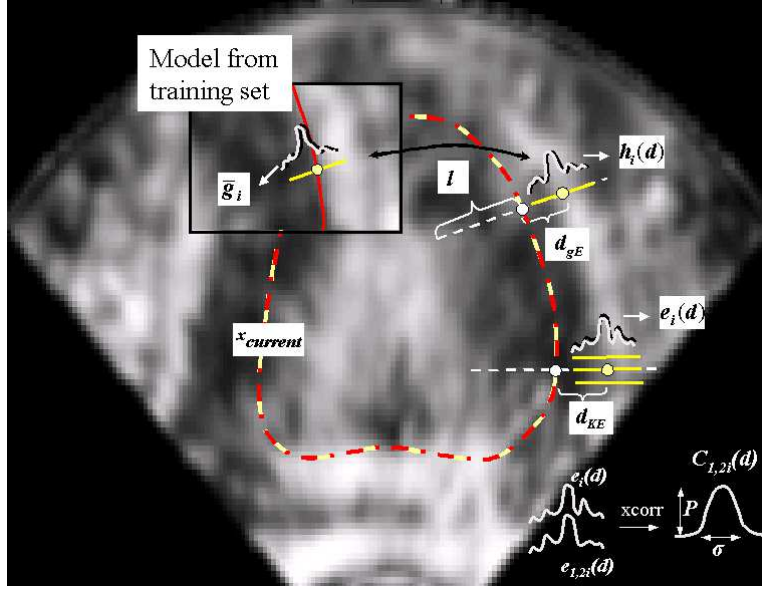
Figure 5.5: Illustration showing the computation of gray level similarity and edge continuity for two boundary points. In the upper point the edge derivative profile $h_i(d)$ is compared with that of the model, $\bar{g}_i$ (shown in the rectangle) along a line normal to the edge and of length $2l$. d_{gE} is the distance from the current boundary point where the maximum similarity is obtained. In the lower point the gray level intensity profile, $e_i(d)$, is compared to its two neighbors, $e_{1i}(d)$ and $e_{2i}(d)$, to obtain correlation functions, $C_{1i}(d)$ and $C_{2i}(d)$. d_{KE} is the distance from the current boundary point to where a maximum correlation exists between the center profile and its neighbors. A similar procedure is applied to B-mode images to obtain d_{gUS} and d_{KUS}.

For a continuous edge (i.e. large similarity between $e_i(d)$ and its neighboring profiles), $C_{1i}(d)$ and $C_{2i}(d)$ should each have a shape similar to a Gaussian function with a large peak and a small standard deviation. We define the edge continuity measure as follows:

$$K_i(d) = \left[P_{C_{1i}}^2 + P_{C_{2i}}^2 \right] /2\sigma_i(d) \tag{5.7}$$

in which $P_{C_{1i}}$ and $P_{C_{2i}}$ characterize the peak and σ_i is the standard deviation of a Gaussian function fitted to $C_{1i}(d)$ and $C_{2i}(d)$. For each point, we compute:

$$d_K = \arg\max_d \{K(d)\} \tag{5.8}$$

Figure 5.5 displays how the grey level similarity and edge continuity measures are computed for two boundary points on the prostate contour, respectively. This is shown for a vibro-elastography image but is computed in the same manner for B-mode images. Due to the difference in image resolution we ensured that corresponding parameters, such as profile length, match in terms of physical dimensions in both B-mode and vibro-elastography images.

5.(ii) To compute $dX_{desired}$ for the posterior points we use the weighted sum of the pixel intensities of the B-mode and their phase symmetry images: $I_{Bmode}(m, n) + 0.5 I_{phase}(m, n)$ where $I_{Bmode}(m, n)$ and $I_{phase}(m, n)$ are the pixel intensities of the B-mode image and its phase symmetry at location (m, n) (assuming an identical intensity range in both images). (see Fig. 5.2). In the posterior region the edge intensity profile, $e_i(d)$, is extracted as discussed before and the desired location of the boundary point in the next iteration is set to the point along the profile normal to the edge where the gradient of $e_i(d)$ is maximized:

$$dX_{desired} = d_{gradUS} u_n$$
$$d_{gradUS} = \arg\max_d \{grad(e_i(d))\} \tag{5.9}$$

where $grad(e_i)$ is the gradient of the edge intensity profile.

The algorithm stops when either the maximum number of allowed iterations has been reached (set to 50) or when at least 96% (29 out of 30) of the boundary points for 2D evaluation, and 94% (28 out of 30) of the boundary points for 3D evaluation, have a small $dX_{desired}$ (we chose a value less than 2.5 mm).

5.2.3   3D Segmentation

For 3D segmentation we use a modification of the method in [60], summarized here for completeness (see Fig. 5.6):
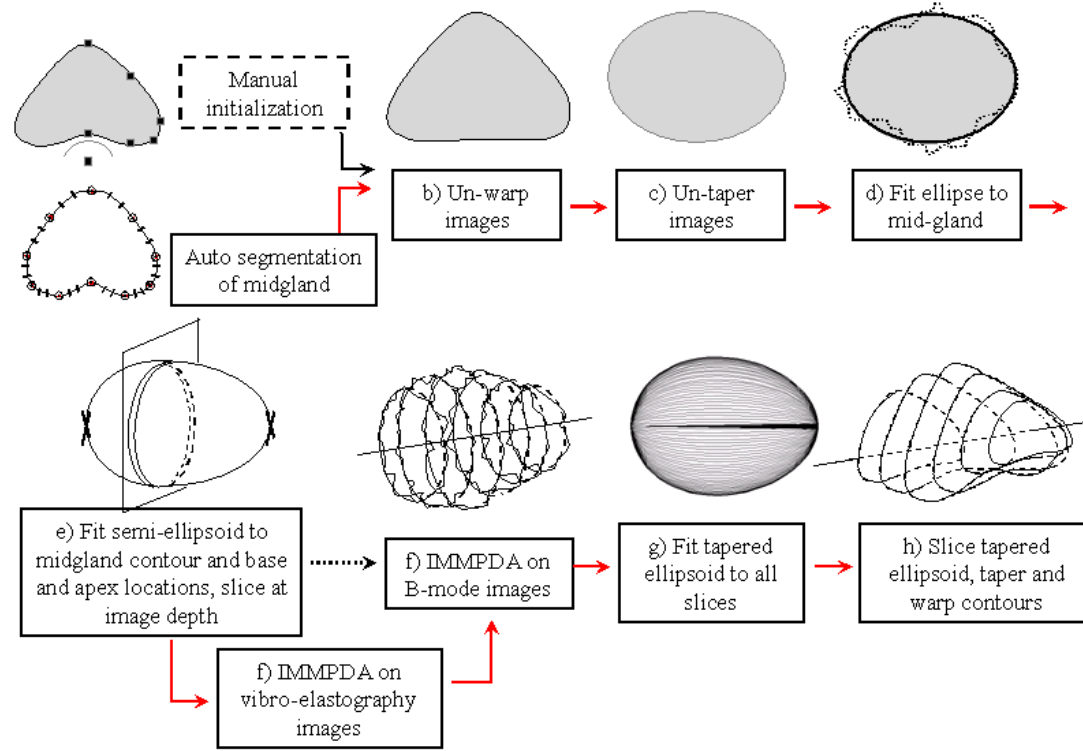
Figure 5.6: The main steps of the 3D semi-automatic prostate segmentation algorithm proposed in [60] including the applied modifications. Manual initialization is replaced by automatic segmentation of the mid-gland and vibro-elastography images are included in the segmentation process.

The prostate is modeled as a warped and tapered ellipsoid. Warping is present in the prostate posterior due to the pressure from the TRUS probe. Tapering is present in the anatomical shape of the gland, both in the transverse plane and from the base to the apex. The aim of the 3D segmentation method is to fit such a shape to a set of 8-12 transverse B-mode images that are collected from the base to the prostate apex prior to the procedure.

The user manually selects six specific boundary points on the mid-gland image. With the aid of these points, the transverse images are first un-warped and then untapered, resulting in prostate cross section images that are elliptical in shape, and the mid-gland image is segmented. The prostate is now modeled as an egg shape with an elliptical cross section. The remaining images are segmented by first fitting two semi-ellipsoids to the mid-gland contour and the base and apex positions (usually defined during imaging), slicing them at image depths and using the obtained ellipses as guides for the IMMPDA edge detector [2]. Finally an ellipsoid tapered along the base-apex axis is fitted to all the detected edges, sliced at image depths and tapered and warped (using the inverse of the same untapering and unwarping values initially used), to match the original images. Figure 5.6 displays the main steps of the 3D original algorithm along with the modifications applied in this chapter.

In order to automate the aforementioned algorithm, we replace the manual initialization step with the 2D automatic segmentation method proposed in Section 5.2.2 by replacing the six manually selected boundary points with the 30 boundary points of the ASM-based contour. Additionally, we use vibro-elastography images, in addition to B-mode, for the ASM-based 2D segmentation and when segmenting the remaining slices. That is, after slicing the two fitted semi-ellipsoids to the mid-gland contour and the base and apex locations, the resulting contours are used to guide the IMMPDA edge detector in the vibro-elastography images first and then, the results are used to guide the IMMPDA in the B-mode images.

5.2.4 Evaluation

We compare the automatic segmentation results with manually segmented contours from ultrasound B-mode images. Manual segmentations are performed by two trained individuals (author and colleague) , blind to the automatic results. A total of 61 co-registered pairs of B-mode and vibro-elastography images from 17 cases are used for 2D evaluation. Since the ultimate goal is to automate the 3D semi-automatic segmentation method

which requires initial segmentation of the mid-gland slice, the 2D evaluation is performed on mid-gland images. Out of the 17 cases available, the whole prostate is reasonably visible in 11 cases. We use these 11 cases for evaluation of the 3D algorithm. In the remaining 6 cases the prostate was not completely visible either due to artifacts (e.g. air bubbles covering the TRUS probe or insufficient contact of the probe with the prostate) or the prostate being out of the field of view (when the prostate is large or the TRUS probe is not appropriately positioned causing the full length of the gland not being covered).

For 2D evaluation, the measures used for comparing the manually created contour C_{man}, with that of the automatic contours C_{auto}, are as follows:

- *MaxD*: The maximum absolute radial distance between C_{man} and C_{auto}, in a slice.
- *MAD* : The average absolute radial distance between contours C_{man} and C_{auto}, in a slice.
- *DSC* : The Dice Similarity Coefficient [21] equal to
$2\left(A_{man}\bigcap A_{auto}\right)/\left(A_{man} + A_{auto}\right)$, where A denotes area of contours.

For 3D evaluation, the measures used for comparing the manually created volume V_{man}, with that of the automatic V_{auto}, are as follows:

- V_{err}: Volume error. The absolute volume of the non overlapping region between two volumes defined as:

$$V_{err} = \left|(V_{auto} + V_{man} - 2(V_{auto\cap man}))\right|/(V_{auto} + V_{man}) \qquad (5.10)$$

- V_{diff}: Volume difference. The difference between the volumes of two delineated prostates defined as:

$$V_{diff} = (V_{auto} - V_{man})/V_{man} \qquad (5.11)$$

These measures are computed for both the whole gland and the base, mid-gland, and apex regions (being respectively, 0.3, 0.4, 0.3 of the length of the gland).

Table 5.2: 2D segmentation results

	MaxD (mm)	MAD (mm)	DSC
Obs. 1	6.49±3.48	2.55±1.41	0.87±0.07
Obs. 2	7.04±3.36	2.66±1.50	0.87±0.08

5.3 Results

5.3.1 2D Segmentation

Table 5.2 shows the results of comparing the 2D automatic and manual contours (two observers) for the 61 mid-gland images. The duration of the algorithm was 13.3±12.3 s and the percentage of cases which converged within the maximum number of iterations (50) was 80.3%.

To show the benefits of using vibro-elastography images, we repeated the evaluation using the weights $\alpha =$[0.5 0 0.5 0], that is using gray level similarity and edge continuity in only B-mode images for the non-posterior points (motion of the posterior points stays the same). In only 19.7% of the images the algorithm converged when vibro-elastography images were not used. The MaxD and MAD values of the 19.7% converged cases were 11.41±4.22 mm and 4.59±1.43 mm for observer 1 and 12.09±4.07 mm and 4.93±1.56 mm for observer 2.

5.3.2 3D Segmentation

Table 5.3a and 5.3b display the volume error and volume difference between the 3D automatic segmentation surfaces and manually created surfaces by both observers for three regions of the prostate (base, mid-gland and apex) and the whole gland. In Table5.3c, the volume of the manually and automatically created surfaces, and the volume of the non-overlapping region between them are shown in cm^3. The Stradwin software [109] was used to create the surfaces from the segmented images. The 3D segmentation duration, that is the time required for segmenting the 3D volume of the prostate starting from the 2D segmented mid-gland image, was 31.7±3.3 s.

Figure 5.7 shows an example of 2D automatic segmentation of the mid-gland. The initial contour X_{init} which is the average of the training set

Table 5.3: 3D segmentation results

(a) $V_{err}(\%)$

	Base	Mid-gland	Apex	Whole gland
Obs. 1	12.7±3.0	7.7±2.7	13.1±3.8	10.2±2.2
Obs. 2	13.4±3.2	10.2±3.6	21.4±9.6	13.5±4.1

(b) $V_{diff}(\%)$

	Base	Mid-gland	Apex	Whole gland
Obs. 1	-2.5±12.1	-9.2±5.5	-7.4±16.8	-7.2±9.1
Obs. 2	-7.3±11.1	-14.0±9.5	-14.0±30.2	-13.3±12.6

(c) Volume error, and volume of automatic and manual segmentation (cm^3)

Obs. 1	Base	Mid-gland	Apex	Whole gland
Vol. err.	3.0±1.0	3.2±1.6	2.3±1.3	8.5±3.7
Vol. man.	12.4±5.2	22.3±8.3	8.7±3.8	43.5±17.1
Obs. 2	**Base**	**Mid-gland**	**Apex**	**Whole gland**
Vol. err.	3.3±1.3	4.3±1.7	3.2±2.2	11.4±4.4
Vol. man.	13.1±5.5	23.3±7.8	9.9±4.3	46.3±16.9
Vol. auto	11.8±4.2	20.1±7.1	7.8±2.7	39.7±13.9

contours scaled and centered according to the phase symmetry B-mode and vibro-elastography images, is shown in dashed yellow. The final contour (in this case, converged after 6 iterations) is shown in solid red. As shown in the figure, the deformed contour can extend past the field of view. This was

allowed so that the missing lateral regions of the prostate have less affect on segmentation. For this purpose, in every iteration, any boundary point that falls outside the field of view (i.e. falls in the black region) is given a lower weight when obtaining the deformed shape. The 3D segmentation result initialized by the 2D automatic contour is also shown (blue triangulated surface) and compared to the manually segmented surface (red).
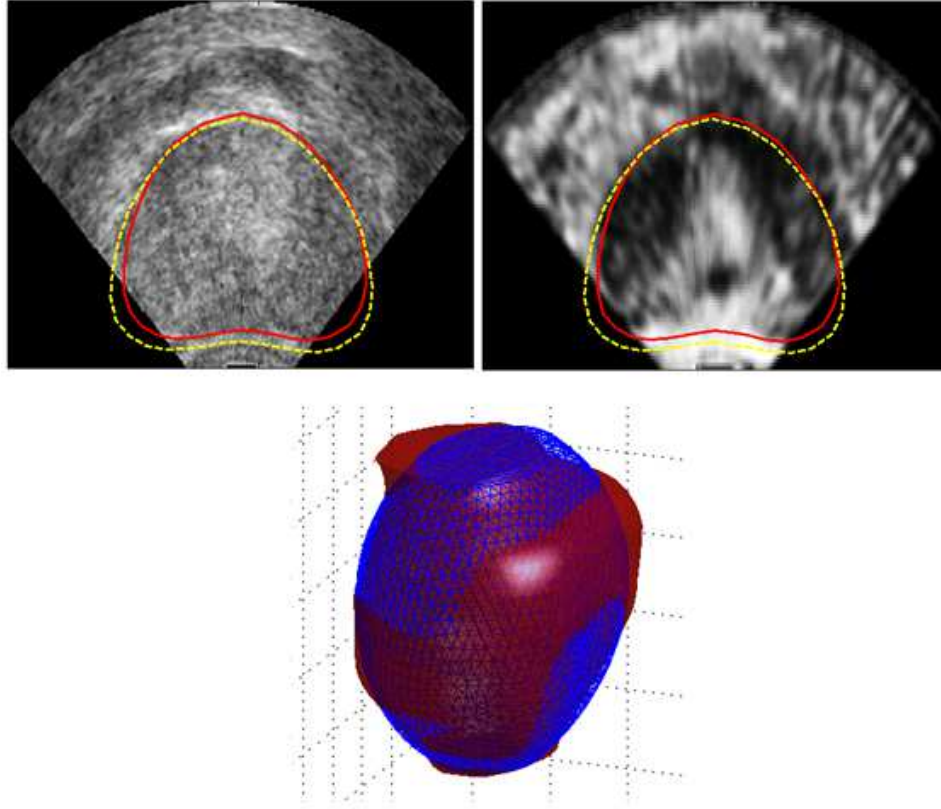
Figure 5.7: 2D segmentation results shown on corresponding B-mode (left) and vibro-elastography (right) mid-gland images. The initial contour X_{init} is shown in dashed yellow and the final contour in solid red. The final 3D segmented surface (triangulated blue) is also compared to the manually created surface (red) in the lower image.

5.4 Discussion and Conclusions

In this chapter we presented an automatic 2D and 3D prostate segmentation algorithm using a combination of both ultrasound B-mode and vibro-elastography images. The high contrast of vibro-elastography images aids segmentation especially since B-mode image quality is known to be relatively poor. To the best of our knowledge the combination of these two image types and an edge continuity measure have not been used for prostate segmentation before.

As we will discuss below, with similar volumetric errors and algorithm duration, the advantage of the current method over the previously proposed semi-automatic method is the elimination of manual initialization by replacing the manually selected initial boundary points with an automatically created mid-gland contour. The use of vibro-elastography images in the segmentation procedure was found to be necessary as we showed in our 2D evaluation that when only B-mode images are used, algorithm convergence is achieved in only 19.7% of the cases.

Various methods are proposed for computing $dX_{desired}$. In [39] the goal is to minimize a cost function based on a grayscale profile normal to the edge. This method, although simple and fast, can fail where the boundary is absent or weaker than a non-boundary grayscale transition. In [17] the square of the Mahalanobis distance is used, a measure of gray level similarity at the boundary point and normal to the boundary.

Even though due to the difference in data sets and evaluation methods, direct comparison is not reasonable, we will provide some reported results from the literature. The 2D ASM-based method proposed in [39] results in an average mean absolute distance and maximum distance of 1.09 ± 0.49 mm and 7.27 ± 2.32 mm between manual (the average of three repeated manual delineations of three trained graduate students) and automatic contours (on 36 patient data sets) in their ASM-based method. In the 3D extension of this method, after each 2D image is segmented, manual editing (required in 26.3% of the 2D images in each case) is allowed, after which the modified points are clamped and the model is re-deformed. In the 3D semi-automatic method proposed by [113] a 83.5% percent volume overlap (the intersection divided by the union of two volumes) between automatic and manual (average of three observers' manual contours) is reported on a data set of 30 patients. In [125] a mean overlap volume error of 4.16% compared to manual segmentation on six patients is reported. [117] report a mean absolute distance of 1.65 ± 0.47 mm and a Dice similarity coefficient value of 0.91 ± 0.03 between automatic and manually delineated TRUS video sequences of 19

patients.

Our results are comparable to the above, however, with standard quality TRUS images we expect lower errors. In the 3D semi-automatic method that we proposed in [60] higher quality B-mode images, equivalent to those displayed on the ultrasound machines' screen, were used. But the B-mode images that we were able to save along with the RF data to use in this work were of lower quality. That is because we did not have access to the additional post processing steps applied to the images before they are displayed on the machine. Nevertheless, the setup used for collecting RF data is a modified standard brachytherapy setup and the vibro-elastography images are created from RF data collected simultaneously with the B-mode images. Therefore, the B-mode and vibro-elastography images are co-registered.

For a better comparison and to see the effect of image quality on the results, we ran the semi-automatic segmentation algorithm on the same 11 cases used in this chapter and performed volumetric comparison with the manual surfaces created by the two observers. The whole gland volume error between the semi-automatic surfaces and manual surfaces created by the two observers were 10.0±2.6% and 13.6±3.9% and the volume differences were -2.2±12.3% and -8.4±16.9% for 11 cases. By comparing these results with those reported in [60] we observe higher error values (volume error of 6.63±0.90% and volume difference of 2.43±6.08%). We attribute this to the lower quality of the images compared to those used for evaluation in our previous work. On the other hand, these errors are similar to those that we report in Table 5.3 (volume errors of 10.2±2.2% and 13.5±4.1% for the two observers and volume differences of -7.2±9.1% and -13.3±12.6%). In [63] our dosimetric analysis on treatment plans created based on semi-automatic volumes showed that the semi-automatic method is a suitable replacement for manual segmentation in prostate brachytherapy. The similar errors suggest that if higher quality B-mode images, similar to those used in [60], were used, the surfaces created from the automatic method can also be a suitable replacement.

One of the sources of error, seen in our 2D results, is the presence of the anterior peri-prostatic venous plexus. This can be a fairly large structure, which collapses when circulation is stopped. It is seen in our in-vivo data as a dark region in VE and B-mode images and therefore, can sometimes be mistaken as the prostate anterior during automatic segmentation, especially when it has a contrast similar to that of the gland. For example, see Fig. 5.8. In this case, the anatomical structure, forming a shadow anterior to the prostate, has resulted in a large segmentation error. This structure is also present in Fig. 5.7, but has not caused a problem. A second source of error is

the limited field of view (-45 to 45° in the transverse view, due to mechanical limitations in our setup) which in some cases does not entirely cover the lateral portions of the prostate, especially in the mid-region (for example, see Fig. 5.7). As a result, in some cases we observe automatic volumes smaller than that from manual segmentation. Even though this missing information has been accounted for to some extent in the 2D segmentation method (seen as the contours extending beyond the field of view, as Fig. 5.7 shows) it results in smaller 3D surfaces. By increasing the field of view, this source of error can be eliminated.
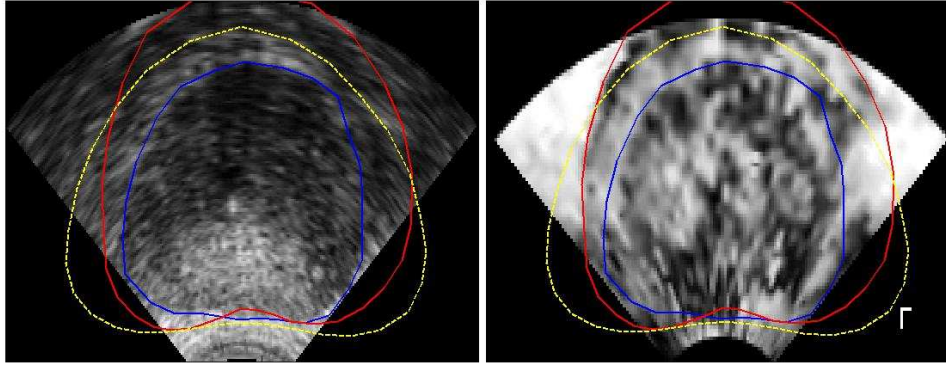
Figure 5.8: The anterior peri-prostatic venous plexus is observed as a dark region in B-mode and VE images. When its contrast is similar to the prostate-to-background contrast, it can be mistaken as the gland itself. In this figure the dashed yellow is the initial automatic contour, and solid red is the final. Solid blue indicates the manually segmented prostate boundary.

In [60] a 3D segmentation time of 17.17±2.71 s for segmenting the 11 cases using the semi-automatic method was reported (code written in MATLAB$^{©}$) and an additional 32±14 s manual initialization time was required resulting in a total of approximately 49 s. A similar value is seen in the current automatic method; once the training set is created (which can be done offline), approximately 45 s is required for segmenting the gland. However, optimization of the algorithm can further reduce the segmentation time.

Based on the above results and discussions we conclude that the proposed 3D automatic segmentation algorithm has the potential to be a suitable replacement for manual segmentation of the prostate. We showed the importance of adding vibro-elastography images to the conventional B-mode, for improving prostate segmentation. The proposed algorithm can be optimized

to be used as a real-time segmentation method for intra-operative prostate interventions.   -

Chapter 6

Visibility of Cancer in Vibro-elastography Images of the Prostate

6.1 Introduction

In this chapter, we provide initial results from an ongoing study on cancer visibility in vibro-elastography images. Vibro-elastography and pathology data are collected, processed and registered, and manual inspection with the aim of finding cancer is performed by two observers on the VE images, the results of which are compared to pathology. In the following sections the methodology is explained and results are reported. In the Discussions and Conclusions section results from similar work are reported, and the limitations of the current work, suggestions for further improvements, and future pathways are discussed.

6.2 Methods and Materials

6.2.1 Data Collection and Processing

RF longitudinal data frames were obtained from 5 cases using the setup described in Chapter 4. Pathology results were also available. Computation of the vibro-elastography images was performed similarly to that of previous chapters, however, additional changes were made to improve image quality as follows:

Computation of the vibro-elastography images

The Correlation Coefficient (CC) [115] is a measure computed for each block of tissue, as a function of time, during tissue displacement estimation. The CC is a measure of how accurate the displacement estimation is, ideally being 1, and is computed as below:

$$CC_{1,2} = \frac{CCF_{1,2}}{\sqrt{ACF_{1,1}ACF_{2,2}}} \tag{6.1}$$

where $CCF_{1,2}$ is the maximum value of the cross-correlation function between signals 1 and 2 and $ACF_{1,1}$ and $ACF_{2,2}$ are the maximum values of the auto-correlation functions. To improve the quality of the images, we monitor the CC. If the CC falls below a certain threshold set by the user, the corresponding displacement estimations for that portion of time are not used for computing the transfer function. If more than a specified number of frames of data have a CC less than the defined threshold, a 'gap' exists and data from the frames before and after this gap, assuming that they have an acceptable length, are separately used to compute two transfer functions. Accordingly, if more gaps exist, multiple transfer functions are computed, which are ultimately averaged. We set the acceptable length of data to 8 frames and define a gap as 2 or more consecutive unacceptable frames. For only one unacceptable frame, the corrupt data is replaced by interpolating between the frames before and after. Currently the CC threshold is set by trial and error for each case in order to obtain visually improved images (a value in the range 0.7-0.9). Fig. 6.1 illustrates the concept. This method has shown to improve the resulting VE images as seen in Fig. 6.2.

The pixel intensity value, VE_{jk}, at axial location k and lateral location (line) j of a longitudinal vibro-elastography image used in this chapter is computed as the weighted average of the magnitude of the transfer function:

$$VE_{jk} = \frac{1}{N} \sum_{n=1}^{N} \frac{\int_{f_1}^{f_2} \left(CF_{ref}^{jk}(j2\pi f) \left| H_{ref}^{jk}(j2\pi f) \right| \right) df}{(f_2 - f_1) \int_{f_1}^{f_2} CF_{ref}^{jk}(j2\pi f) df} \tag{6.2}$$

where $(H_{ref}^{jk}(j2\pi f)$ is the transfer function computed with respect to a reference location ref, $CF_{ref}^{jk}(j2\pi f)$ is the coherence function, used as the weight, and $[f_1, f_2]$ describes the frequency range of interest, which in this work coincides with the range of the broad-band vibration applied to tissue, and N is the number of transfer functions computed from portions of correct data, after removing low CC frames.

If at location jk no acceptable length of data exists for which the corresponding CC is above the defined threshold, a value of zero is returned and the stiffness value of that block of tissue is considered unreliable. In order to distinguish between this unreliable value and a very stiff region (i.e. a TF value of zero), for each TF image a corresponding binary image of the same size is produced. In these images pixel values of zero indicate unreliable
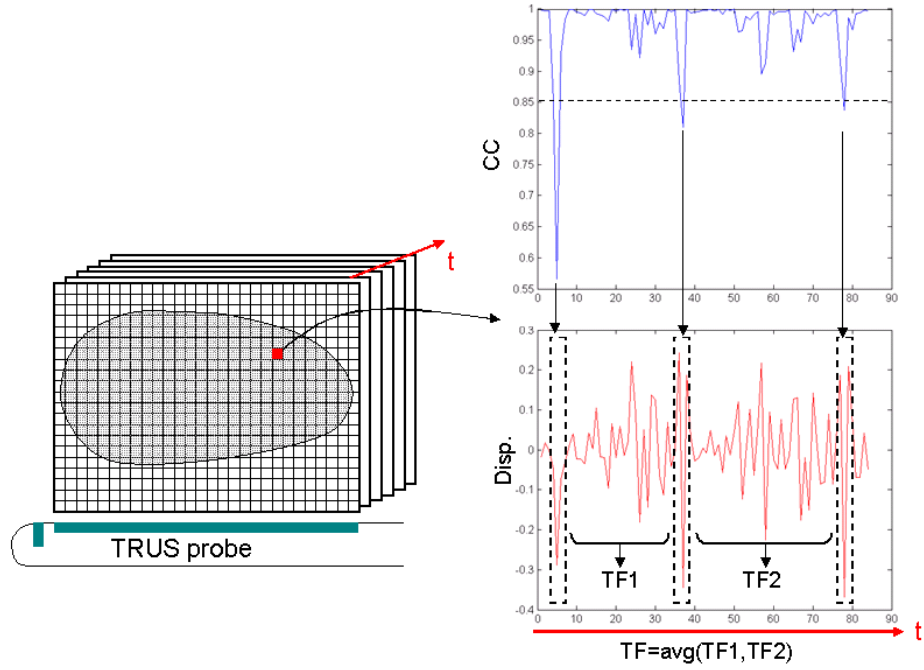
Figure 6.1: Illustration of the transfer function improvement by removing data with low CC. Approximately 80 frames of RF data are collected from the prostate, for each angle, using the TRUS probe (left). For each region in the probe's field of view (red square) the tissue displacement (lower right plot) is estimated through time, as the tissue is vibrated. Along with the displacement estimation, the correlation coefficient (CC) is also computed (upper right plot). Instead of computing the transfer function (TF) using all the displacement data, a threshold on the CC (in this case 0.85) is set to remove erroneous displacement data. TFs are computed from portions of correct data (TF1 and TF2) which are finally averaged to provide the final TF. The average value of the magnitude of the TF, over the vibration frequency range, defines the intensity of the corresponding pixel (red square).

data.

Finally, from the set of fan-shaped longitudinal images, 3D VE matrices or 'volumes' were constructed via interpolation, as described in Chapter 4, Section 4.2.1.
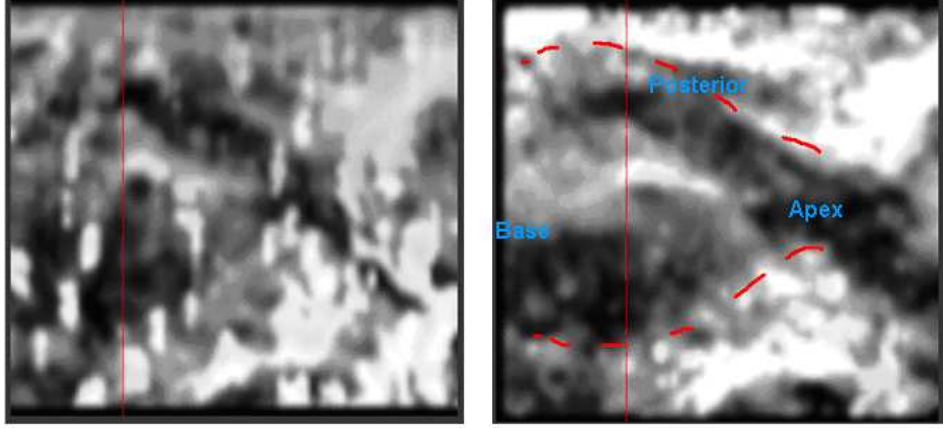
Figure 6.2: The effect of removing data with low correlation (CC). The two figures show the magnitude of the transfer function from the same prostate in the sagittal view, before (left) and after (right) removing low CC data. In this case a threshold of CC=0.85 was used.

Pathology data

In addition to RF data, whole-mount pathology analysis has also been performed on the extracted prostates. The whole-mount sections were produced using the multi-bladed cutting device described in [24]. Each section is 4 mm thick from which, in a routine manner, a fine slice was cut and mounted on a glass slide for hematoxylin and eosin staining. From each prostate, 9-13 slides, depending on the size of the gland, were produced on which cancer regions were detected and marked by a certified pathologist (see Fig. 6.3). The slides were scanned and aligned to correct for the in-plane translation and rotation of each slide with respect to its adjacent slides. To correct the in-plane translation, bounding boxes were created for each prostate slice and the centers of these bounding boxes were aligned. Correction of the in-plane rotation of the slides was performed manually by inspecting the internal structures of the prostate, including the urethra and the texture of the central zone. Figure 6.4 shows an example of manual correction of the orientation of two consecutive pathology slices based on the gland boundary and internal structures. The aligned pathology images were converted into a Stradwin file format [109]. Using the Stradwin software we observed and manually segmented the prostate boundary and cancerous regions to create prostate and cancer surfaces, an example shown in Fig. 6.5.
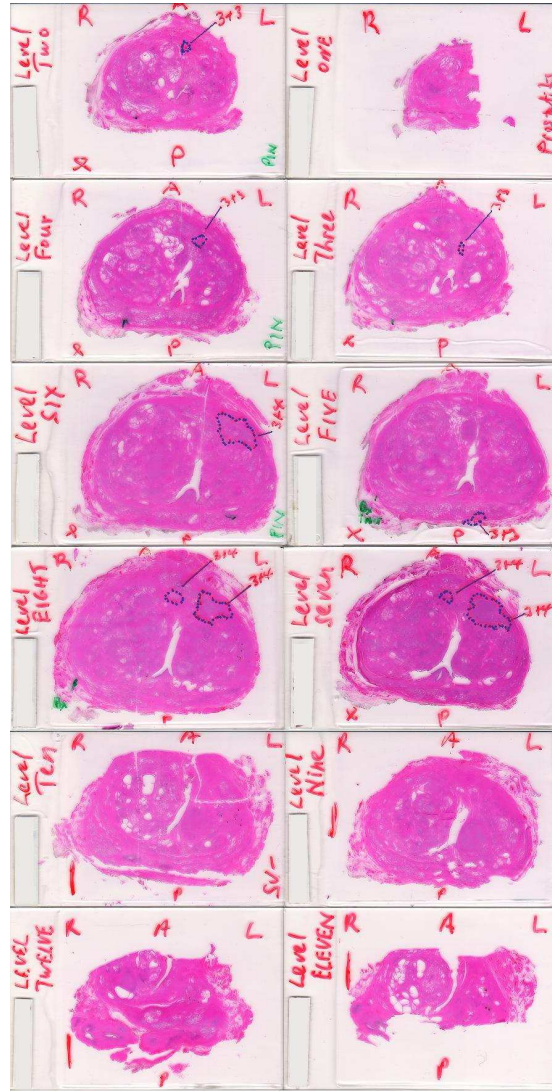
Figure 6.3: An example of pathology slides of one case with cancerous regions and grades defined. Starting from the apex, the number defined as 'level' corresponds to the depth at which the sample was taken. Cancer is marked by dotted lines. The left and right side of the prostate is marked as 'L' and 'R', the anterior and posterior marked as 'A' and 'P', respectively.
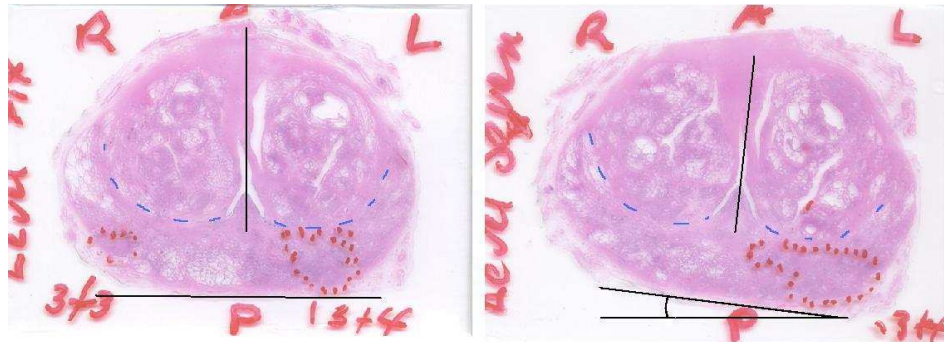
Figure 6.4: An example of manual correction of the orientation in pathology slides based on the gland internal structure. In this case, guided by the prostate boundary and internal structures (marked as blue dashed and black solid lines), the slice on the right will be rotated counter-clockwise to align with its prior slice on the left.
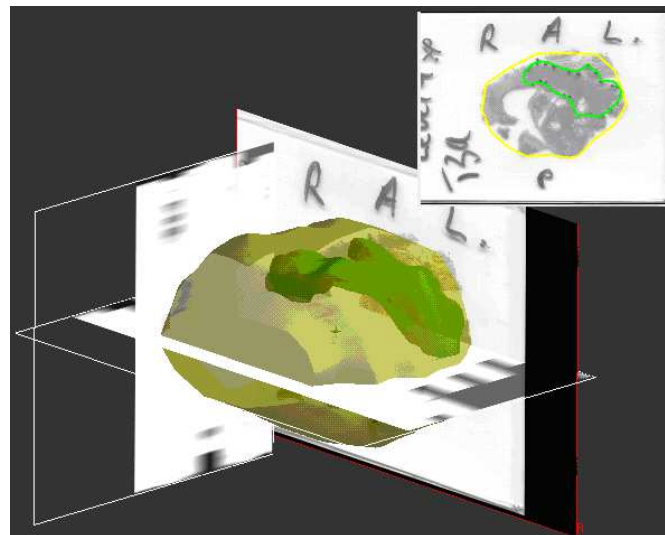
Figure 6.5: The set of pathology images are converted to a Stradwin file format. The prostate and the marked cancer regions are then segmented in this software.

6.2.2 Cancer Visibility in VE Images

To evaluate the visibility of cancer in VE images the VE volumes were observed by two individuals who were blind to the pathology results. The first observer (the author of this thesis) was more familiar with the appearance of cancer in VE images, while the second had less experience. Transverse slices in the VE volume corresponding to the pathology slices were identified by the registration procedure proposed by Taquee et al. in [104]. In these slices, all regions suspected for cancer were segmented by the two individuals. We will refer to these identified tumors as the 'guessed tumors', with the marked tumors in pathology being the 'gold standard'. Suspicious regions were chosen as regions with low intensity (or dark areas, corresponding to relatively stiffer tissue) which were continuously seen in multiple transverse VE images. We assume that dark regions seen in only one or two images are artefacts.

These suspected tumors were then compared with pathology results in a region-based manner. For this, the outlined tumors in each of the pathology slices were labeled as being in one of the four regions: left and right lateral, anterior and posterior. A guessed tumor in VE which also exists in the same region and has approximately the same size, is marked as a true positive.

Figure 6.6 shows a few examples of how the comparison was performed. In this figure, matching tumors are linked with red lines and the false positive and false negatives are marked by FP and FN, respectively. We considered only tumors with an area larger than 7 mm^2 (3 mm diameter) in both pathology and VE since the coarse resolution of the VE images and the presence of noise complicates the detection of small tumors.

In the five studied cases, 25% of the tumors were located in the anterior, 25% in the left lateral, 19% in the right lateral and 31% in the posterior. For the first observer, the sensitivity of detecting cancer in the correct region of the VE image corresponding to the pathology slice was 72.5%. 24.4% of tumors could not be correctly detected in VE (false negatives). 37.3% of the guessed tumors in VE were in fact not cancerous (false positives). The sensitivity of VE for detecting cancer with a Gleason score of 7 and above was 85%. In terms of size, the undetected tumors (considering only those >7 mm^2 in size) had an average area of 24±20 mm^2 (5.4±5 mm diameter). It was observed that many of these false negatives were in the mid-posterior region of the prostate, above the TRUS probe. In this area we have observed that the VE image quality (i.e. visibility of the prostate boundary) degrades. Our results showed a higher the detection rate in VE for higher Gleason scores. Gleason scores for 51 tumors were available. 20
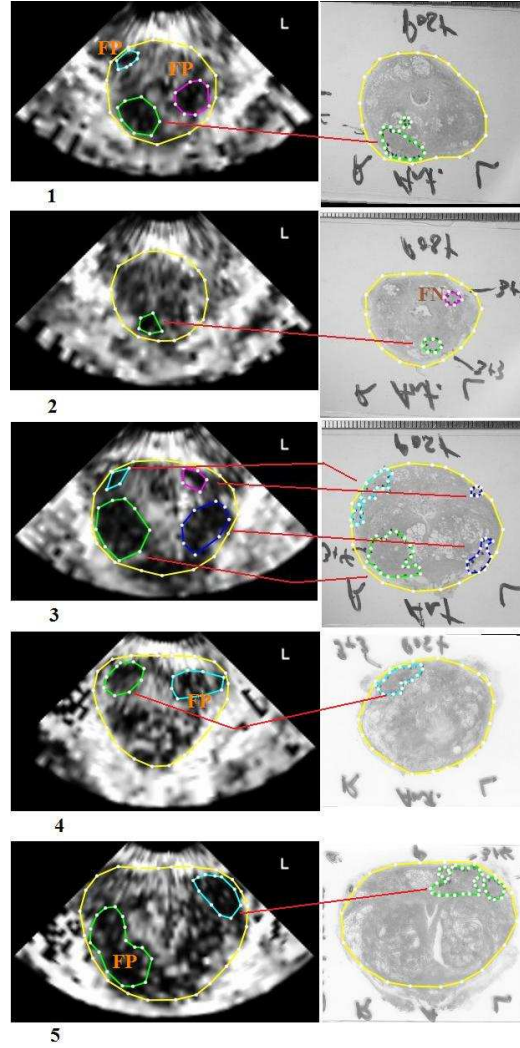
Figure 6.6: Examples of how evaluation of cancer visibility in VE was performed in five pairs of transverse VE (left column) and pathology (right column) images. Corresponding VE and pathology images were found via registration and guessed tumors were marked on VE images and compared to those in pathology. Matching tumors (true positives) are linked with red lines and the false positive and false negatives are marked by FP and FN, respectively.

out of the 31 tumors with Gleason scores of 3+3 (64.5%), 13 of the 16 tumors with Gleason scores of 3+4 (81.25%), both tumors with Gleason scores of 4+3+5 and both tumors with Gleason scores of 4+5 were detected.

However, observer variability in visual detection of cancer is high and the level of experience of the observer greatly affects cancer detection results. For the second observer (with less experience with cancer in VE images) the sensitivity of detecting cancer in the correct region drops to 43.1%. The percentage of undetected tumors was 56.9% and the percentage of incorrect guesses was 47.6%. The average area of undetected tumors (again, considering only those >7 mm^2 in size) was 63 ± 50 mm^2 (9 ± 8 mm diameter), larger than that of the first observer.

Table 6.1 shows the sensitivity, percentage of undetected tumors (false negatives/number of tumors) and the percentage of incorrect guesses (false positives/number of guessed tumors) for the four prostate regions of the registered slices and the whole gland.

	Sens.%		% undetected		% incorrect guess	
	Obs. 1	Obs. 2	Obs. 1	Obs. 2	Obs. 1	Obs. 2
Ant.	78.3	28.6	21.7	71.4	30.8	16.7
LL	77.8	31.3	22.3	68.8	44.0	61.5
RL.	82.3	68.8	17.6	31.3	50.0	50.0
Post.	64.3	26.1	35.7	73.9	41.9	33.4
Whole	75.8	43.1	24.2	56.9	37.3	47.6

Table 6.1: The sensitivity, percentage of undetected tumors (false negatives/number of tumors) and the percentage of incorrect guesses (false positives/number of guessed tumors) for the four regions of the matching slices and the whole gland.

We noticed that in some cases cancerous tumors which were located in pathology on the anterior of the prostate were also visible in the VE images. Such tumors may be missed by TRUS based biopsy. The reason for that is the depth (and therefore the anterior-posterior position of the biopsy core) is determined by the length of the core which rarely exceeds 10 mm. Thus in most cases biopsy only samples the posterior 1/4 to 1/2 of the gland depending on the anterior-posterior diameter. This is usually adequate, since anteriorly located tumors are generally restricted to the apex where the anterior-posterior diameter is small. However, when cancer is located out of the reach of biopsy it is most likely to be missed and therefore, VE has the potential to be used in image guided prostate biopsy. Figure 6.7
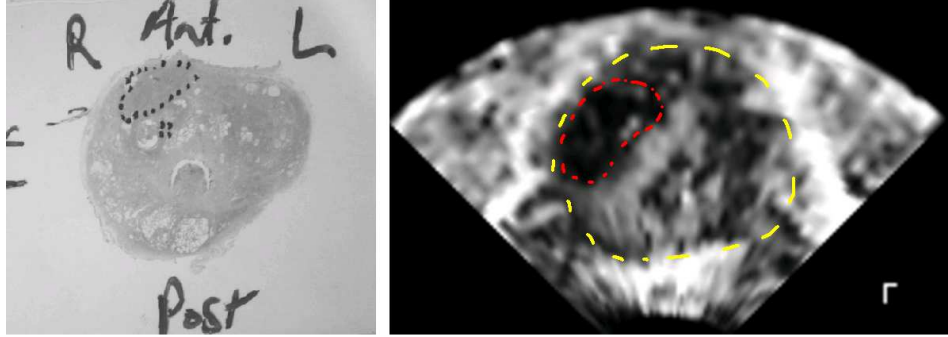
Figure 6.7: An example of an anteriorly located tumor detected as a dark region in the corresponding VE image.

shows an example of an anteriorly located tumor detected as a dark region in the corresponding VE image.

6.3 Discussion and Conclusions

In recent years, prostate cancer detection with the use of elastography has been of interest to many groups, but is still in an early stage. A general agreement exists that in the prostate, cancer is stiffer than healthy tissue (with a stiffness ratio of 1.5-3.5:1). This knowledge has been used as the basis for detecting cancer. Several groups have performed similar studies on the visibility of cancer in elastography images.

Salomon et al. [91] investigate the sensitivity and specificity of cancer detection in the prostate using ultrasound elastography in patients going through radical prostatectomy. The elastography images they used were strain images created by manually applying compression and decompression of the prostate using the transrectal ultrasound probe. An EUB-6500HV Hitachi ultrasound system with a V53W 7.5 MHz transrectal end-fire probe was used (Hitachi Medical, Kashiwa, Japan). In a single institution, single observer study on 109 patients with positive biopsies, B-mode and elastography images were recorded in the transverse plane and areas suspicious for cancer were marked on the elastography images. Histopathological evaluation was performed on slices 3 mm apart. Sensitivity and specificity was reported for the 6 regions of the gland (right and left side of the apex, midgland and base) with an average of 75.4% (range 68.1-84.0%) and 76.7% (range 67.0-84.0%) respectively. They report a positive predictive and neg-

ative predictive value of 87.8% and 59% and an accuracy of 76%. The detection rate of cancer foci was best in the apex where approximately 90% of the tumors were detected and worst at the base where only 75% of the tumors were detected.

In a paper by Pallwein et al. [82] the prostate of 15 patients with organ confined cancer confirmed by biopsy and scheduled for radical prostatectomy were studied. Real-time elastography was performed by two radiologists, blind to the biopsy results, and the images were interpreted by consensus. A Voluson 730 (GE Healthcare, Chalfont St Giles, UK) with an endorectal side fire 7.5MHz transducer was used. Displacement estimates and strain images were computed from radio frequency data produced from manual compression and decompression of the transducer. Similar to [91] six outer gland regions (left and right of base, mid, and apex) were evaluated for cancer. Only hard lesions with a diameter of ≥ 5 mm were considered malignant in elastography images. 35 tumors of this size were found on histopathology slides, 32 of which were in the outer gland and 3 in the inner gland. Elastography detected 28 of the 35 tumors and of the 7 undetected foci, 3 were in the inner gland, and 3 at the base. The best sensitivity for elastography was at the apex (100%) and the worst at the base (detection of only two of the five foci), with the mid-gland sensitivity being 94%. Four sites with false positive findings on elastography were reported. The overall outer gland sensitivity, specificity and accuracy values of 0.88, 0.93 and 0.91 were obtained. The positive and negative predictive values were, respectively, 0.88 and 0.93.

In a work by Sumura et al. [101] real-time elastography findings were compared to digital rectal examination, color Doppler ultrasonography, gray-scale transrectal ultrasonography and T2-weighted and dynamic contrast enhanced MRI. Histopathology was used as the gold standard (microslides spaced at 5 mm intervals) on which 26 tumors with volumes larger than 0.1mL were marked in two regions: anterior (including the transition zone and/or anterior side of the peripheral zone) and posterior. Strain images were obtained using an EUB8500 ultrasound system (Hitachi, Japan) with an end-firing 7.5MHZ transrectal probe by manual compression and decompression of the TRUS probe. They report that the cancer detection rate is superior to all other methods listed above, with an overall detection rate of 75% in the anterior and 73.7% in the posterior of the prostate. As expected, the larger the tumor and the higher the Gleason score, the higher the detection rate.

Tsutsumi et al. [111] collected strain images in the transverse plane from the base to the apex from 51 patients going through radical prostate-

119

ctomy and compared to the corresponding pathological transverse sections of the prostate. Strain images were obtained by manual compression of a 7.5MHz biplanar probe and an EUB6500 Hitachi ultrasound system (Hitachi, Japan). The detection rate of tumors and relationship of tumor locations in elastography, and relationship between Gleason score and cancer stage and elastographic findings was observed. For the anterior, middle and posterior part of the prostate, they report a sensitivity of 94%, 76% and 57% and a positive predictive value of 83%, 72%, and 70%, respectively. The minimum detectable tumor diameter in their images was 4 mm. Surprisingly, the detection of low grade tumors was more accurate than high grade tumors (100% for Gleason score 6, 85% for Gleason score 7, 85% for Gleason score 8 and 63% for Gleason score 9 or 10) and the detection of T1c tumors was more accurate than T2 or T3. They attribute these results to the predominance of the peripheral location of high-grade tumors, where their sensitivity results were low, compared to the anterior location of the low-grade tumors, where they report better sensitivity results.

In a similar study [65] but on a larger population (311 patients), Miyagawa et al. show that the sensitivity of elastography and elastography+TRUS imaging in detecting cancer (confirmed by biopsy) is higher than that of DRE or TRUS only. They report sensitivity of cancer detection in DRE (37.9%), TRUS (59.0%), elastography (72.6%) and TRUS+elastography (89.5%). Higher prostate-specific antigen (PSA) level and smaller prostate volume are reported to increase the sensitivity of elastography and elastography+TRUS. However, the high frequency of false-positive elastography results and difficulty in the detection of cancer in the peripheral zone are two main problems reported in their work. They report no significant difference in the sensitivity related to Gleason score. Biopsy findings were used as the gold standard and regional evaluation was not performed.

In a recent study, Tsutsumi et al. [110] introduce a new excitation technique called real-time balloon inflation elastography (RBIE) in which manual inflation and deflation of a balloon covering the TRUS probe by a piston-type injector is used instead of manual compression of the tissue. This results in more stable images and reduces operator dependence. They presented the accuracy and feasibility of this technique in the detection of prostate cancer on 55 cases in which pathologic specimens were compared to RBIE images. In this method only 1% of the images were affected by artifacts due to slippage in the compression plane whereas in manual compression this number was 32%. They report a sensitivity of 84% in the anterior, 85% in the middle and 60% in the posterior of the prostate and positive predictive values of 75%, 79%, and 93% for the three regions. A

specificity of 80%, 91% and 96% for the three regions was obtained; an improvment in the posterior region compared to manual compression. They report that with the RBIE method the detection rate of Gleason scores 7 or more is larger than cases with a Gleason score of 6 or less.

We showed that it is possible to visually detect cancer in VE images and our sensitivity values are comparable to some of the above work, but our results are yet to be improved. In the above studies (except for that of Tsutsumi et al. [110]) elastography images were obtained by manually exciting the tissue. This increases user dependability, whereas, in our method excitation is performed automatically. However, in all the aforementioned work, including ours, detection of cancer is manually performed where an individual observes the images and decides whether it is cancer or not. Results from this form of detection greatly depend on the experience of the observer, as we showed. Unfortunately, in the above studies, results from multiple observers were not reported.

There are many interesting pathways which can be followed from here. Next, we enlist some current limitations of our work and potential research paths.

Current limitations and potential research areas

An exact shape and/or area-based comparison between pathology and suspected cancer regions was not performed due to the various sources of error that currently exist, some of which are as follows:

Regarding the registration of the VE volume to the pathology volume, in an ideal situation it is expected that the cancer contours extracted from pathology images, when overlaid on the corresponding registered VE images, exactly delineate the cancer as seen in VE. However this is not the case for various reasons.

Firstly, the registration method is surface-based. Therefore, any prostate segmentation error will directly affect the registration outcomes. Although purely images based registration errors are not unaffected by image artifacts and noise, a combined image- and surface-based method may improve the results.

The second issue is that there are no obvious and consistent landmarks seen inside both the VE and pathology volume. Therefore identifying, for example, which slice in the VE volume corresponds to the first slice of the pathology is not an easy task. We assumed that the volume of the prostate or the area of the prostate in each slice does not change significantly. We segment a portion of the prostate in the VE volume that has the same superior-inferior length of the prostate in pathology and that the base and apex areas approximately match.

Thirdly, the registration algorithm used assumes that the TRUS probe is parallel to the superior-inferior axis of the prostate or, in other words, the registered transverse pathology slices can not have an orientation where a pitch (rotation around the left-right axis of the prostate) exists. The solution provided by Nir et al.[75], considers this and is therefore, deemed more appropriate for use in the future.

Some error is introduced during the preparation of the pathology slides. The exact location from which pathology specimens are created is not known. The ends of the prostate are first removed before creating the whole-mounts but it is not clear of what size. The specimens are then cut from 4 mm thick whole-mount slices and placed on slides. Their exact location in the whole-mount is not known. Placing the specimens of the slides also results in a difference in the orientation of each specimen with respect to the other. As a result of these errors, the location of cancer with respect to the prostate surface from pathology is not exact but only approximate.

Additional study of the false positives is also required. The pathology results confirmed only tumors with Gleason scores of 6 and above. There could be a possibility that the stiff regions falsely detected as cancer in VE could eventually become cancer or were seen as stiff regions due to other changes in the prostate tissue, such as prostatic intraepithelial neoplasia or PIN, which is an abnormality of the prostatic gland and believed to precede the development of prostate adenocarcinoma. Alternatively, the higher stiffness of the tissue could be due to reasons other than cancer, such as the presence of calcifications. A pathology analysis more detailed than a clinical report is therefore essential.

In summary, in this chapter we provided groundwork and preliminary tools for pursuing cancer detection in VE images. We listed some of the current limitations of our work and proposed solutions. Our current results show that cancer can sometimes be visually detected in VE images, however, as other work also suggest, VE alone can not guarantee a high sensitivity and specificity. We suggest that the combined use of different ultrasound image types or modalities can possibly lead to better detection results and furthermore, lead to the development of an automated method for in-vivo cancer detection.

Chapter 7

Conclusions and Future Research

In Chapters 2, 3, 4, and 5 novel algorithms and methods were proposed with the ultimate goal of segmenting the prostate boundary. In Chapter 2 a 3D semi-automatic prostate segmentation method was presented. The method was clinically tested with low dose rate brachytherapy as its application in Chapter 3. Vibro-elastography was shown to improve the visibility of the prostate in Chapter 4, the results of which were used to devise an automatic segmentation method in Chapter 5. As a further step, visibility of cancer was studied in Chapter 6. All proposed methods were tested on in-vivo patient data.

7.1 Contributions

The contributions of this thesis are summarized as follows:

- Developing a clinically acceptable prostate segmentation tool. This tool is currently being clinically used as part of the low dose rate prostate brachytherapy procedure in BC Cancer Agency, Vancouver Cancer Center. This tool simplifies delineation, reduces user variability and produces smooth and symmetrical prostate contours which adhere to the brachytherapy guidelines used in this center. By using this method, individuals other than physicians can create the contours and physicians are only required to provide corrections.

- Modeling the prostate boundary. A warped and tapered ellispoid was found to be a suitable shape for modeling the prostate. The benefits of using a model is less sensitivity of the segmentation algorithm to image noise. On the other hand, irregular shapes, such as prostates with extracapsular cancer, can not be properly segmented by such a pre-defined model. However, for low dose rate brachytherapy, the

application in which our method was used, cancer is usually intracapsular, and smooth and symmetric contours are required, therefore, this will not cause an issue for the majority of cases.

- Extensive evaluation of the semi-automatic segmentation method. We would like to emphasize the need for proper evaluation of proposed segmentation methods. In most segmentation methods seen in the literature, evaluation is limited to computing the accuracy of the method compared to a gold standard, usually manual contours. Since there is no standard set of segmented ultrasound images of the prostate, there is no ground truth to compare various segmentation methods against. Obviously, a set of high quality prostate images will lead to good automatic segmentation results. A reported error is meaningful only when a measure of the quality of the images used for evaluation or the accepted range for that specific application is also provided. We provide this acceptability range by measuring the inter- and intra-observer variability in manual segmentation.

- Region-based evaluation. Since segmentation errors in various regions have different consequences with respect to treatment planning, a region-based evaluation provides more information about the suitability of a segmentation method. Our region-based evaluation, where error values are reported for nine sectors of the prostate, provides this.

- The feasibility of using vibro-elastography images for visualizing the prostate boundary was quantitatively studied. Vibro-elastography images were compared to those of B-mode, the commonly used image type, with MRI as the gold standard. The assessment was performed both on the boundary visibility and contrast of the gland with respect to its surrounding tissue. Additionally, a volume-based comparison between surfaces created from B-mode and VE images and those from MRI images was performed.

- Developing a new edge measure: the edge continuity. This measure has been used for evaluating visibility of the prostate boundary in B-mode and VE images. It has also been used for segmenting the prostate. We showed that the addition of this measure to our active shape model-based segmentation algorithm improves edge detection.

- Developing an automatic 3D algorithm for segmentation of the prostate using a combination of B-mode and vibro-elastography images.

7.2 Future work

Novel methods have been presented in this thesis for segmenting and assessment of visualization of the prostate gland. A number of interesting areas of research can be suggested as follows:

- Extending the semi-automatic segmentation algorithm to be used in prostate interventions other than LDR brachytherapy. Whether this algorithm is suitable for use with other prostate treatment methods or on other modalities is yet to be tested. For example, our preliminary tests showed that MRI images are too detailed for the IMMPDA edge detector to detect the correct prostate edge.

- Integrating the prostate segmentation algorithm into an intra-operative treatment method. Currently in LDR brachytherapy at the Vancouver Cancer Center the prostate is imaged a few days or weeks prior to the treatment, this being called the volume study. The volume is segmented, manually or automatically, and based on the obtained planning target volume, a treatment plan is created. In the operating room the B-mode images of the gland are manually registered to the images taken at the volume study and treatment is carried out. The segmentation algorithm, used intra-operatively, can aid registration. Once the two image sets are segmented, the results of registration of the contours can be used to guide the motion of the TRUS probe to achieve registered pre- and intra-operative images. Furthermore, if used with an intra-operative treatment planning algorithm the additional pre-operative imaging can be bypassed, avoiding the necessity to register the images, needless to say the extra costs.

- The automatic method can be used in segmentation of other organs, e.g. the kidney, since any model can be created and used from a training set.

- Active shape models only use shape constraints with some information about the image collected near landmarks (e.g. edge points). Methods such as active appearance models on both image types can improve segmentation results as they incorporate other information such as image texture.

125

- The quality of vibro-elastography images still has room for improvement. Areas where improvements could be made include the data collection procedure and image processing. The data collection setup used in this thesis is favorable in the sense that very little modifications to a standard brachytherapy setup are needed. However, a few flaws exist:

The roll of the rotation motor covers a range of approximately -45 to 45 degrees. Large prostates fall outside this field of view laterally especially in the mid-region.

The TRUS probe is not a completely rigid object and acts as a cantilever-like structure. Therefore, the desired motion cannot be exactly produced throughout the length of the probe. Direct measurement of the probe motions via sensors embedded in the probe, or modeling the motion of the probe during data processing can increase the accuracy of our results.

Proper placement of the TRUS probe is important for obtaining high quality images. Applying too much pressure on the prostate leads to excessive deformation and compression of the gland while too little pressure will not guarantee adequate propagation of vibration throughout the prostate. Currently the position of the TRUS probe, prior to collecting RF data, is adjusted by observing the quality of the B-mode image and is based on the experience of the individual positioning the probe. Providing visual guides for probe placement, such as with the help of force sensors placed along the transducer, is suggested.

The resolution of the images that we use is coarse compared to the resolution of standard medical images such as ultrasound B-mode and MRI. With the current code, increasing the resolution is simple. However, processing time will increase which is not in favor of our goal of obtaining a real-time imaging method.

In computing the VE images, 1D motion estimation is performed in the axial direction. It is clear that lateral motion is also present during vibration of the tissue. We observed that the quality of VE images is relatively poor in the posterior region. This is possibly due to the presence of soft tissue and sliding of the probe on the rectal wall which, we believe, results in excessive lateral motion in this region.

In the VE images used in this work stiffness is computed 'relative' to a reference location. Based on our qualitative assessment of VE images obtained using various reference points we chose the average motion

126

of the tissue along a line passing through the focal point, being set to half the tissue depth. Further investigation on the selection of the reference may improve image quality.

- The area of cancer detection in elastography images is a relatively new area of research. Currently a suspicious prostate is screened for cancer using biopsy. Biopsy is an invasive procedure with a high false negative rate. Repeats are commonly required. An elastography image which reliably displays the prostate in a timely manner can potentially eliminate the need for biopsy. Or, at the least, be used for guided biopsy to improve detection rates. A detailed list of potential research projects in this area is presented in Chapter 6.

Bibliography

[1] S. H. Aaltomaa, V. V. Kataja, T. Lahtinen, J. Palmgren, and T. Forsell. Eight years experience of local prostate cancer treatment with permanent I125 seed brachytherapy–morbidity and outcome results. *Radiotherapy and Oncology*, 91(2):213–216, May 2009.

[2] P. Abolmaesumi and M. R. Sirouspour. An interacting multiple model probabilistic data association filter for cavity boundary extraction from ultrasound images. *IEEE Transactions on Medical Imaging*, 23(6):772–784, 2004.

[3] H. Akbari, X. Yang, L. V. Halig, and B. Fei. 3D segmentation of prostate ultrasound images using wavelet transform. *Proceedings of SPIE*, 7962:79622K, 2011.

[4] D. Ash, A. Flynn, J. Battermann, T. de Reijke, P. Lavagnini, L. Blank, E.S.T.R.A/E.A.U. Urological Brachytherapy Group, and E.O.R.T.C. Radiotherapy Group. Estro/eau/eortc recommendations on permanent seed implantation for localized prostate cancer. *Radiotherapy and Oncology*, 57(3):315–321, Dec 2000.

[5] S. Badiei. Prostate segmentation in ultrasound images using image warping and ellipse fitting. Master's thesis, University of British Columbia, 2007.

[6] S. Badiei, S. E. Salcudean, J. Varah, and W. J. Morris. Prostate segmentation in 2D ultrasound images using image warping and ellipse fitting. *International Conference on Medical Image Computing and Computer Assisted Interventions*, LNCS 4191:17–24, 2006.

[7] M.S. Bazaraa, H.D. Sherali, and C.M. Shetty. *Nonlinear programming: theory and algorithms*. Wiley-Interscience, 2006.

[8] P.J. Besl and H.D. McKay. A method for registration of 3D shapes. *IEEE Transactions on Pattern Analysis and Machine Intelligence*, 14(2):239–256, 1992.

[9] M. Bilgen and M. F. Insana. Predicting target detectability on acoustic elastography. In *IEEE Ultrasonics Symposium*, pages 1427–1430, 1997.

[10] J. C. Blasko, P. D. Grimm, J. E. Sylvester, K. R. Badiozamani, D. Hoak, and W. Cavanagh. Palladium-103 brachytherapy for prostate carcinoma. *International Journal of Radiation Oncology Biology Physics*, 46(4):839–850, 2000.

[11] D. Boukerroui, A. Baskurt, J.A. Noble, and O. Basset. Segmentation of ultrasound images–multiresolution 2D and 3D algorithm based on global and local statistics. *Pattern Recognition Letters*, 24(4-5):779–790, 2003.

[12] Canadian Cancer Society. Canadian cancer statistics. Technical report, 2012.

[13] L. Castéra, J. Vergniol, J. Foucher, B. Le Bail, E. Chanteloup, M. Haaser, M. Darriet, P. Couzigou, and V. de Lédinghen. Prospective comparison of transient elastography, fibrotest, apri, and liver biopsy for the assessment of fibrosis in chronic hepatitis C. *Gastroenterology*, 128(2):343–350, 2005.

[14] S. Catheline, J. L. Gennisson, and M. Fink. Measurement of elastic nonlinearity of soft solid with transient elastography. *Journal of the Acoustical Society of America*, 114(6 Pt 1):3087–3091, Dec 2003.

[15] Y. J. Choi, J. K. Kim, H. J. Kim, and K. S. Cho. Interobserver variability of transrectal ultrasound for prostate volume measurement according to volume and observer experience. *American Journal of Roentgenology*, 192(2):444–449, 2009.

[16] D. L. Cochlin, R. H. Ganatra, and D. F. R. Griffiths. Elastography in the detection of prostatic cancer. *Clinical Radiology*, 57(11):1014–1020, 2002.

[17] T. F. Cootes, A. Hill, C. J. Taylor, and J. Haslam. The use of active shape models for locating structures in medical images. *Image and Vision Computing*, 12(6):355–366, 1994.

[18] T. F. Cootes, C. J. Taylor, D. H. Cooper, and J. Graham. Active shape models-their training and application. *Computer Vision and Image Understanding*, 61:38–59, 1995.

[19] J. M. Crook, L. Potters, R. G. Stock, and M. J. Zelefsky. Critical organ dosimetry in permanent seed prostate brachytherapy: defining the organs at risk. *Brachytherapy*, 4(3):186–194, 2005.

[20] V. Daanen, J. Gastaldo, J. Y. Giraud, P. Fourneret, J. L. Descotes, M. Bolla, D. Collomb, and J. Troccaz. MRI/TRUS data fusion for brachytherapy. *International Journal of Medical Robotics*, 2(3):256–261, 2006.

[21] L. R. Dice. Measures of the amount of ecologic acssociation between species. *Ecology*, 26(3):297–302, 1945.

[22] D. A. Dickey and W. A. Fuller. Distribution of the estimators for autoregressive time series with a unit root. *Journal of the American Statistical Association*, 74(366):427–431, 1979.

[23] M. A. Dresner, G. H. Rose, P. J. Rossman, R. Muthupillai, A. Manduca, and R. L. Ehman. Magnetic resonance elastography of skeletal muscle. *Journal of Magnetic Resonance Imaging*, 13(2):269–276, Feb 2001.

[24] B. Drew, E. C. Jones, S. Reinsberg, A. C. Yung, S. L. Goldenberg, and P. Kozlowski. Device for sectioning prostatectomy specimens to facilitate comparison between histology and in vivo MRI. *Journal of Magnetic Resonance Imaging*, 32(4):992–996, Oct 2010.

[25] O. Ecabert, J. Peters, H. Schramm, C. Lorenz, J. von Berg, M. J. Walker, M. Vembar, M. E. Olszewski, K. Subramanyan, G. Lavi, and J. Weese. Automatic model-based segmentation of the heart in CT images. *IEEE Transactions on Medical Imaging*, 27(9):1189–1201, 2008.

[26] H. Eskandari, S. E. Salcudean, and R. Rohling. Tissue strain imaging using a wavelet transform-based peak search algorithm. *IEEE Transactions on Ultrasonics, Ferroelectrics and Frequency Control*, 54(6):1118–1130, 2007.

[27] A. Fenster, D. B. Downey, and H. N. Cardinal. Three-dimensional ultrasound imaging. *Physics in Medicine and Biology*, 46(5):R67–R99, May 2001.

[28] J. Ferlay, D. M. Parkin, and E. Steliarova-Foucher. Estimates of cancer incidence and mortality in Europe in 2008. *European Journal of Cancer*, 46(4):765–781, 2010.

[29] I. N. Fleming, H. Rivaz, K. Macura, L. M. Su, U. Hamper, G. A. Lagoda, A. L. Burnett II, T. Lotan, R. H. Taylor, G. D. Hager, and E. M. Boctor. Ultrasound elastography - enabling technology for image guided laparoscopic prostatectomy. In *Proceedings of the SPIE Medical Imaging 2009: Visualization, Image-Guided Procedures, and Modeling.*, volume 7261, page 72612I, 2009.

[30] L. Gao, K. J. Parker, R. M. Lerner, and S. F. Levinson. Imaging of the elastic properties of tissue–a review. *Ultrasound in Medicine and Biology*, 22(8):959–977, 1996.

[31] B. S Garra. Elastography: current status, future prospects, and making it work for you. *Ultrasound Q*, 27(3):177–186, Sep 2011.

[32] B. S. Garra, E. I. Cespedes, J. Ophir, S. R. Spratt, R. A. Zuurbier, C. M. Magnant, and M. F. Pennanen. Elastography of breast lesions: initial clinical results. *Radiology*, 202(1):79–86, Jan 1997.

[33] L. Gong, S. D. Pathak, D. R. Haynor, P. S. Cho, and Y. Kim. Parametric shape modeling using deformable superellipses for prostate segmentation. *IEEE Transactions on Medical Imaging*, 23(3):340–349, 2004.

[34] S. Gravas, C. Mamoulakis, J. Rioja, V. Tzortzis, T. de Reijke, H. Wijkstra, and J. de la Rosette. Advances in ultrasound technology in oncologic urology. *Urologic Clinics of North America*, 36(2):133–45, vii, May 2009.

[35] J. F. Greenleaf, M. Fatemi, and M. Insana. Selected methods for imaging elastic properties of biological tissues. *Annual Review of Biomedical Engineering*, 5:57–78, 2003.

[36] P. D. Grimm, J. C. Blasko, J. E. Sylvester, R. M. Meier, and W. Cavanagh. 10-year biochemical (prostate-specific antigen) control of prostate cancer with (125)I brachytherapy. *International Journal of Radiation Oncology Biology Physics*, 51(1):31–40, 2001.

[37] T. J. Hall, Y. Zhu, and C. S. Spalding. In vivo real-time freehand palpation imaging. *Ultrasound in Medicine and Biology*, 29(3):427–435, Mar 2003.

[38] E. J. Halpern, D. L. Cochlin, and B. B. Goldberg. *Imaging of the prostate*. Martin Dunitz, 2002.

[39] A. C. Hodge, A. Fenster, D. B. Downey, and H. M. Ladak. Prostate boundary segmentation from ultrasound images using 2D active shape models: optimisation and extension to 3D. *Computer Methods and Programs in Biomedicine*, 84(2-3):99–113, 2006.

[40] K. Hoyt, K. J. Parker, and D. J. Rubens. Real-time shear velocity imaging using sonoelastographic techniques. *Ultrasound in Medicine and Biology*, 33(7):1086–1097, Jul 2007.

[41] N. Hu, D. B. Downey, A. Fenster, and H. M. Ladak. Prostate boundary segmentation from 3D ultrasound images. *Medical Physics*, 30(7):1648–1659, Jul 2003.

[42] X. Huang and D. N. Metaxas. Metamorphs: deformable shape and appearance models. *IEEE Transactions on Pattern Analysis and Machine Intelligence*, 30(8):1444–1459, 2008.

[43] L. Huwart, C. Sempoux, E. Vicaut, N. Salameh, L. Annet, E. Danse, F. Peeters, L. C. ter Beek, J. Rahier, R. Sinkus, Y. Horsmans, and B. E. Van Beers. Magnetic resonance elastography for the noninvasive staging of liver fibrosis. *Gastroenterology*, 135(1):32–40, 2008.

[44] A. Di Ieva, F. Grizzi, E. Rognone, Z. Tsz Ho Tse, T. Parittotokkaporn, F. Rodriguez Y Baena, M. Tschabitscher, C. Matula, S. Trattnig, and R. Rodriguez Y Baena. Magnetic resonance elastography: a general overview of its current and future applications in brain imaging. *Neurosurgical Review*, 33(2):137–45; discussion 145, Apr 2010.

[45] A. Jendoubi, J. Zeng, and M. F. Chouikha. Top-down approach to segmentation of prostate boundaries in ultrasound images. In *Applied Imagery Pattern Recognition Workshop, 2004. Proceedings. 33rd*, pages 145–149, 2004.

[46] N. N. Kachouie, P. Fieguth, and S. Rahnamayan. An elliptical level set method for automatic TRUS prostate image segmentation. In *Proceedings of the IEEE International Symposium on Signal Processing and Information Technology*, pages 191–196, Aug. 2006.

[47] M. J. Kadour and J. A. Noble. Assisted-freehand ultrasound elasticity imaging. *IEEE Transactions on Ultrasonics, Ferroelectrics and Frequency Control*, 56(1):36–43, 2009.

[48] K. Kamoi, K. Okihara, A. Ochiai, O. Ukimura, Y. Mizutani, A. Kawauchi, and T. Miki. The utility of transrectal real-time elastography in the diagnosis of prostate cancer. *Ultrasound in Medicine and Biology*, 34(7):1025–1032, Jul 2008.

[49] L. Kanzler. *A study of the efficiency of the foreign exchange market through analysis of ultra-high frequency data*. PhD thesis, Oxford University, Oxford, UK, 1998.

[50] L. Kitchen and A. Rosenfeld. Edge evaluation using local edge coherence. *IEEE Transactions on Systems, Man and Cybernetics*, 11(9):597–605, 1981.

[51] E. Konofagou and J. Ophir. A new elastographic method for estimation and imaging of lateral displacements, lateral strains, corrected axial strains and Poisson's ratios in tissues. *Ultrasound in Medicine and Biology*, 24(8):1183–1199, Oct 1998.

[52] E. E. Konofagou, J. D'hooge, and J. Ophir. Myocardial elastography– a feasibility study in vivo. *Ultrasound in Medicine and Biology*, 28(4):475–482, Apr 2002.

[53] E. E. Konofagou and J. Ophir. Precision estimation and imaging of normal and shear components of the 3D strain tensor in elastography. *Physics in Medicine and Biology*, 45(6):1553–1563, Jun 2000.

[54] P. D. Kovesi. MATLAB and Octave functions for computer vision and image processing. Centre for Exploration Targeting, School of Earth and Environment, The University of Western Australia. Available from: <http://www.csse.uwa.edu.au/∼pk/Research/research.html>.

[55] H. M. Ladak, F. Mao, Y. Wang, D. B. Downey, D. A. Steinman, and A. Fenster. Prostate boundary segmentation from 2D ultrasound images. *Medical Physics*, 27(8):1777–1788, Aug 2000.

[56] R.M. Lerner, K.J. Parker, J. Holen, R. Gramiak, and R.C. Waag. Sono-elasticity: Medical elasticity images derived from ultrasound signals in mechanically vibrated targets. *Acoustic Imaging*, 16:317–327, 1988.

[57] J. Li, Y. Cui, R. E. English, and J. A. Noble. Ultrasound estimation of breast tissue biomechanical properties using a similarity-based non-linear optimization approach. *Journal of Strain Analysis*, 44(5):363–374, 2009.

[58] R. G. P. Lopata, M. M. Nillesen, H. H. G. Hansen, I. H. Gerrits, J. M. Thijssen, and C. L. de Korte. Performance evaluation of methods for two-dimensional displacement and strain estimation using ultrasound radio frequency data. *Ultrasound in Medicine and Biology*, 35(5):796–812, May 2009.

[59] A. Lyshchik, T. Higashi, R. Asato, S. Tanaka, J. Ito, J. J. Mai, C. Pellot-Barakat, M. F. Insana, A. B. Brill, T. Saga, M. Hiraoka, and K. Togashi. Thyroid gland tumor diagnosis at us elastography. *Radiology*, 237(1):202–211, Oct 2005.

[60] S. S. Mahdavi, N. Chng, I. Spadinger, W. J. Morris, and S. E. Salcudean. Semi-automatic segmentation for prostate interventions. *Medical Image Analysis*, 15(2):226–237, Apr 2011.

[61] S. S. Mahdavi, M. Moradi, X. Wen, W. J. Morris, and S. E. Salcudean. Vibro-elastography for visualization of the prostate region. In *Medical Image Computing and Computer Assisted Intervention*, volume 5762 of *LNCS*, pages 339–347, 2009.

[62] S. S. Mahdavi, M. Moradi, X. Wen, W. J. Morris, and S. E. Salcudean. Evaluation of visualization of the prostate gland in vibro-elastography images. *Medical Image Analysis*, 15(4):589–600, Aug 2011.

[63] S. S. Mahdavi, I. Spadinger, N. Chng, S. E. Salcudean, and W. J. Morris. Semiautomatic segmentation for prostate brachytherapy: Dosimetric evaluation. *Brachytherapy*, 2011.

[64] J. E. McNeal, E. A. Redwine, F. S. Freiha, and T. A. Stamey. Zonal distribution of prostatic adenocarcinoma. Correlation with histologic pattern and direction of spread. *American Journal of Surgical Pathology*, 12(12):897–906, 1988.

[65] T. Miyagawa, M. Tsutsumi, T. Matsumura, N. Kawazoe, S. Ishikawa, T. Shimokama, N. Miyanaga, and H. Akaza. Real-time elastography for the diagnosis of prostate cancer: evaluation of elastographic moving images. *Japanese Journal of Clinical Oncology*, 39(6):394–398, Jun 2009.

[66] W. J. Morris, M. Keyes, D. Palma, I. Spadinger, M. R. McKenzie, A. Agranovich, T. Pickles, M. Liu, W. Kwan, J. Wu, E. Berthelet, and H. Pai. Population-based study of biochemical and survival outcomes

after permanent 125I brachytherapy for low- and intermediate-risk prostate cancer. *Urology*, 73(4):860–5; discussion 865–7, Apr 2009.

[67] R. Muthupillai, D. J. Lomas, P. J. Rossman, J. F. Greenleaf, A. Manduca, and R. L. Ehman. Magnetic resonance elastography by direct visualization of propagating acoustic strain waves. *Science*, 269(5232):1854–1857, Sep 1995.

[68] R. P. Myers. Structure of the adult prostate from a clinician's standpoint. *Clinical Anatomy*, 13(3):214–215, 2000.

[69] S. Nag, D. Beyer, J. Friedland, P. Grimm, and R. Nath. American brachytherapy society (ABS) recommendations for transperineal permanent brachytherapy of prostate cancer. *International Journal of Radiation Oncology Biology Physics*, 44(4):789–799, 1999.

[70] S. Nag, W. Bice, K. DeWyngaert, B. Prestidge, R. Stock, and Y. Yu. The american brachytherapy society recommendations for permanent prostate brachytherapy postimplant dosimetric analysis. *International Journal of Radiation Oncology Biology Physics*, 46(1):221–230, 2000.

[71] S. Nag, J. P. Ciezki, R. Cormack, S. Doggett, K. DeWyngaert, G. K. Edmundson, R. G. Stock, N. N. Stone, Y. Yu, M. J. Zelefsky, and American Brachytherapy Society Clinical Research Committe. Intraoperative planning and evaluation of permanent prostate brachytherapy: report of the american brachytherapy society. *International Journal of Radiation Oncology Biology Physics*, 51(5):1422–1430, 2001.

[72] N. D. Nanayakkara, J. Samarabandu, and A. Fenster. Prostate segmentation by feature enhancement using domain knowledge and adaptive region based operations. *Physics in Medicine and Biology*, 51(7):1831–1848, Apr 2006.

[73] J. C. Nascimento and J. S. Marques. Robust shape tracking with multiple models in ultrasound images. *IEEE Transactions on Image Processing*, 17(3):392–406, 2008.

[74] National Cancer Institute, 2012.

[75] G. Nir and S. E. Salcudean. Registration of whole-mount histology and tomography of the prostate using particle filtering. In *Proceedings of SPIE Medical Imaging*, volume 8676, 2013.

[76] J. A. Noble and d. Boukerroui. Ultrasound image segmentation: a survey. *IEEE Transactions on Medical Imaging*, 25(8):987–1010, . 2006.

[77] M. O'Donnell, A.R. Skovoroda, B.M. Shapo, and S.Y. Emelianov. Internal displacement and strain imaging using ultrasonic speckle tracking. *IEEE Transactions on Ultrasonics, Ferroelectrics and Frequency Control*, 41(3):314–325, 1994.

[78] J. Ophir, I. Céspedes, B. Garra, H. Ponnekanti, Y. Huang, and N. Maklad. Elastography: ultrasonic imaging of tissue strain and elastic modulus in vivo. *European Journal of Ultrasound*, 3(1):49–70, 1996.

[79] J. Ophir, I. Céspedes, H. Ponnekanti, Y. Yazdi, and X. Li. Elastography: a quantitative method for imaging the elasticity of biological tissues. *Ultrasonic Imaging*, 13(2):111–134, Apr 1991.

[80] J. Ophir, B. Garra, F. Kallel, E. Konofagou, T. Krouskop, R. Righetti, and T. Varghese. Elastographic imaging. *Ultrasound in Medicine and Biology*, 26 Suppl 1:S23–S29, May 2000.

[81] K. Otto, B. G. Clark, and C. Huntzinger. Exploring the limits of spatial resolution in radiation dose delivery. *Medical Physics*, 29(8):1823–1831, Aug 2002.

[82] L. Pallwein, M. Mitterberger, P. Struve, G. Pinggera, W. Horninger, G. Bartsch, F. Aigner, A. Lorenz, F. Pedross, and F. Frauscher. Real-time elastography for detecting prostate cancer: preliminary experience. *British Journal of Urology International*, 100(1):42–46, 2007.

[83] K. J. Parker, M. M. Doyley, and D. J. Rubens. Imaging the elastic properties of tissue: the 20 year perspective. *Physics in Medicine and Biology*, 56(1):R1–R29, Jan 2011.

[84] K. J. Parker, L. S. Taylor, S. Gracewski, and D. J. Rubens. A unified view of imaging the elastic properties of tissue. *Journal of the Acoustical Society of America*, 117(5):2705–2712, May 2005.

[85] S. D. Pathak, V. Chalana, D. R. Haynor, and Y. Kim. Edge-guided boundary delineation in prostate ultrasound images. *IEEE Transactions on Medical Imaging*, 19(12):1211–1219, 2000.

[86] M. A. Penna, K. A. Dines, R. Seip, R. F. Carlson, and N. T. Sanghvi. Modeling prostate anatomy from multiple view TRUS images for image-guided HIFU therapy. *IEEE Transactions on Ultrasonics, Ferroelectrics and Frequency Control*, 54(1):52–69, 2007.

[87] C. Pluempitiwiriyawej, J. M. F. Moura, Y. J. L. Wu, and C. Ho. STACS: new active contour scheme for cardiac MR image segmentation. *IEEE Transactions on Medical Imaging*, 24(5):593–603, 2005.

[88] H. Rivaz, E. Boctor, P. Foroughi, R. Zellars, G. Fichtinger, and G. Hager. Ultrasound elastography: a dynamic programming approach. *IEEE Transactions on Medical Imaging*, 27(10):1373–1377, 2008.

[89] F. Sahba, H. R. Tizhoosh, and M. M. Salama. A coarse-to-fine approach to prostate boundary segmentation in ultrasound images. *Biomedical Engineering Online*, 4(58):58, 2005.

[90] S. E. Salcudean, D. French, S. Bachmann, R. Zahiri-Azar, X. Wen, and W. J. Morris. Viscoelasticity modeling of the prostate region using vibro-elastography. *International Conference on Medical Image Computing and Computer Assisted Interventions*, 9(Pt 1):389–396, 2006.

[91] G. Salomon, J. Köllerman, I. Thederan, F. K. H. Chun, L. Budus, T. Schlomm, H. Isbarn, H. Heinzer, H. Huland, and M. Graefen. Evaluation of prostate cancer detection with ultrasound real-time elastography: a comparison with step section pathological analysis after radical prostatectomy. *European Urology*, 54(6):1354–1362, 2008.

[92] C. B. Saw and N. Suntharalingam. Quantitative assessment of interstitial implants. *International Journal of Radiation Oncology Biology Physics*, 20(1):135–139, Jan 1991.

[93] J. A. Schaar, C. L. de Korte, F. Mastik, C. Strijder, G. Pasterkamp, E. Boersma, P. W. Serruys, and A. F. W. van Der Steen. Characterizing vulnerable plaque features with intravascular elastography. *Circulation*, 108(21):2636–2641, 2003.

[94] F. K. W. Schaefer, I. Heer, P. J. Schaefer, C. Mundhenke, S. Osterholz, B. M. Order, N. Hofheinz, J. Hedderich, M. Heller, W. Jonat, and I. Schreer. Breast ultrasound elastography–results of 193 breast lesions in a prospective study with histopathologic correlation. *Eurpean Journal of Radiology*, 77(3):450–456, 2011.

[95] D. Shen, Y. Zhan, and C. Davatzikos. Segmentation of prostate boundaries from ultrasound images using statistical shape model. *IEEE Transactions on Medical Imaging*, 22(4):539–551, 2003.

[96] S. Sidhu, W. J. Morris, I. Spadinger, M. Keyes, M. Hilts, R. Harrison, K. Otto, M. McKenzie, and A. Agranovich. Prostate brachytherapy postimplant dosimetry: a comparison of prostate quadrants. *International Journal of Radiation Oncology Biology Physics*, 52(2):544–552, Feb 2002.

[97] R. Sinkus, J. Lorenzen, D. Schrader, M. Lorenzen, M. Dargatz, and D. Holz. High-resolution tensor MR elastography for breast tumour detection. *Physics in Medicine and Biology*, 45(6):1649–1664, Jun 2000.

[98] W. L. Smith, C. Lewis, G. Bauman, G. Rodrigues, D. D'Souza, R. Ash, D. Ho, V. Venkatesan, D. Downey, and A. Fenster. Prostate volume contouring: a 3D analysis of segmentation using 3DTRUS, CT, and MR. *International Journal of Radiation Oncology Biology Physics*, 67(4):1238–1247, Mar 2007.

[99] R. Souchon, V. Hervieu, A. Gelet J. Ophir, and J. Y. Chapelon. Human prostate elastography: in vitro study. In *IEEE Symposium on Ultrasonics*, volume 2, pages 1251–1253, Oct. 2003.

[100] S. Srinivasan and J. Ophir. A zero-crossing strain estimator for elastography. *Ultrasound in Medicine and Biology*, 29(2):227–238, Feb 2003.

[101] M. Sumura, K. Shigeno, T. Hyuga, T. Yoneda, H. Shiina, and M. Igawa. Initial evaluation of prostate cancer with real-time elastography based on step-section pathologic analysis after radical prostatectomy: a preliminary study. *International Journal of Urology*, 14(9):811–816, Sep 2007.

[102] J. E. Sylvester, P. D. Grimm, S. M. Eulau, R. K. Takamiya, and D. Naidoo. Permanent prostate brachytherapy preplanned technique: The modern Seattle method step-by-step and dosimetric outcomes. *Brachytherapy*, 8(2):197–206, 2009.

[103] M. Tanter, J. Bercoff, L. Sandrin, and M. Fink. Ultrafast compound imaging for 2-D motion vector estimation: application to transient

elastography. *IEEE Transactions on Ultrasonics, Ferroelectrics and Frequency Control*, 49(10):1363–1374, 2002.

[104] F. Taquee, O. Goksel, S. S. Mahdavi, M. Keyes, W. J. Morris, I. Spadinger, and S. Salcudean. Deformable prostate registration from MR and TRUS images using surface error driven FEM models. In *Proceedings of the SPIE 8316, 831612*, 2012.

[105] P. Thevenaz and M. Unser. Snakuscules. *IEEE Transactions on Image Processing*, 17(4):585–593, 2008.

[106] C. W. Thomas, A. Kruk, C. E. McGahan, I. Spadinger, and W. J. Morris. Prostate brachytherapy post-implant dosimetry: a comparison between higher and lower source density. *Radiotherapy and Oncology*, 83(1):18–24, Apr 2007.

[107] I. Thompson, J. B. Thrasher, G. Aus, A. L. Burnett, E. D. Canby-Hagino, M. S. Cookson, A. V D'Amico, R. R. Dmochowski, D. T. Eton, J. D. Forman, S. L. Goldenberg, J. Hernandez, C. S. Higano, S. R. Kraus, J. W. Moul, C. M. Tangen, and A. U. A. Prostate Cancer Clinical Guideline Update Panel. Guideline for the management of clinically localized prostate cancer: 2007 update. *Journal of Urology*, 177(6):2106–2131, Jun 2007.

[108] S. Tong, H. N. Cardinal, R. F. McLoughlin, D. B. Downey, and A. Fenster. Intra- and inter-observer variability and reliability of prostate volume measurement via two-dimensional and three-dimensional ultrasound imaging. *Ultrasound in Medicine and Biology*, 24(5):673–681, Jun 1998.

[109] G. M. Treece, R. W. Prager, A. H. Gee, and L. Berman. Surface interpolation from sparse cross sections using region correspondence. *IEEE Transactions on Medical Imaging*, 19(11):1106–1114, 2000.

[110] M. Tsutsumi, T. Miyagawa, T. Matsumura, T. Endo, S. Kandori, T. Shimokama, and S. Ishikawa. Real-time balloon inflation elastography for prostate cancer detection and initial evaluation of clinicopathologic analysis. *American Journal of Roentgenology*, 194(6):W471–W476, 2010.

[111] M. Tsutsumi, T. Miyagawa, T. Matsumura, N. Kawazoe, S. Ishikawa, T. Shimokama, T. Shiina, N. Miyanaga, and H. Akaza. The impact of real-time tissue elasticity imaging (elastography) on the detection

of prostate cancer: clinicopathological analysis. *International Journal of Clinical Oncology*, 12(4):250–255, 2007.

[112] E. Turgay, S. Salcudean, and R. Rohling. Identifying the mechanical properties of tissue by ultrasound strain imaging. *Ultrasound in Medicine and Biology*, 32(2):221–235, Feb 2006.

[113] I. B. Tutar, S. D. Pathak, L. Gong, P. S. Cho, K. Wallner, and Y. Kim. Semiautomatic 3-D prostate segmentation from TRUS images using spherical harmonics. *IEEE Transactions on Medical Imaging*, 25(12):1645–1654, 2006.

[114] J. M. Varah. Least squares data fitting with implicit functions. *BIT*, 36(4):842–854, 1996.

[115] T. Varghese and J. Ophir. Estimating tissue strain from signal decorrelation using the correlation coefficient. *Ultrasound in Medicine and Biology*, 22(9):1249–1254, 1996.

[116] T. Wu, J. P. Felmlee, J. F. Greenleaf, S. J. Riederer, and R. L. Ehman. Assessment of thermal tissue ablation with MR elastography. *Magnetic Resonance in Medicine*, 45(1):80–87, Jan 2001.

[117] P. Yan, S. Xu, B. Turkbey, and J. Kruecker. Adaptively learning local shape statistics for prostate segmentation in ultrasound. *IEEE Transactions on Biomedical Engineering*, 58(3):633–641, 2011.

[118] X. Yang and B. Fei. 3D prostate segmentation of ultrasound images combining longitudinal image registration and machine learning. In *SPIE*, volume 8316, page 83162O, 2012.

[119] A. Yezzi, S. Kichenassamy, A. Kumar, P. Olver, and A. Tannenbaum. A geometric snake model for segmentation of medical imagery. *IEEE Transactions on Medical Imaging*, 16(2):199–209, 1997.

[120] M. Yin, J. A. Talwalkar, K. J. Glaser, A. Manduca, R. C. Grimm, P. J. Rossman, J. L. Fidler, and R. L. Ehman. Assessment of hepatic fibrosis with magnetic resonance elastography. *Clinical Gastroenterology and Hepatology*, 5(10):1207–1213.e2, 2007.

[121] R. Zahiri-Azar, O. Goksel, and S. E. Salcudean. Sub-sample displacement estimation from digitized ultrasound RF signals using multidimensional polynomial fitting of the cross-correlation function. *IEEE*

Transactions on Ultrasonics, Ferroelectrics and Frequency Control, 57(11):2403–2420, 2010.

[122] R. Zahiri-Azar and S. E. Salcudean. Motion estimation in ultrasound images using time domain cross correlation with prior estimates. *IEEE Transactions on Biomedical Engineering*, 53(10):1990–2000, 2006.

[123] A. Zaim. An edge-based approach for segmentation of prostate ultrasound images using phase symmetry. In *ISCCSP 2008*, pages 10–13, 2008.

[124] M. J. Zelefsky, D. A. Kuban, L. B. Levy, L. Potters, D. C. Beyer, J. C. Blasko, B. J. Moran, J. P. Ciezki, A. L. Zietman, T. M. Pisansky, M. Elshaikh, and E. M. Horwitz. Multi-institutional analysis of long-term outcome for stages T1-T2 prostate cancer treated with permanent seed implantation. *International Journal of Radiation Oncology Biology Physics*, 67(2):327–333, Feb 2007.

[125] Y. Zhan and D. Shen. Deformable segmentation of 3-D ultrasound prostate images using statistical texture matching method. *IEEE Transactions on Medical Imaging*, 25(3):256–272, 2006.

[126] Y. Zhan, D. Shen, J. Zeng, L. Sun, G. Fichtinger, J. Moul, and C. Davatzikos. Targeted prostate biopsy using statistical image analysis. *IEEE Transactions on Medical Imaging*, 26(6):779–788, 2007.

[127] M. Zhang, P. Nigwekar, B. Castaneda, K. Hoyt, J. V. Joseph, A. di Sant'Agnese, E. M. Messing, J. G. Strang, D. J. Rubens, and K. J. Parker. Quantitative characterization of viscoelastic properties of human prostate correlated with histology. *Ultrasound in Medicine and Biology*, 34(7):1033–1042, Jul 2008.